An assessment of equilibrium in the Merensky Reef: A textural, geochemical and Nd isotope study of coexisting plagioclase and orthopyroxene from Winnaarshoek in the eastern Bushveld Complex, RSA

A thesis submitted in fulfillment of the requirements for the degree of

MASTER OF SCIENCE

At

Rhodes University

By

Mark Douglas Raines

February 2014

Department of Geology, Rhodes University

South Africa

Declaration

Material contained in this thesis represents the original work of the author except where specific acknowledgement is made to the work of others.

M.D. Raines

February 2014

Department of Geology

Rhodes University

Grahamstown

South Africa

Abstract

Evidence of mineral disequilibrium is presented for the Merensky Reef at Winnaarshoek in the eastern Bushveld Complex. Petrographic disequilibrium textures, disequilibrium in orthopyroxene, plagioclase and clinopyroxene mineral compositions as well as disequilibrium in Sm-Nd isotopic compositions of whole rock samples and coexisting plagioclase and orthopyroxene are presented. Disequilibrium textures presented include clinopyroxene exsolution lamellae in orthopyroxene; resorbed plagioclase in orthopyroxene or relict plagioclase; various inclusions such as orthopyroxene, plagioclase or clinopyroxene in larger oikocrysts of clinopyroxene or orthopyroxene; discontinuous rims of clinopyroxene surrounding orthopyroxene; resorbed orthopyroxene in clinopyroxene; and corona textures associated with olivine. These textures were used to derive a possible mineral crystallization sequence. At least two sequences of crystallization took place, both of which crystallized plagioclase first. One sequence then crystallized olivine which was then consumed to produce orthopyroxene which crystallized prior to late clinopyroxene. The other sequence indicates orthopyroxene crystallization after plagioclase crystallization, followed by crystallization of clinopyroxene. These sequences indicate at least two magmas were responsible for the genesis of the Merensky Reef and its hanging wall and footwall units.

Compositionally, disequilibrium is evident in the range of compositions found in coexisting orthopyroxene, plagioclase and clinopyroxene with stratigraphic height, with particular reference to the change in mineral composition in each of the hanging wall, Reef and footwall units. Orthopyroxene compositions range in Mg numbers between 74.6 and 82.9 (77.4) in the hanging wall, 78.5 and 87.0 (avg. 81.1) in the Reef, and 77.9 and 84.1 (avg. 81.3) in the footwall. Plagioclase compositions range in An content between $An_{64.9}$ and $An_{82.3}$ (avg. $An_{75.1}$) in the hanging wall, $An_{56.8}$ to $An_{70.8}$ (avg. $An_{62.7}$) in the Reef, and $An_{54.2}$ to $An_{86.3}$ (avg. $An_{73.2}$) in the footwall.

In terms of Sm-Nd isotopic compositions, disequilibrium is evident between both whole rock samples and coexisting plagioclase and orthopyroxenes. Bulk rock Sm-Nd isotopic compositions show a range in ε_{Nd} values between $\varepsilon_{Nd\ (2.06\ Ga)}$ = -4.8 to -6.4 in the hangingwall, $\varepsilon_{Nd\ (2.06\ Ga)}$ = -6.3 to -8.5 in the Reef, and $\varepsilon_{Nd\ (2.06\ Ga)}$ = -4.5 to -6.3 in the footwall. Similar ε_{Nd} values are present in the hanging wall and footwall units, with a clear "spike" in the Merensky Reef. ε_{Nd} values in plagioclase

are between $\varepsilon_{Nd\ (2.06\ Ga)}$ = -5.8 and -7.8, while orthopyroxene isotopic Sm-Nd values are between $\varepsilon_{Nd\ (2.06\ Ga}$ = -7.1 and -9.1.

The mineral disequilibrium features presented within this study help elucidate the crystallization sequence of the magma as well as to constrain the contamination of the magma upon ascension and emplacement of the Merensky Reef. The results of this study favour a model where a mantle plume resulted in the ascent of a new magma which was contaminated by the assimilation of old, lower crust. Contamination took place prior to the possible lateral emplacement of the Merensky reef as a density current. 5-10% contamination of depleted mantle or a B2-"like" source by Archaean TTGs is modeled to achieve the contamination "spike" of ε_{Nd} = -8.5 in the Merensky Reef.

Acknowledgements

First and foremost I would like to thank my supervisor Dr. Steve Prevec, without whom this thesis would not have been completed. Steve's patience, guidance and knowledge have been invaluable. Thank you for your availability at all hours for discussion and advice on numerous aspects of this study (often teaching new or forgotten concepts). Thank you also, for the many hours put into proof reading and editing of this thesis.

I would also like to thank Roger Scoon for providing the Winnaarshoek cores from which we were able to select samples for analysis. Further thanks to Roger for general comments, sampling strategies and advice throughout the preparation of this study.

I would like to thank John Hepple and his technicians at Rhodes University Department of Geology for their time spent in preparing samples and the production of polished thin sections.

I would also like to thank Dr. Gabi Costin for all the hours of assistance using the Electron Microprobe and the help with the analysis and some interpretation of acquired data.

I would like to thank Prof. Julian 'Goonie' Marsh for valuable comments and assistance with the interpretation of raw isotopic data.

Dr. Petrus le Roux, University of Cape Town is thanked for running Sm-Nd analysis of bulk rock and mineral separates.

I would also like to thank my fellow postgraduate students at the Geology Department for their advice and assistance with various aspects of this thesis. Thanks especially, to the members of office 21 for providing laughter at stressful times.

I would also like to thank those organizations which funded me and the project over the past 2 years. Funding for analytical work was provided by Rhodes University Research Committee (RC) grants to Dr S. Prevec in 2012 and 2013. Thank you for the National Research Foundation (NRF) for the provision of a Scarce Skills scholarship, without which this project would not have been possible.

Lastly, I would like to thank my family, friends and girlfriend, Amy for the never ending support provided during the course of this research project. I am so grateful.

Table of Contents

Abstract ..... **i**

Acknowledgements ..... **iii**

Figure and Table Captions ..... **vii**

Figures vii

Tables xi

Chapter 1- Introduction **1**

1.1 Introduction 1

1.2 Rationale and summary of existing disequilibrium literature 2

1.3 Research Aims and Objectives 5

Chapter 2 - Geological Setting **6**

2.1 Regional Geology 6

2.1.1 Lithostratigraphic subdivisions of the Bushveld Complex 6

2.2 Genetic Models 15

2.2.1 Origins of the UCZ 15

2.2.2 Genetic Models 16

Chapter 3- Sampling, Methodology and Analytical methods **22**

3.1 Sampling Strategy 22

3.2 Sample preparation 22

3.2.1 Crushing 22

3.2.2 Mineral Separation 23

3.2.3 Electron Micro-Probe Sample preparation 24

3.2.4 Isotopic sample preparation 24

3.3 Analytical work 25

3.3.1 Petrography 25

3.3.2 Electron Micro-Probe Analysis 25

3.3.3 Isotopic Analysis 25

Chapter 4- Petrography 27

4.1 Macroscopy 27

4.1.1 Lithostratigraphy 27

4.1.2 Core Log Descriptions 31

4.2 Microscopy and Petrography 34

4.2.1 Overview 34

4.2.1 Microtextures 36

4.3 Summaries of Petrologic Observations 47

4.3.1 Orthopyroxene 47

4.3.2 Clinopyroxene 47

4.3.3 Plagioclase 47

4.3.4 Chromite 48

4.3.5 Olivine and reaction phases 48

4.3.6 Phlogopite 49

4.3.7 Base-Metal Sulphides (BMS) 49

Chapter 5- Mineral Chemistry 50

5.1 Hangingwall 50

5.2 Merensky Reef 52

5.3 Footwall 54

5.4 Summary of Mineral Compositional Results 57

5.4.1 Orthopyroxene 57

5.4.2 Plagioclase 58

5.4.3 Clinopyroxene 60

5.4.4 Olivine and reaction phases 60

Chapter 6- Isotope Chemistry 62

6.1 Whole Rock Sm-Nd data 62

6.1.1 Footwall 62

6.1.2 Merensky Reef 62

6.1.3 Hanging Wall 63
6.2 Mineral Separate Sm-Nd data 63
6.2.1 Plagioclase 64
6.2.2 Orthopyroxene 64
6.3 Summary of Isotopic Results 68

Chapter 7- Discussion 71
7.1 Evidence of Disequilibrium 71
7.1.1 Petrography and mineral compositions 71
7.1.2 Sm-Nd isotopic evidence for disequilibrium 76
7.2 Evidence for magma- crystal mixing 77
7.3 Features of the Mineralized Reef Zone 82
7.4 Contamination 85
7.4.1 Modeling the Contamination 85
7.4.2 Contamination Model 88
7.5 Implications for Genetic Models 91

Summary and Conclusions 95

References 97

Appendix A- Orthopyroxene compositions (EPMA) from the Merensky Reef at Winnaarshoek **..... 106**

Appendix B- Clinopyroxene compositions (EPMA) from the Merensky Reef at Winnaarshoek **..... 121**

Appendix C- Plagioclase compositions (EPMA) from the Merensky Reef at Winnaarshoek **..... 133**

Appendix D- Simple mass balance contamination models **..... 146**

Figure and Table Captions

Figures

Figure 1.1 Sm-Nd Isochron diagram showing orthopyroxene and plagioclase distribution relative to 2.06 Ga reference isochrones, after Prevec *et al.* (2005)…… **4**

Figure 2.1 Simplified geological map of the Bushveld Complex. A) Far Western Limb; B) Western Limb; C) Eastern Limb; D) Northern/Potgietersrus Limb, E) Southeastern/Bethal Limb. Modified after Eales and Cawthorne (1996)……..... **7**

Figure 2.2 Simple stratigraphy of the Rustenburg Layered Suite of the Bushveld Complex with major lithological units and marker intervals. Modified after (Eales & Cawthorn, 1996; Mitchell & Scoon, 2007). **11**

Figure 2.3 Cr-saturation diagram representing Cr solubility in a magma as a function of temperature. The initial starting composition of Bushveld magmas may have been represented by P. Upon fractionation with cooling the magma may have differentiated to D. Mixing of the two magmas could result in composition M_1 which would crystallize chromite until it reaches M_2 (Murck & Cambell, 1986; CambellL & Murck, 1993)..**18**

Fig. 4.1 Photographs of mottled anorthosite and leuconorite. Both rock types have cumulus plagioclase and interstitial pyroxene. Pyroxene "mottles" are evident in the anorthosite. A & B) Anorthosite from WH-14 core and WH-31 core respectively. C & D) Leuconorite from WH-14 and WH-31 core respectively…….**28**

Fig. 4.2 Photographs of Merensky pyroxenite and Merensky pegmatoidal pyroxenite. Both rock types have cumulus pyroxene and interstitial plagioclase. A) Merensky pyroxenite from WH-14 core with crosscutting chromitite stringer. B) Merensky pyroxenite from WH-31 core with yellow disseminated sulphides. C) Merensky pegmatoidal pyroxenite from WH-14 with large plagioclase and pyroxene grains. D) Merensky pegmatoidal pyroxenite from WH-31 core with pegmatoidal features and a cm sized yellow sulphide on the right…….....…….....……**30**

Fig. 4.3 Stratigraphic column depicting the WH-14 (left) and WH-31 (right) boreholes from Winnaarshoek, Eastern Bushveld Complex. …….....…….....…….....**33**

Fig. 4.4 Photomicrographs of anorthosite and leuconorite. A) Anorthosite with cumulate euhedral laths of plagioclase and interstitial orthopyroxene from WH-31 core. B) Anorthosite from WH-14 core. C) Leuconorite with euhedral plagioclase and inter-cumulus ortho- and clinopyroxene from WH-31 core. D) Leuconorite from WH-14 core. E) Large clinopyroxene oikocryst containing orthopyroxene inclusion in leuconorite from WH-31 core. F) Cross polarized view of clinopyroxene oikocryst. …….....…….....…….....**37**

Fig. 4.5 Photomicrographs of Reef pyroxenite and pegmatoidal pyroxenite from WH-31 core. A) Orthopyroxenite with subhedral orthopyroxene and interstitial plagioclase, sulphides and phlogopite. B) Chromitite stringer with euhedral chromite and interstitial plagioclase. C) Orthopyroxenite with subhedral orthopyroxene below the chromitite stringer. D) Orthopyroxenite with rounded orthopyroxene above the chromitite stringer E) Association of phlogopite and sulphides in orthopyroxenite. F) Pegmatoidal orthopyroxenite illustrating large pegmatoidal texture in orthopyroxene and plagioclase.....**38**

Fig. 4.6 A) Photomicrograph and B) Back-scatter electron image depicting large orthopyroxene grains exhibiting clinopyroxene exsolution lamellae……..**39**

Fig. 4.7 A) Photomicrograph and B) Back-scatter electron image of clinopyroxene rims associated with (A) opx-opx grain boundaries and (B) opx-plag grain boundaries. C) Photomicrograph of orthopyroxene with inclusions especially relict plagioclase grains. D) Photomicrograph depicting plagioclase grains included or partly included in other plagioclase grains. E) Photomicrograph and F) Back-scatter electron image depicting plagioclase and orthopyroxene includeded in clinopyroxene oikocryst. Note how the orthopyroxene is irregular and being "digested' by the clinopyroxene.……...**40**

Figure 4.8 Photomicrographs depicting A) Resorbed orthopyroxene primocryst by interstitial clinopyroxene and B) resorbed plagioclase relict within resorbed orthopyroxene primocryst……**41**

Figure 4.9 A) Photomicrograph of orthopyroxene grains with clinopyroxene exsolution lamellae and discontinuous rims in the Merensky Reef pyroxenite. Orthopyroxene triple-junctions are also clearly depicted. B) BSE image depicting discontinuous clinopyroxene rims on opx-opx grain boundaries in the Reef pyroxenite. C) Photomicrograph of rounded, resorbed relict plagioclase in orthopyroxene in the Merensky Reef pyroxenite. D) Photomicrograph of irregular relict plagioclase in orthopyroxene in the Reef pyroxenite……..**42**

Figure 4.10 Photomicrographs illustrating A) rounded orthopyroxene grains included in large clinopyroxene oikocryst in the Reef pyroxenite and B) pegmatoidal pyroxenite. C) Relict orthopyroxene grain included in large plagioclase grain. D) Irregular shaped plagioclase grain included in larger plagioclase grain, possibly representing two generations of plagioclase crystallization. E) Orthopyroxene and plagioclase triple junctions in the Reef pyroxenite. F) Association of base-metal sulphides with phlogopite throughout the Reef……**43**

Figure 4.11 Photomicrographs of exsolution lamellae and discontinuous rims in the footwall unit rocks. A) Clinopyroxene exsolution lamellae and discontinuousrims on orthopyroxene. B) Clinopyroxene discontinuousrim on orthopyroxene displaying clinopyroxene twin-plane still intact as it almost completely surrounds the orthopyroxene……..…**44**

Figure 4.12 Photomicrographs and back-scatter electron images (BSE) illustrating various textures in rocks of the footwall unit. A) Resorbed plagioclase inclusions in orthopyroxene. B) BSE image of resorbed plagioclase with clinopyroxene rims in orthopyroxene. C) Resorbed plagioclase in small orthopyroxene grains. D) Coronitic texture where orthopyroxene and clinozoisite envelope olivine and vein-like plagioclase. E) Photomicrograph of corona texture with crossed polars. Note the preserved twin plane of the opx rim. F) BSE image of coronitic texture……..**45**

Figure 4.13 Photomicrographs illustrating resorbed plagioclase grains in olivine (A), irregular serpentinized olivine in association with plagioclase and orthopyroxene (B), and rounded, serpentinized olivine included in orthopyroxene (C) in the footwall leuconorite……...**46**

Figure 5.1 Plagioclase compositions in anorthosite and leuconorite of the hanging wall……..**51**

Figure 5.2 Compositions of all analyzed orthopyroxene and clinopyroxene in anorthosite and leuconorite of the hanging wall……..…**51**

Figure 5.3 Plagioclase compositions in feldspathic orthopyroxenite and pegmatoidal feldspathic pyroxenite of the Merensky Reef……..…**53**

Figure 5.4 Compositions of all analyzed orthopyroxene and clinopyroxene in feldspathic orthopyroxenite and pegmatoidal feldspathic pyroxenite of the Merensky Reef……..**53**

Figure 5.5 Plagioclase compositions in feldspathic orthopyroxenite and pegmatoidal feldspathic pyroxenite of the footwall……...**56**

Figure 5.6 Compositions of all analyzed orthopyroxene and clinopyroxene in feldspathic orthopyroxenite and pegmatoidal feldspathic pyroxenite of the footwall…….**56**

Figure 5.7 Compositions of all analyzed plagioclase in all lithologies of the Merensky Reef unit. Red symbols correspond to core compositions of that rock type's symbol, while blue symbols correspond to rim compositions of that rock type's symbol……**58**

Figure 5.8 Mean values and compositional ranges of plagioclase and orthopyroxene expressed as % An and Mg# respectively, as a function of stratigraphic height……**59**

Figure 6.1 Whole rock and mineral separate Sm-Nd isotopic data from the Merensky Cyclic Unit at Winnaarshoek of the eastern Bushveld Complex, plotted against two 2.06 Ga reference isochrons. The top reference line is represented by the equation: $y = 0.0136x + 0.50974$ with an initial ε_{Nd} value corresponding to -4.7 while the bottom reference line is represented by the equation $y = 0.0136x + 0.5096$ corresponding to an

initial ε_{Nd} value of -7.3. HW, RF and FW stand for hanging wall, Reef and footwall respectively and (WR) stands for whole rock. Labeled whole rock samples correspond to plagioclase and orthopyroxene separates……**65**

Figure 6.2 Plot of ε_{Nd} values calculated for 2.06 Ga vs. stratigraphic height of the Merensky Cyclic Unit at Winnaarshoek of the eastern Bushveld Complex, illustrating the variation in ε_{Nd} values in each unit. Note the progressive decrease in contamination from to the point of maximum contamination in the reef pegmatoid (ε_{Nd} = -8.5) to the top of the hanging (ε_{Nd} = -4.8). HW and FW stand for hanging wall and footwall respectively……**67**

Figure 6.3 $^{147}Sm/^{144}Nd$ ratios and ε_{Nd} values in measured whole rock, plagioclase and orthopyroxene at Winnaarshoek of the eastern Bushveld Complex expressed as a function of height……..……**69**

Figure 7.1 Isobaric diagrams illustrating the cotectic and peritectic curves in the An-Fo-Si system at 0.1 MPa. After (Anderson, 1915). Bivariate fields A, B and C are the fields where plagioclase first crystallization is supported. w= An-En-liq cotectic; x= plag-ol-opx-liq peritectic; y= plag-ol-liq cotectic; z= An-Si-liq cotectic……..**74**

Figure 7.2 Chondrite-normalized whole rock REE contents of the Merensky Reef at Winnarshoek in the eastern Bushveld Complex obtained from Mitchell & Scoon (2007). (a-b) represent hanging wall samples, (c-f) represent Reef samples and (f) represents the footwall……...**80**

Figure 7.3 Chondrite-normalized REE contents of (a) clinopyroxene, (b) orthopyroxene and (c) apatite from the Merensky Reef at Atok Section in the northeastern Bushveld Complex obtained by Mathez (1995)……**80**

Figure 7.4 Possible magma reservoirs and country rock contaminants plotted against the ε_{Nd} values from the Merensky Reef at Winnaarshoek. Depleted mantle from DePaolo (1981); enriched mantle from Lahaye *et al.* (1995); Archaean and Neoarchaean TTGs and granites from Schoene *et al.* (2009) and Henderson *et al.* (2000); Transvaal metapelites from Dia *et al.* (1990) and Jahn and Condie (1995); Rooiberg Suite from Buchanan *et al.* (2004)……**86**

Figure 7.5 Schematic ε_{Nd} vs Nd diagram showing the effect of fractional crystallization and mixing on cumulate rock samples from Winnaarshoek. The samples bulk Nd composition plots in the field of possible cumulate-liquid composition to the left of the liquid mixing line because $D^{Nd}<<1$ for cumulus minerals undergoing fractional crystallization processes.FC= fractional crystallization……**88**

Figure 7.6 ε_{Nd} versus Nd concentration, demonstrating mixing of a) the basal Rooiberg felsites (c. 2.06 Ga; Buchanan *et al.,* 2004) and b) Archaean TTGs (3.1-3.45 Ga; Schoene *et al.*, 2009) with depleted mantle

(DePaolo, 1981) and a B2-"like" komatiitic enriched mantle from Barberton (Lahaye *et al.,* 1995). Mixing lines are demarcated for every 5% of crustal contamination. Large symbols represent the modeled compositions for each of the contaminants (based on average) and source rocks e.g. diamond= Depleted Mantle (DM); square= B2-"like" magma; triangle= basal Rooiberg and; X= Archaean TTGs. Boxes represent the range of data for the basal Rooiberg and Archaean TTGs. ……**89**

Figure 7.7 Schematic diagrams representing some postulated models for the Merensky reef. a) Upwards percolation of magmatic fluids responsible for the precipitation of PGEs, but not expected to change the isotopic composition. b) Classic magma mixing of A- and U- type magmas to create the Reef and precipitate PGEs and Chromite. This model could cause a shift in the isotopic composition but is not expected to create the "spike" documented in this study. c) The proposed model of contamination and precipitation of PGEs and chromite prior to the emplacement of the Merensky Reef as a lateral sill following melting by a mantle plume which causes magma ascension and contamination by lower crust……..**92**

Tables

Table 5.1 Compositions of measured olivine and clinozoisite in the footwall leuconorite……**55**

Table 5.2 Mean compositions of measured clinopyroxene and orthopyroxene by type……**57**

Table 6.1 Sm-Nd whole rock and mineral separate isotope geochemistry for rocks of the Merensky Cyclic Units from Winnaarshoek in the eastern Bushveld Complex……..**66**

Table A Orthopyroxene compositions from the Merensky Reef, Winnaarshoek……**104**

Table B Clinopyroxene composistions from the Merensky Reef, Winnaarshoek……**119**

Table C Plagioclase composistions from the Merensky Reef, Winnaarshoek……...**131**

Table D Simple mass balance contamination models……..**144**

Chapter 1- Introduction

1.1 Introduction

Since being discovered in 1897, the Bushveld Igneous Complex- BIC (Fig. 2.1) has been a wealth of not only economic mineralization (platinum group elements, chromium, vanadium and iron), but of academic and scientific discovery. Having been studied for over a century by local (South African) as well as scores of international scientists, many of the mysteries of the Complex have been resolved. Innumerable aspects of the Complex have been addressed in the literature, a majority of which are directed at mineralization especially towards the Merensky Reef (e.g., Lee, 1996; Cawthorn, 1999b), the UG2 chromitite (e.g., McLaren & De Villiers, 1982; Scoon & Teigler, 1994) and more recently the Platreef in the northern lobe (e.g., Buchanan *et al.*, 1981; Kinnaird *et al.*, 2005). Detailed petrographic and petrogenetic studies as well as understanding the variations in mineral compositions across the stratigraphy also represent popular topics of study on the Complex and although much has been determined many aspects still remain enigmatic. Such aspects include, but are not limited to, the nature and formation of mineralized zones, mechanisms of emplacement and contamination as well as the genesis and composition of parent magmas; all of which are still fierce topics of debate.

The Critical Zone of the Rustenburg Layered Suite hosts both the Merensky Reef (C_uZ) and the UG2 chromitite (C_LZ) which has resulted in the extensive study of this zone. By studying this zone in particular we can glean a host of knowledge on the genesis of ore-bearing horizons in not only the Bushveld Complex but also similar layered intrusions in other parts of the world. A plethora of descriptive and mineral compositional work has been carried out on rocks of the C_UZ with few basic petrological interpretations of these data as most studies place emphasis on stratigraphic correlations and the significance of ore minerals. Despite abundant and intricate models, explanations of the genetic origins of mineralized (PGE and chromite) horizons in the Critical Zone remain elusive. The relationship between the host pyroxenite and the Cr to PGE in relation to the silicate packages above and below the mineralization is particularly problematic. Detailed evaluation of the variation of mineral composition and isotopic signatures at a grain and subgrain level is needed to attempt the

understanding of the Merensky Reef specifically. Sr isotopic work has been conducted (e.g., Kruger & Marsh, 1982; Kruger & Marsh, 1985; Lee & Butcher, 1990) which shows evidence of mixing at the top of the C_UZ and often isotopic contamination spikes related to chromitites are recorded. However, relatively little Sm-Nd work has been undertaken on rocks of the Bushveld Complex especially not in the Eastern Limb of the Complex. This is generally because the relatively low concentrations of Nd in these cumulate rocks make such work difficult and may amplify the uncertainty of the measured error in $\varepsilon_{Nd.}$ Work which has been conducted using the Sm-Nd isotope system show spikes in ε_{Nd} values in the Reef (Maier *et al.*, 2000) as well as isotopic mineral disequilibrium in the Reef lithologies (Prevec *et al.*, 2005).

1.2 Rationale and summary of existing disequilibrium literature

In this study the Sm-Nd system is favoured over that of Rb-Sr for the following reasons: the Sm-Nd system may prove to be a more effective system than that of Rb-Sr (which is completely dominated by plagioclase in mafic rocks) as it is less prone to alteration and fluid (hydrothermal and late magmatic) remobilization. It is also better balanced in terms of concentrations of Rare Earth Elements (REEs) in coexisting phases. Another advantage is that Nd also provides information about plagioclase and both ortho- and clinopyroxene, whereas Sr only provides information about plagioclase and its parent magma. Numerous studies e.g. (Eales *et al.*, 1990; Maier *et al.,* 2000; Prevec *et al.,* 2005; Seabrook *et al.*, 2005; Chutas *et al.*, 2012) have suggested that disequilibrium features exist in isotopes and/or minerals in the Merensky Reef; however this has not been done in a coherent way whereby these studies can be reconciled with one another. A new more systematic approach showing a relationship between isotopic, mineral compositional and textural variation will be a step towards unraveling the inconsistencies. Details of these previous studies are summarized below.

Eales *et al.* (1990) found discrepancies in the initial Sr values between whole rock values in a specific sample and its constituent plagioclase and orthopyroxene values. The sample had a Sr_i value of 0.7073 while orthopyroxene had values of 0.7074 and 0.7071. Cumulus plagioclase had a median value of 0.7065 while plagioclase xenocrysts had values of 0.7061 and 0.7075 (the reported analytical errors are insignificant compared to these differences in Sr_i ratios). This implies isotopic disequilibrium between plagioclase and orthopyroxene and also between different plagioclase grains

i.e. cumulus grains versus xenocrystic grains. The implications of this addressed by Eales *et al.* (1990), are that C_UZ units are composite and form during the interaction between isotopically and compositionally different liquids in accordance with models dependent on magma mixing e.g. (Irvine *et al.,* 1983; Harmer & Sharpe, 1985; Naldrett *et al.*, 1987).

Maier *et al.* (2000) reported pioneering Sm-Nd data on cumulate rocks of the Bushveld Complex. They found that rocks of the C_UZ have intermediate ε_{Nd} values in comparison to distinctly higher ε_{Nd} values in the basal ultramafic portions (ε_{Nd} = -5.3 to -6.0) and the gabbronoritic Main Zone (ε_{Nd} = -6.4 to-7.9). New Nd isotopic data on marginal rocks and sills in the floor of the complex generally interpreted as chilled parental constituents which show a larger crustal component in the upper portion of the complex are consistent with those of Maier *et al.* (2000). These variations were implied to be the result in a change in the nature of the crustal components responsible for the contamination of Bushveld magmas.

Prevec *et al.* (2005) presented Sm-Nd data suggesting that orthopyroxene (n=2) and plagioclase (n=3) in the Merensky Reef and its immediate footwall are in isotopic disequilibrium. Whole rock and orthopyroxene have ε_{Nd} values at 2.06 Ga between -7.46 and -8.46, while plagioclase has ε_{Nd} values of -1.13 to -3.37 (Fig. 1.1). This favours a model where a pre-emplaced crustally contaminated liquid results in the crystallization of orthopyroxene which then accumulates and settles into a crystal mush dominated by plagioclase. The existing plagioclase would then have crystallized from a previously relatively uncontaminated liquid. The final crystallization product would indicate that plagioclase follows orthopyroxene on the liquidus and that Archaean granitoids are possible crustal contaminants. This infers that disequilibrium resulted from the injection of a new, more crustally contaminated magma above a partially solidified liquid and is consistent with existing models for the genetic origins of the Merensky Cyclic Unit mentioned by Cawthorn (1999b).

Seabrook *et al.,* (2005) recognized that initial Sr-isotope ratios for plagioclase and Cr/MgO values for orthopyroxene in C_UZ and Main Zone rocks are markedly different. Geochemical data shows that orthopyroxene in the Merensky Reef has CZ compositions, while plagioclase compositions have signatures typical of the MZ. The implications of this mineral disequilibrium are that the two major

constituents of the Merensky Reef, plagioclase and orthopyroxene, formed from two separate but coexisting liquids. Their model infers that there was an influx of MZ magma at the base of the Merensky unit which displaced the CZ liquid upwards but did not mix with it. This displaced CZ magma crystallized orthopyroxene which sank into the underlying MZ liquid and accumulated to form the Merensky pyroxenite where plagioclase was crystallized as an interstitial phase with MZ Sr_i signatures. Their model infers that there was not significant mixing of magmas but rather a mixing of minerals from separate magmas.

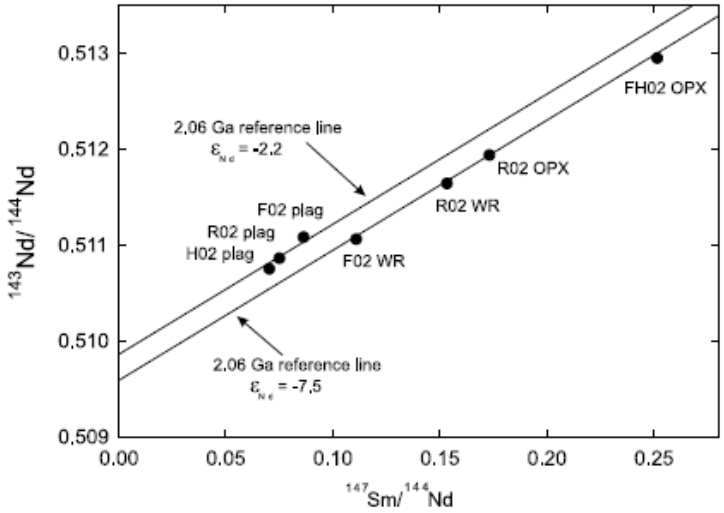

Figure 1.1 Sm-Nd Isochron diagram showing orthopyroxene and plagioclase distribution relative to 2.06 Ga reference isochrones, after Prevec *et al.* (2005).

Chutas *et al.* (2012) presented variations in Sr_i values and radiogenic Pb-isotope compositions in plagioclase and orthopyroxenes as a platform for mineral disequilibrium studies of the Merensky Reef. They used a microdrilling technique reporting data which showed that CZ plagioclase has a consistently higher Sr_i ratio and a less radiogenic $^{238}U/^{204}Pb$ composition than coexisting orthopyroxene. They reported a Sr_i ratio of 0.70506 to 0.70662 for plagioclase and ranging between 0.70290 and 0.70654 for orthopyroxene. The range in $^{238}U/^{204}Pb$ composition in coexisting plagioclase and orthopyroxene was 9.42 to 10.30 and 9.83 to 15.75, respectively. The authors infer that disequilibrium is a result of high temperature, late-magmatic processes and aim to consolidate and constrain these processes by examining the isotopic signatures in "armored" chadocrystic

plagioclase grains, comparing isotopic signatures of proximal and distal grains to microchannels, and by comparing isotopic signatures to CSD curves.

1.3 Research Aims and Objectives

Sample suites have been obtained from drill core across the Merensky Cyclic Unit from two localities in the Winnaarshoek area of the eastern Bushveld Complex. Each suite of samples represents approximately 15 samples of 10-15 cm-long half or quarter core. The two suites differ in terms of textural variation and PGE grade in the Merensky Reef. The research objective is to analyze representative samples along both transects for petrological and textural variations and from at least one transect to analyze the mineral chemistry, whole rock and mineral separate isotopic variations. This will provide an evaluation of isotopic variation emphasizing the Sm-Nd isotopic system in coexisting silicate phases from within, above and below the reef pyroxenite.

The aim of the research conducted in this study is firstly to provide evidence for disequilibrium between coexisting mineral phases in terms of variations in mineral chemistry, mineral and whole rock isotope composition or variations in mineral textures across the Merensky Reef Unit from the hanging wall through the Reef to the footwall. These data are required to compare the effects of magma-crystal mixing and will also contextualize the samples within the existing whole-rock isotopic database as well as add to the relatively little amount of available data in the Sm-Nd database for the Merensky Reef. Secondly this study aims to consolidate previous work done on disequilibrium features in the Merensky Reef by authors such as Eales *et al.*, 1990; Maier *et al.,* 2000; Prevec *et al.,* 2005; Seabrook *et al.*, 2005; and Chutas *et al.*, 2012 with the hope of contextualizing these studies (with this one) in a comprehensible manner in terms of the relationships between isotopic, mineral compositional and textural variation and the effect this may have on constraining the existing genetic models for the origin of the Merensky Reef.

Chapter 2 - Geological Setting

2.1 Regional Geology

The Bushveld Complex intruded at approximately 2060 Ma into rocks of the Transvaal Supergroup, mainly along an unconformity between the overlying Rooiberg felsites and the Magaliesburg quartzites of the Pretoria Group (Eales & Cawthorn, 1996; Viljoen & Schurmann, 1998). The Complex consists of five limbs (Fig. 2.1), four of which outcrop in disconnected regions, whereas the fifth is covered by younger sediment (Eales & Cawthorn, The Bushveld Complex, 1996). The Western Limb extends in an arc from near Thabazimbi to north of Pretoria for approximately 200km, the Eastern Limb extending from south of Stoffberg to Chuniespoort also extends approximately 200km and has better exposure than the Western Limb (Eales & Cawthorn, 1996). The Northern (Potgietersrus) Limb is somewhat hidden by younger sedimentary cover and intrusions; with good exposure confined to the eastern margin of the limb (Eales & Cawthorn, 1996; Kruger, 2005). The Far Western Limb represents an eroded remnant and has exposure west of the Pilansberg Alkaline Complex, extending to the Botswana border. The broad similarity in the succession of rock types across all three of the above mentioned areas indicates that comparable magmas were supplied to these chambers and conditions of fractional crystallization were similar (von Gruenewaldt *et al.*, 1985). The Southeastern (Bethal) Limb was identified by gravity highs and is covered by younger sediment of the Karoo sequence (Vermaak and von Gruenewaldt, 1986; Eales & Cawthorn, 1996). The entire Complex comprises the Rooiberg Group volcanic province, the Rashoop Granophyre Suite, the Lebowa Granite Suite and, the Rustenburg Layered Suite (RLS) (Vermaak & von Gruenewaldt, 1986).

2.1.1 Lithostratigraphic subdivisions of the Bushveld Complex

The Bushveld Complex is largely defined by a Felsic (Rooiberg Group, Lebowa Granite Suite and Rashoop Granophyre Suite) and Mafic (Rustenburg Layered Suite, Fig.2.2) sequence of rocks sandwiched between the older rocks of the Transvaal Supergroup and younger rocks and alluvium (Eales & Cawthorn, 1996).

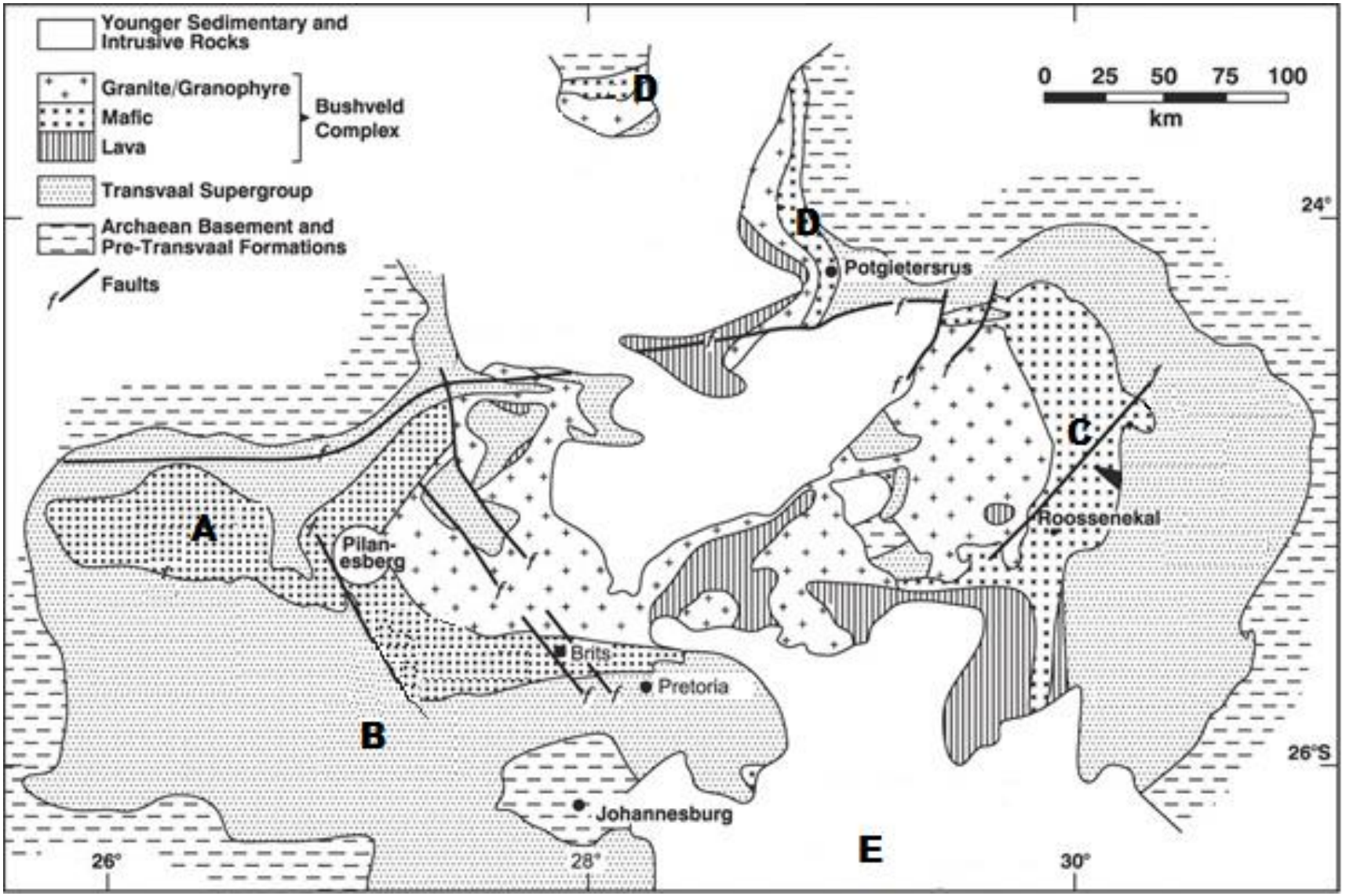

Figure 2.1 Simplified geological map of the Bushveld Complex. A) Far Western Limb; B) Western Limb; C) Eastern Limb; D) Northern/Potgietersrus Limb, E) Southeastern/Bethal Limb. Modified after Eales and Cawthorn (1996).

2.1.1.1 Felsic Suite

The Rooiberg Group

The Rooiberg Group represents the first volcanic/igneous activity associated with the Bushveld Complex and forms the roof of the feature. The Rooiberg Group is roughly 3 – 5km thick and consists from bottom to top of the Dullstroom, Damwal, Kwaggasnek, and Schrikkloof formations (Twist & French, 1983). The Dullstroom becomes more siliceous with height containing basalt interbedded with andecite, dacite and rhyolite flows; the Damwell is dominated by dacite rhyolite with approximately 68% SiO_2 content. The Kwaggasnek and Shrikkloof formations consist of rhyolites with approximately 72% and 74% SiO_2 content respectively (Schweitzer & Hatton, 1995; Buchanan *et al.*, 2002). Walraven (1997) reported a Pb-evaporation age of 2,061 ± 2 Ma for zircons separated from Kwaggasnek rhyolites, however this age is deemed to be inaccurate due to a lack of pre-treatment of the zircon grains. However, the age obtained by Walraven (1997), is still within error of the a ^{207}Pb–^{206}Pb concordia age of 2,058.9 ± 0.8 Ma obtained by Buick *et al.* (2001), on titanite grains separated from an Upper Zone xenolith.

Rashoop Granophyre Suite

The collective group of granophyre sills which exist throughout the Roof of the RLS are known as the Rashoop Granophyre Suite. They are characterised by micrographic intergrowths of quartz and microcline perthite with accessory plagioclase and mafic minerals especially hornblende (Mathez *et al.*, 2013). Walraven (1985, 1987) illustrated that different mechanisms were responsible for the genesis of the different granophyres. The largest and most extensive of which is the Stavoren Granophyre which occurs as sheets as thick as 650m thick between the RLS and the Rooiberg lavas (Walraven, 1987). The compositional characteristics of the Stavoren led Walraven (1987) to believe that it is an intrusive equivalent of rhyolites of the Kwaggasnek and Shrikkloof formations. However, a recent study by Mathez *et al.* (2013) indicates that the Stavoren Granophyres compositional fields (especially Fe-index) overlap with those of the Shrikkloof rhyolites thus making it unlikely that they are intrusive equivalents.

Lebowa Granite Suite

The Lebowa Granite Suite is the largest exposure of ferroan, anorogenic granite on Earth, occupying an area of 65,000-70,000km^2 as a shallow bowl between the eastern and western limbs of the Bushveld Complex (Hill *et al.,* 1996). The suite is composed of several sheets of granites with a combined thickness of 1.5-3.5km (Hill *et al.,* 1996). The 2,054.4 ± 1.8 Ma Nebo Granite dominates the suite and occurs between the RLS and its Rooiberg and Rashoop roof,m displaying intrusive relationships with Rooiberg rhyolites, where contacts are exposed (Walraven & Hattingh, 1993; Walraven, 1997; Mathez *et al.,* 2013). The granites show a wide range in composition from peraluminous to ferroan and metaluminous which may have been a result of basaltic liquid differentiation (Frost & Frost, 2011).

2.1.1.2 Mafic Suite

The Rustenburg Layered Suite

The collective mafic sequence of the Bushveld Complex, the Rustenburg Layered Suite (RLS), has a thickness of 7-9 km (Schiffries & Rye, 1989) and has generally been divided from base upwards into 5 zones; the Marginal, Lower (LZ), Critical (CZ), Main (MZ) and Upper (UZ) Zones (Fig. 2.2), with extensive debates regarding the exact boundaries (e.g., Kruger, 1990; Eales & Cawthorn, 1996).

The Marginal Zone

The rocks of the Marginal Zone are characterized by medium grained, although generally finer grained than those found in the interior of the Complex and often containing country rock xenoliths (Viljoen & Schurmann, 1998), unlayered, heterogeneous noritic rocks 800m thick which form the base of the Complex (Eales & Cawthorn, 1996; Viljoen & Schurmann, 1998). Vermaak (1976) suggests that the sequence of noritic rocks does not represent chilled parent magmas from the edge of the main chamber but rather represents composite sills or, evolved magmas from within the chamber which represent a distal facies. Grainsize, texture, and chemical composition suggest the norites are cumulates (Cawthorn *et al.*, 1981). Areas which do not contain marginal norite include north of Potgietersrus in the Northern Limb and near Burgersfort in the Eastern Limb where the

rocks are extremely coarse melanorites & pyroxenites and course harzburgites respectively (Eales & Cawthorn, 1996).

The Lower Zone (LZ)

The best exposure of the LZ is preserved in the Olifants River Trough in the Eastern Bushveld, and is unique in that it is the only area where all the LZ units are well developed (Eales & Cawthorn, 1996). It is composed of alternating layers of harzburgite, dunite and bronzite in a succession approximately 1700m thick (Cameron, 1978). It is in the eastern Bushveld where Cameron (1978), divided the LZ into basal feldspathic pyroxenite with minor harzburgite (max 400m), lower pyroxenite (max 400m), harzburgite (max 500m) and, upper pyroxenite (max 250m). West of Pilansburg and in the far western Bushveld the sequence of LZ rocks is essentially similar and are characterized by the absence of chromitite layers and lower chromite content is recorded in the collective rock types, whereas south of Potgietersrus, the LZ is 1600m thick and contain well-developed chromitite layers (Eales & Cawthorn, 1996). The LZ is dominated by olivine-bearing, orthopyroxene-rich rocks with accessory chromite and variable intercumulus clinopyroxene, plagioclase and biotite as indicated by drill-core from the Union Section platinum mine in the western limb (Eales & Cawthorn, 1996). In terms of cyclicity, the LZ in the Far Western limb contains nine cyclic units of dunite-harzburgite-pyroxenite approximately 1050m thick (Engelbrecht, 1985). There are 37 cyclic units of olivine-, chromite- and orthopyroxene-bearing cumulates in the LZ of the Northern limb over a thickness of 1700m and is unique wherein it is the only limb where the LZ contains significant PGEs and chromitite layers (Hulbert & von Gruenewaldt, 1985). The top of the LZ in the Western limb is defined by the termination of substantial olivine in the sequence (Teigler *et al.*, 1992), whereas the base of the CZ is controlled at the level where interstitial plagioclase in pyroxenite increases from 2% to 6% (Cameron, 1978).

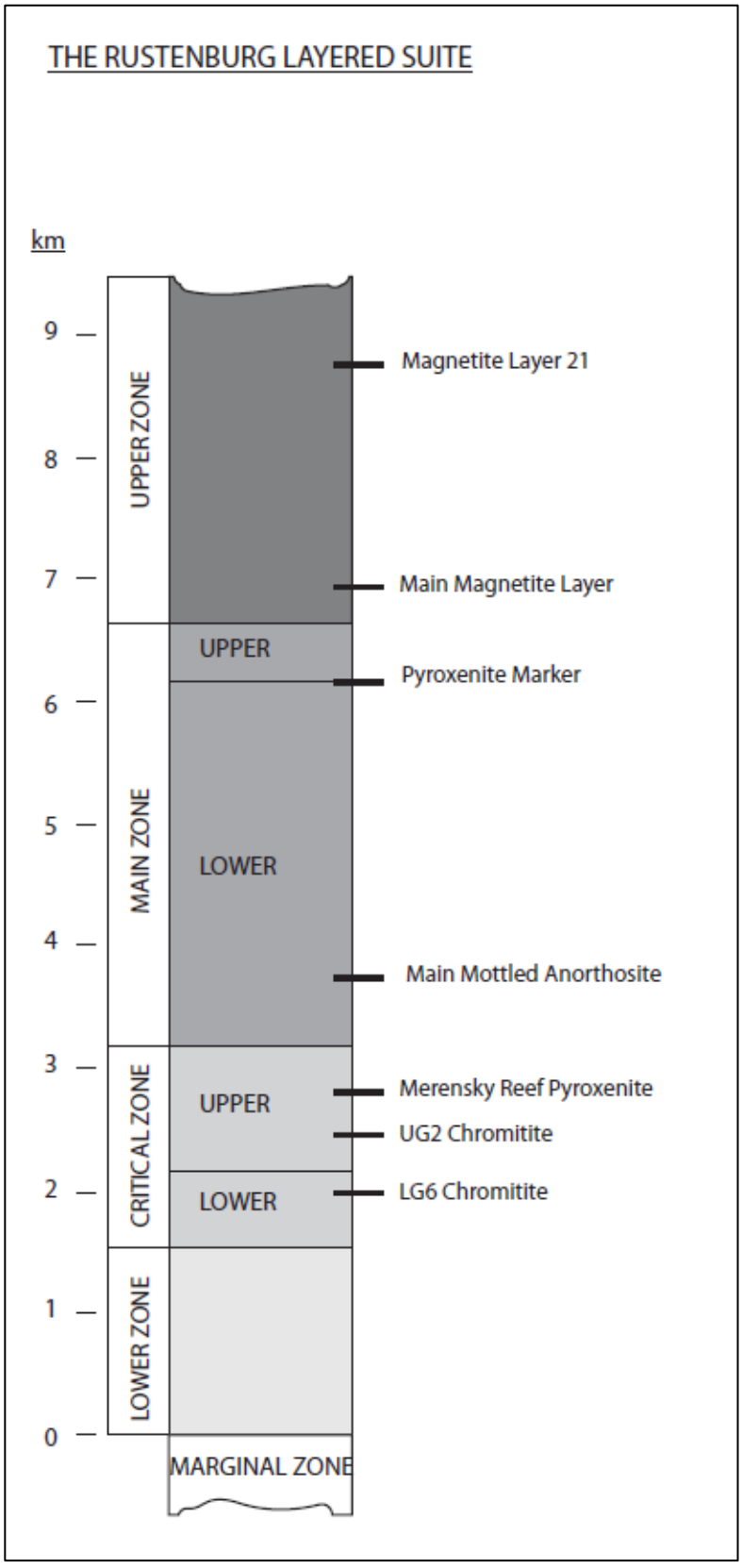

Figure 2.2 Simple stratigraphy of the Rustenburg Layered Suite of the Bushveld Complex with major lithological units and marker intervals. Modified after Eales & Cawthorn (1996) and Mitchell & Scoon (2007).

Critical Zone

The Critical Zone (CZ) is characterized by regular and rhythmic cyclicity displayed in layers of cumulus chromite within pyroxenites and olivine-rich rocks (Viljoen & Schurmann, 1998). The Upper Group 2 (UG2) chromitite and the Merensky Reef, two of the world's largest platinum-bearing ore bodies are contained within the CZ. The CZ is broadly subdivided into the Upper CZ (C_UZ) and the Lower CZ (C_LZ). The C_LZ is composed mostly of bronzitites, with lesser chromitites, dunites and harzburgites (Cameron, 1982). Cumulus phases include bronzite, olivine, and chromite; however, plagioclase, augite, phlogopite, k-feldspar and quartz are postcumulus phases (Cameron, 1982). Conversely, more than 70 percent of the stratigraphic thickness of the C_UZ is composed of norites and consists of 8 cyclic units hosting partial or complete sequences from ultramafic base cumulates through norite to anorthosite (Cameron, 1982; von Gruenewaldt *et al.*, 1985; Eales & Cawthorn, 1996). Chromitite and chromite-silicates are only present in discrete intervals while bronzitites and anorthosites are secondary constituents (Cameron, 1982). Plagioclase and bronzite occur as the principal cumulus minerals with secondary clinopyroxene and/or chromite and can occur as postcumulus minerals along with augite, phlogopite, k-feldspar and quartz (Cameron, 1982; Eales & Cawthorn, 1996). The CZ in the central portion of the Bushveld Complex reaches a maximum thickness of approximately 1500m, which generally tapers out to about 800m in the eastern and western Bushveld (Vermaak & von Gruenewaldt, 1986). Huge reserves of chromite and chromitite seams, some which are associated with significant PGE mineralization especially the UG-2, are also contained within the Critical Zone (CZ). These are known as the Lower (LG), Middle (MG) and Upper (UG) Group chromitite layers and are individually labeled from the base upwards as LG1-7, MG1-4 and UG1-2 (Eales & Cawthorn, 1996). The UG3 only exists in the eastern Bushveld. The first appearance of cumulus plagioclase-bearing rocks occurs between the MG2 and 3 chromitites, marking the transition from the C_LZ to the C_UZ (Eales & Cawthorn, 1996). This is seen in the Eastern limb and most of the Western limb. The Bushveld Complex contains 25 chromitite layers, all of which are hosted in the CZ (Viljoen & Schurmann, 1998) of which the thickest exceed 1m (Eales & Cawthorn, 1996).

In terms of mineralization, the CZ can be sub-divided based on grades and reef-type mineralization. The units (which show considerable variation in thickness) from bottom to top include 1) the UG-1, 2) The UG-2 3) the Merensky Reef and 4) the Bastard units (Cameron, 1982) the latter two being briefly discussed below.

a) The Merensky Reef

The Merensky Cyclic Unit contains basal chromitite, pyroxenite (pegmatoidal pyroxenite in the western Bushveld), norite and anorthosite (Eales & Cawthorn, 1996). Typically the reef is composed of 70% orthopyroxene, 20% plagioclase, 4% clinopyroxene, 2% biotite, 3% quartz, chromite and sulphides (Brynard *et al.*, 1976). The Merensky Reef itself contains up to 10 g/t PGE, usually in conjunction with roughly 3 percent base metal sulphides and associated platinum group minerals (PGM). The thickness is variable ranging between 4cm and 4m (up to 12m thick in parts of the eastern Bushveld) in some instances and a range in dip of 9° to 27° (Brynard *et al.*, 1976; Lee, 1996). The reef occurs at the Critical Zone-Main Zone boundary where the Merensky pyroxenite forms the base of the Merensky cyclic unit (Seabrook *et* al., 2005). It is within this pyroxenite where the majority of the reefs mineralization exists and it (the reef) occurs as a discrete unconformable boundary (Seabrook *et* al., 2005). The main economic mineralization is defined by 2-4 chromitite stringers which define both the upper and lower limits of the reef, but are not always present especially in the eastern Bushveld (Cameron, 1982; Lee, 1996). The lower chromitite band (3 to 5mm thick) defines the base of the reef with a sharp undulating contact with anorthosite grading into spotted anorthosite with depth (Brynard *et al.*, 1976). The upper chromitite band generally occurs 0.3 – 1.3m below the gradational contact of melanorite overlain by spotted anorthosite (Brynard *et al.*, 1976).

b) The UG2 chromitite layer

Like the Merensky Reef, the UG2 chromitite layer is one of the world's primary PGE enriched deposits if not the largest PGE resource (Vermaak & von Gruenewaldt, 1986). It is found within 15 to 400m below the Merensky Reef with variation more prolific in the eastern lobe than the western lobe (Viljoen & Schurmann, 1998). The layer itself can be traced across the eastern and western lobes of the Bushveld Complex for over 400km with only minor interruption along strike (McLaren & De Villiers, 1982). In the central sector of the eastern Bushveld the UG2 chromitite attains a thickness of 70 to 150cm (averages less than 1m over the entire Bushveld Complex) and is composed of 75-90% modal chromite inter mixed with plagioclase (Eales & Cawthorn, 1996; Mondal & Mathez, 2007). The dip of the UG2 layer varies between 10° and 26° with a portion reaching a dip of 65° in the northwestern lobe (Viljoen & Schurmann, 1998). Anorthosite sometimes

forms the footwall of the UG2 but most commonly it overlies a coarse melanorite or feldspathic pyroxenite (Viljoen & Schurmann, 1998). Leader chromitite stringers (10 to 12 cm thick) are frequently dispersed within the immediate vicinity of the main UG2 seam hanging wall feldspathic pyroxenite (Viljoen & Schurmann, 1998). The PGE contents of the UG2 range between 3.5 to 19.2 ppm with PGMs concentrated towards the base of the UG2 horizon as well as towards the middle to upper contact (Lee, 1996).

Main Zone

The main Zone (MZ) consists mostly of norites grading upwards into gabbronorites. The Pyroxenite Marker is a distinctive layer of pyroxenite located two thirds of the way up the MZ which contrast with several mottled anorthosite layers found in the lower portion (Viljoen & Schurmann, 1998) and which are confined to the Main Mottled and Upper Mottled Anorthosites (Eales & Cawthorn, 1996). The MZ is a thick succession approximately 2800m-thick and is relatively homogenous compared to other subdivisions of the Rustenburg Layered Suite (Eales & Cawthorn, 1996). In comparison to the CZ, the MZ is without the fine-scale rhythmic layering and lithological complexity, being bereft of both olivine and chromian spinel (Eales & Cawthorn, 1996). Although, Molyneux (1974), recorded one case of fine-scale layering within the MZ in the Eastern limb of the Complex. Von Gruenewaldt (1973), divided the MZ into three sectors, the upper and lower of which contain primary orthopyroxene while the central sector contains pigeonite. A second subdivision exists proposed by, Mitchell (1990), dividing the MZ into the lower Main Zone (M_LZ) which is comprised of 11 norite units, overlain by 4 Gabbronorite units and the upper Main Zone (M_UZ) where gabbronorite appears first wedged between the porphyritic Gabbro Marker and the Main Mottled Anorthosite. The two units are separated by the Pyroxenite Marker (Mitchell, 1990).

Upper Zone

The Upper Zone (UZ) is defined at its base by the first appearance of cumulus magnetite above the Pyroxenite Marker (Eales & Cawthorn, 1996; Viljoen & Schurmann, 1998). The UZ is 2000m thick and is well layered in some sections. 25 magnetitite layers are found within the UZ, the most significant of which is the 2m thick Main Magnetitite Layer, which is mined for its 1.3% V_2O_3 content (Eales & Cawthorn, 1996). SACS (1980) has divided the UZ into 3 subzones. Subzone *a* is

comprised of three thin magnetitite layers near the base with a further 700m thick sequence of anorthosite and ferrogabbro. The Main Magnetitite Layer is found 130m above the base, with a further seven magnetitite layers overlying it. Subzone *b* is 580m thick and defined at its base at the appearance of iron-rich cumulus olivine. A further seven magnetitite layers are hosted by anorthosite, troctolite, and olivine and magnetite ferrogabbro. The appearance of apatite as an additional cumulus phase marks the base of Subzone *c* where plagioclase composition becomes more sodic than An_{50}. This 1000m thick sequence is composed of olivine diorite, anorthosite, magnetite-rich diorite and another seven magnetite layers.

2.2 Genetic Models

2.2.1 Origins of the UCZ

The relevance of the Marginal Zone as a possible parent magma has widely been disputed based on the complexity of its constituent rock types and the variable cumulus enrichment indicating that their compositions are not representative of magmas (Eales & Cawthorn, 1996). However, recent works illustrate, using new Nd isotope data, that marginal rocks and sills in the floor of complex are representative of chilled parental magmas influenced by large amounts of crustal contamination (Maier *et al.,* 2000). Richardson & Shirey (2008) propose an alternate view stating that the isotopic character is not a result of *in situ* contamination but is inherited from the lithospheric mantle. Sharpe (1981), used field relationships and geographic proximity of the marginal rocks applied to different sections of the layered suite to correlate magma types and infer that the Marginal Zone was not parental but rather a precursor to the main intrusion.

Sharpe (1981), recognized border facies N and B2 from base to top of the CZ which are confined to the CZ as neither occurs along the CZ-LZ or LZ-Marginal Zone contact. The appearance of both these border phases above the LZ is indicative of a new pulse of magma. The primary liquid of this pulse was chilled along the contacts of the Marginal Zone where the pulse was forced to penetrate (Sharpe, 1981). Further penetration along the fracture planes allowed for mixing with cooler host rocks, followed by mixing of the bulk magma with LZ residuum and resulting in the fractionation and formation of the CZ (Sharpe, 1981). The B2 border facies formed as the bulk liquid chilled against the floor remelting the pre-existing N facies and forming sills on the floor (Sharpe, 1981). A

discrete magma has been suggested as the CZ parent, however, its low (200ppm) Cr content is inconsistent compared with the Cr budget of the intrusion (Sharpe, 1981). Davies & Cawthorn (1984) identified an appropriate magma type in the western Bushveld occurring as a discordant microgabbronorite intruding CZ and Marginal Zone rocks. The composition was deemed to be very similar to Sharpe's (1981) CZ magma.

Recently some authors have provided models for an ultramafic parent e.g. (Eales, 2000; Maier *et al.*, 2000; Eales & Costin, 2012). Work by Hatton (1995) and Hatton & Schweitzer (1995) recognized the source of the Bushveld Complex and overlying Rooiberg Group to be a rising diapir of mantle-derived magma which entered the crust and formed a cover of silicious liquid as a result of crustal melting. Eales & Costin (2012), propose a similar yet complementary model whereby a komatiitic magma, contaminated by crustal assimilation, was emplaced at depth into a staging chamber beneath the site where the Bushveld Complex originally formed. The model requires that the crystallizing magma was emplaced into a reservoir where crystal growth is accelerated with ascent and cooling of the magma. In this contaminated komatiite, crystallisation of olivine, orthopyroxene, and accessory chrome spinel would take place between 1,600°C and 1680°C at approximately 10 kbar (Eales & Costin, 2012). Fractionation trends through the Marginal Zone to the LZ and C_LZ over intervals up to 120m result in more primitive compositions suggestive of mixing of residual magma with irregular additions of less evolved batches (Eales & Costin, 2012).

2.2.2 Genetic Models

2.2.2.1 Chromite ores

Magma Mixing

Magma addition and mixing models for the genesis of chromitite layers still remain the most popular, with most authors adopting Irvine's (1977) model based on the Muskox Intrusion and other layered intrusions. When applying Irvine's model to the Bushveld Complex, he suggests the injection of a primitive magma (type 1) which mixed with a slightly differentiated resident magma. This progression is best illustrated on a Cr-saturation diagram from (Murck & Campbell, 1986), shown in Figure 2.3). The starting composition of the primitive type 1 magma is given by P which changes to composition D as a result of cooling and differentiation. More magma of composition P

would be added to the magma chamber where P and D mixed to form M_1. M_1 becomes oversaturated in Cr, forming chromite grains until the composition falls to M_2. The problem with this model is that in order to produce a layer even 1m thick with a loss of 100ppm Cr (as shown in the diagram) would require the mixing of 4 to 5km of magma (Campbell & Murck, 1993). In order to achieve this on a scale of 30 000km^2 would require instantaneous mixing, due to the sharp nature of the UG2 basal contacts, which is considered unlikely (Cawthorn, 2010). Another model questioning the abruptness of the event creating such sharp basal contacts over large areas is proposed by Kinnaird *et al.* (2002), which show that every chromitite layer was associated with an increase in Sr-isotope ratios, where assimilation of a crustal component was ascribed as the reason for the increased ratio. In the model Kinnaird *et al.* (2002), attribute the anomalously low ratios in the succession above the chromitites, to chromite crystals descending from the roof of the intrusion carrying residual liquid with higher Sr isotope ratios, accounting for higher values in the chromitites than the overlying rocks.

Injection of a chromite slurry

Eales (2000) adopted a model allowing for the injection of a crystal-charged chromite slurry which evolved in a deeper magma chamber and undergoing crystallization. The model strove to resolve the following problems surrounding the layered sequence:

The high average Cr content of the LZ and CZ could be explained by the addition of excess Cr in the form of chromite microphenocryst suspensions.

a) The scarcity of adequate volumes of Cr-depleted residua in the layered sequence above the CZ might be explained by their having been trapped in the lower chamber.
b) The need to postulate large volumes of magnesian liquids in the Bushveld chamber, as a means to account for the high average Cr levels of the CZ, becomes redundant.
c) The large decline in Cr content that occurs across the CZ/LZ boundary need not be explained solely in terms of Rayleigh fractionation of parent magma in the chamber.
d) If the hypothesis of mixing of primitive and evolved magmatic liquids to bring about Cr super saturation is valid, it would be expected that the Mg# of cumulates above and below chromitite layers would be different. This is commonly not the case as we see see variations

of alternating Mg# which increase and decrease in intervals across the LZ and C_LZ cumulates. This ultimately suggests that the abundance of chromitites in the Bushveld Complex cannot have resulted from liquid mixing alone.

Some of the issues surrounding this model are that first, the model does not account for an imbalance in elements other than Cr (i.e. it only accounts for disproportionate amounts of Cr) and so problems exist with the mass balance calculations regarding the lower half of the Bushveld Complex (Cawthorn, 2010). Secondly, the chromitite layers show significant lateral uniformity of thickness across the Complex with little evidence for thinning. This does not seem plausible as the chromite-enriched slurry would presumably be emplaced near the site of entry resulting in the significant thinning of the layers with distance (Cawthorn, 2010).

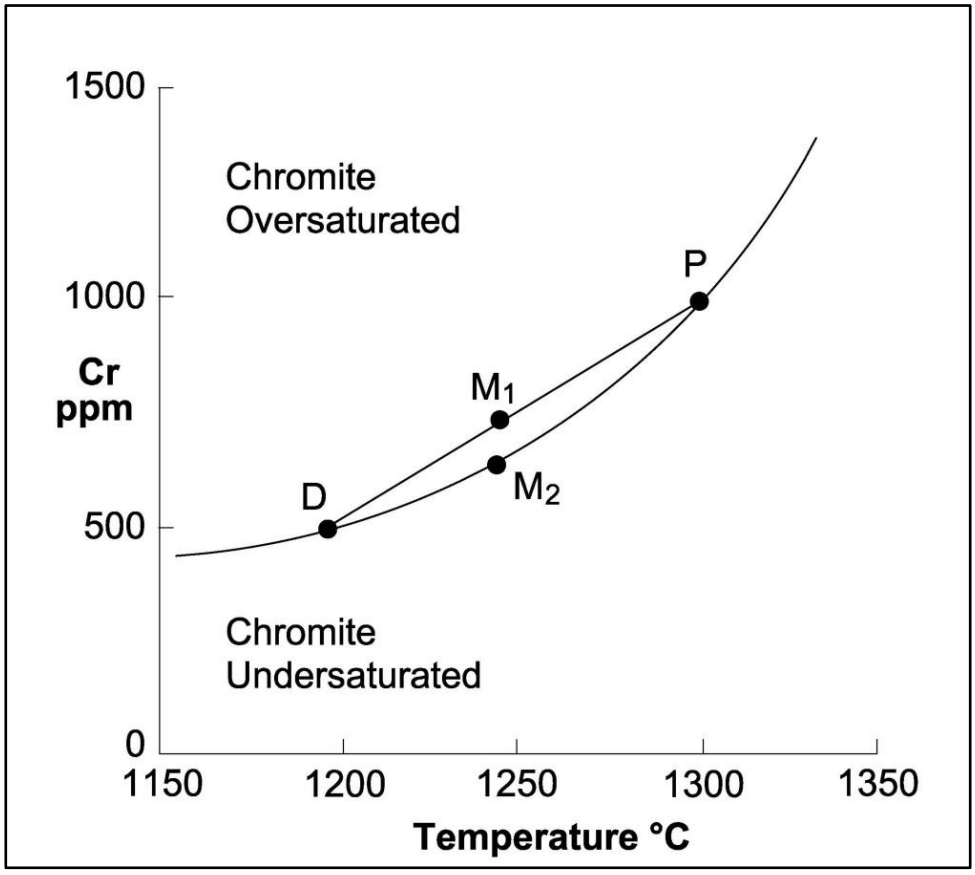

Figure 2.3 Cr-saturation diagram representing Cr solubility in a magma as a function of temperature. The initial starting composition of Bushveld magmas may have been represented by P. Upon fractionation with cooling the magma may have differentiated to D. Mixing of the two magmas could result in composition M_1 which would crystallize chromite until it reaches M_2 (Murck & Campbell, 1986; Cambell & Murck, 1993).

Pressure Change

The most relevant pressure change model was put forward by Lipin (1993), which accounts for mass balance problems by invoking an instantaneous pressure change across the entirety of the magma chamber, allowing production of chromite as an across-the-board pressure change would drive the magma into the chromite field. This would however, show no affect in the magmatic system other than a change in the paragenetic sequence of minerals, making it a near impossible model to test realistically (Cawthorn, 2010). Another problem is that the roof of the magma chamber in a complex as large as the Bushveld would float on the magma as opposed to being a rigid 'cap' confining the pressure which results from basal pressure increasing mechanisms (Eales & Cawthorn, 1996).

2.2.2.2 The Merensky Reef- PGE/ Sulphide ores

The Bushveld Platinum-Group-Mineral (PGM) deposits are categorized as follows:

- PGMs hosted within iron-rich cores of pipe-like bodies of olivine-rich rock that transgress layering,
- PGMs within various sulphide mineral-bearing layers in the LZ, MZ and UZ,
- PGMs within all the chromitite layers and seems of the LG, MG as well as UG1 Chromitite Layer,
- PGMs hosted by the UG2 Chromitite Layer and,
- PGMs hosted by the Merensky Reef and associated rocks

A number of genetic models and hypotheses have been proposed for the origin of PGE mineralization. The following section concentrates on the latter two classes as mentioned above, whilst reviewing the variable models.

Fluid Facilitated Remelting

Nicholson & Mathez (1991) proposed a qualitative model whereby the assemblages were originally composed of a leuconorite overlain by a partially molten pyroxenite. The hypothesis holds that the reef formed by hydration mechanisms resulting in the melting of the partially molten protolith. Nicholson & Mathez (1991) invoked the degassing of a volatile component which migrated upwards through the solid underlying rocks by means of fractures. This volatile component is then added to the pyroxenite resulting in remelting and recrystallization. Cooling and inward crystallization of the remelted zone result in the mineral paragenitic sequences observed.

Upward Infiltration of Fluid

Boudreau (2008) presented a more quantitative model based on that proposed by (Nicholson & Mathez, 1991) of hydration melting of pyroxenite in conjunction with mass and heat diffusion. Boudreau's model is a multi-stage process involving the following conditions. Footwall rocks accumulated to form great thicknesses, where a water-rich vapour was created by the last stage of crystallization of the residual magma. The liquid dissolved portions of any PGE and sulphides encountered as it ascends. The vapour eventually encounters a crystal mush where the interstitial magma was undersaturated in water. The vapour (with its sulphur and PGE) then dissolved into the interstitial magma. Precipitation of PGE-enriched sulphides resulted from the water acting as a flux and causing remelting. The process can also be used to explain the formation of the coarse-grained textures associated with the pegmatoidal pyroxenite. Cawthorn (2010) addressed two problems with this model. Firstly, PGE mineralization can occur below or above the pegmatoidal pyroxenite and Boudreau's model requires that the mineralization be confined in association to the pegmatitic layer. Secondly, if there is significant remelting of the original layer, the overlying package would have collapsed into it or the volatile-enriched magma would have migrated upwards as a result of density contrasts. There is very little evidence supporting those observations therefore it remains unclear if the event represents infiltration of magma or simply crystal mush deformation.

Magma Mixing- Downward accumulation of a PGE-enriched sulphide liquid

Several models have been proposed which advocate an immiscible sulphide liquid as the key scavenging agent of base and precious metals (e.g. Naldrett, 1989). The common association of PGE and sulphides led Naldrett (1989) to suggest that the immiscible sulphide liquid was able to scavenge base and precious metals by separating from the silicate melt. The model has been applied quite successfully to explain the Cu and Ni contents in an assortment of magmatic base-metal sulphide deposits, by using the partition coefficients of both the sulphide and silicate liquids. Although the model is useful when applied to Cu, Ni and S, complications arise when PGE are taken into consideration. Firstly, the concentration of PGE in in silicate magmas is very low (typically ppb) and secondly it is difficult to acquire reliable values for the partition coefficient for PGE because once experimental values for partition coefficients are obtained they often show different results (Cawthorn, 1999b).

PGE and Chromite association

The fact that PGE and chromitite layers have an intrinsic relationship is undisputed as all chromitite layers contain aberrantly high PGE contents. Capobianco *et al.* (1994) presented experimental and mineralogical evidence supporting a model suggesting PGE is present in the chromite in solid solution, resulting in the geochemical association. Evidence includes the identification of PGM within chromite grains which are attributed to exsolution due to high initial concentration in the chromite during cooling (Capobianco *et al.,* 1994). Another model by Scoon & Teigler (1994), proposed that platinum minerals were trapped by chromite and then transported as suspended grains to the base of the chamber. This mechanism cannot be the only mechanism involved as the Platreef only contains chromite as a minor phase, suggesting there must be another process to consider (Cawthorn, 1999b).

Chapter 3- Sampling, Methodology and Analytical methods

3.1 Sampling Strategy

Drill core from two boreholes were provided by Roger Scoon from Winnaarshoek (property of Impala Platinum's Marula platinum mine) in the eastern Bushveld Complex. The selected drill cores are WH14 and WH31. These particular two cores were selected because they show a variation in the reef mineralization with WH14 representing a restricted low-grade reef type, while WH31 represents a wider, more richly mineralized reef zone. Both cores were logged and photographed. Nine thin section sites were selected from WH14 from sites of interest based on initial macroscopic thoughts as well as to maintain a sequence from the hanging wall through the reef to the footwall. A similar strategy was conducted in selecting 11 thin sections from the WH31 core with an additional 19 sample sites for isotopic analysis. The isotopic sites included 6 sites in the hanging wall (H1-H6), 8 sites in the Reef (R1-R8) and 5 sites in the footwall (F1-F5). The Reef samples were taken over centimeter intervals to map variations through the reef, while the hanging wall and footwall samples were representatively mapped over 4-5 meters.

3.2 Sample preparation

3.2.1 Crushing

The 19 selected samples for isotope work were first cleaned with water and acetone. Samples ranged from 20-25 cm lengths of half core (especially in hanging and footwall) to 5 cm lengths of quarter core (especially in the reef). Samples were crushed into smaller 1-2 cm sized chips by using a Osborn-Massco laboratory jaw-crusher, before being pulverized into a fine powder by the Herzog swing-mill for 3 minutes per sample. The plates of the jaw crusher and the rings of the swing-mill were cleaned with water and dried with acetone and an air compressor after each sample. Several "quartz runs" were added to the swing-mill to avoid contamination across different rock types.

3.2.2 Mineral Separation

Six sample sites were selected to conduct mineral separate experiments where 2 samples were selected from each of the hanging wall, Reef and footwall. The samples were first cleaned with water and acetone before being broken into smaller chips by using the Osborn-Massco laboratory jaw-crusher. The chips were ground in a Cook & Sons roller mill yielding smaller grain fractions ranging from fine powder to millimeter sized grains. The grains were washed in a beaker in order to separate the powder and suspended particles from larger grains. The powder was discarded and the grains left to dry in an oven at 90 °C. Once dry the grains were sorted into different size fractions. Sorting by sieving was achieved by use of 4 stacked cups with different sized nylon mesh at the base of each cup. The nylon mesh sizes from the base to the top of the sieve stack were; 50 μm, 100 μm, 200 μm and 300 μm. The grains were added to the top of the stack and then shaken manually to isolate the desired grain sizes (100μm and 200μm).

Magnetic mineral species were removed with aid of a hand magnet before the sorted grains were propelled through a Cook & Sons magnetic separator in order to initially separate plagioclase grains from pyroxene grains. Various amplitudes and slope settings were applied to process the grains more efficiently. The settings which achieved the best separation were: slope angle = 15°; tilt angle = 10°; and amplitude = 1.0 amperes. Initially vibration speed is set to high to achieve rough separation into 2 groups of mixed plagioclase and pyroxene which are then continually reprocessed at slower vibration speeds to refine the sorting.

Once sorted macroscopically into pure plagioclase and pyroxene, a pure 200 μg of each mineral from each sample was required. This was acquired by adding ethanol to each separate and picking out the 200 μg of pure sample with tweezers or a pipette under a binocular microscope. The culmination of this process yielded 10 mineral separates comprising 6 plagioclase and 4 orthopyroxene samples.

3.2.3 Electron Micro-Probe Sample preparation

The eleven thin sections from the WH31 core were polished and carbon coated for Electron Micro-probe analysis (EMPA). Unsatisfactorily polished samples were resubmitted until a good, consistent polish was acquired for each thin section. Samples were then carbon coated with a coating thickness of 25 μm.

3.2.4 Isotopic sample preparation

The 19 powder samples were packaged and sent to the University of Cape Town for Nd isotopic compositions, and Sm and Nd concentrations analysed by isotope dilution at the AEON-UCT ICP-MS-MC Lab at the University of Cape Town, Rondebosch, South Africa. The procedure is completed as follows:

Nd analysis by MC-ICP-MS technique:

Rock powder was digested by concentrated HF:HNO3 for approximately 48 hours at 140ºC in closed Teflon beakers which were then dried down and converted to nitrate. Concentrated HNO_3 enamel digestion then takes place for 1 hour at 140ºC in closed Teflon beakers. The sequential Sr and Nd separation process then took place following the procedures of Míková & Denková (2007) after Pin & Zalduegui (1997) and Pin et al. (1994).

3.3 Analytical work

3.3.1 Petrography

Petrological observations were made using a Leica binocular microscope in conjunction with a Leica digital microscope camera to acquire photomicrographs. Photomicrographs were processed using the Leica Application Suite software v1.4.0.

3.3.2 Electron Micro-Probe Analysis

EMPA data acquisition was performed at Rhodes University, Department of Geology, on a JEOL JXA 8230 Superprobe, using 4 WD spectrometers. The analytical conditions were as follows: probe current 20 nA, acceleration voltage 15 kV, counting time 10 seconds on peak and 5 seconds on background (20 secs and 10 secs, respectively for Sr and Ba and 30 secs and 15 secs, respectively for Ni), beam size spot <1 micron. Natural standards were used for measuring the characteristic X-rays. The ZAF matrix correction method was employed for quantification.

In analyzed minerals the following standards were used for all silicates: Plag-An65_SPI for Ca (Diopside_SPI_W in pyroxene and olivine), Albite_SPI for Na and Al (Almandine_SPI for Na in pyroxene), Rhodonite_SPI for Mn, Fayalite_USNM_85276 for Fe^{3+} and Fe^{2+} (Almandine_SPI for Fe^{2+} in olivine), Orthoclase_SPI for for K, Celestite_SPI for Sr, Barite_SPI for Ba, Diopside_SPI_W for Mg (Kaersutite_SPI in olivine), Olivine_SPI for Si , Cromite_SPI for Cr, Rutile_SPI for Ti and Nickel_Silicide_SPI for Ni.

3.3.3 Isotopic Analysis

Sm-Nd isotopic analysis was performed on a Nu Instruments NuPlasma HR in the MC-ICP-MS facility housed in the Department of Geological Sciences, University of Cape Town, Rondebosch, South Africa. Nd isotopes were analysed as 50 ppb 2% HNO_3 solutions using Nu Instruments DSN-100 desolvating nebulizer. The JNdi-1 was employed as a reference standard and $^{143}Nd/^{144}Nd$ was normalized to a value of 0.512115 after Tanaka *et al.* (2000) and gave an average of 0.51267 ± 4 on n=6 (2 s on 31 measurements). Nd isotopic compositions were corrected for Sm and Ce interference using the measured signal for ^{147}Sm and ^{140}Ce, and natural Sm and Ce isotope

abundances as well as for instrumental mass fractionation using the exponential law and a $^{146}Nd/^{144}Nd$ normalization value of 0.7219. ε_{Nd} values were calculated for 2.06 Ga using values for CHUR of $^{147}Sm/^{144}Nd=0.1967$ and $^{143}Nd/^{144}Nd=0.512638$ (Jacobsen and Wasserburg, 1980). Two duplicate whole rock samples were analyzed showing slight changes in measured values (Table 6.1); however these fall within the range of reproducibility reported earlier.

Chapter 4- Petrography

4.1 Macroscopy

4.1.1 Lithostratigraphy

The sample set comprises four different types of intrusive igneous rocks, namely anorthosite, leuconorite, pyroxenite and pegmatoidal pyroxenite as described below.

Anorthosite

Anorthosite (Fig. 4.1 A&B) occurs both overlying the hanging wall leuconorite and underlying the footwall leuconorite in the WH-14 core. The anorthosite is a medium-grained mottled anorthosite with interstitial pyroxene crystals forming the "mottles" within cumulus plagioclase. Where the "mottles" are absent the pyroxene grains are more widely dispersed and are here termed "spotted" anorthosite (Eales & Cawthorn, 1996). Plagioclase dominates the rock accounting for approximately 90% while pyroxene and possibly biotite account for the remaining 10%. Plagioclase grains are somewhat uniform occurring as 0.5- 2 mm subhedral crystals displaying lath-like and tabular habits. Plagioclase also occurs dispersed among the interstitial orthopyroxene mottles. Pyroxene crystals are subhedral to euhedral and up to 2.5 mm in size displaying a poikilitic habit.

Leuconorite

Leuconorite (Fig. 4.1 C&D) occurs as hanging wall in both core sets and occurs below footwall pyroxenite in WH-31. The leuconorite is coarse grained with crystals up to 15mm in size. It is light grey in colour and composed of approximately 80% euhedral plagioclase and 20% interstitial orthopyroxene. Plagioclase occurs as white/grey subhedral laths ranging up to 15 mm in size. Orthopyroxene occurs as brown subhedral grains up to 15 mm in size.

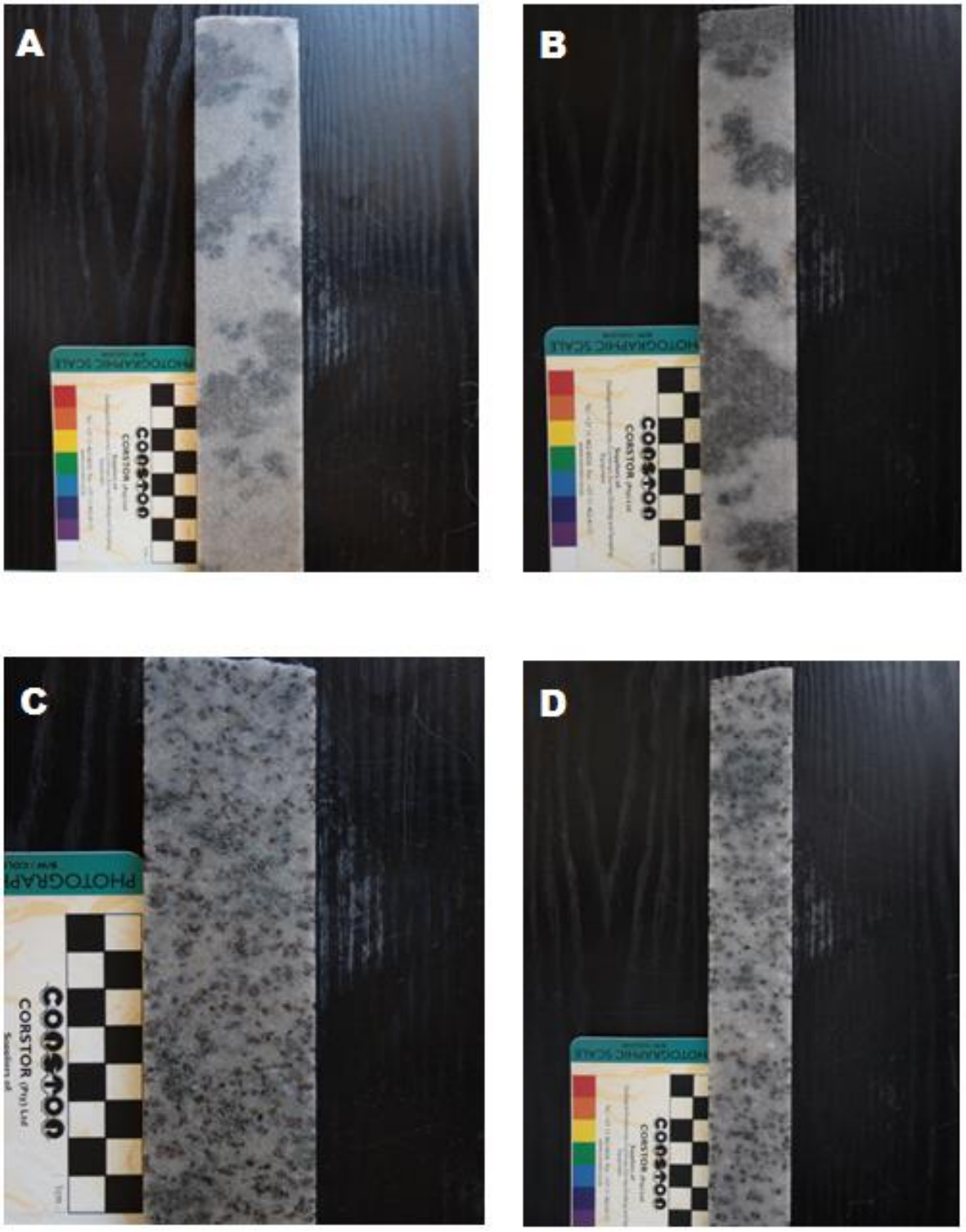

Fig. 4.1 Photographs of mottled anorthosite and leuconorite. Both rock types have cumulus plagioclase and interstitial pyroxene. Pyroxene "mottles" are evident in the anorthosite. A & B) Anorthosite from WH-14 core and WH-31 core respectively. C & D) Leuconorite from WH-14 and WH-31 core respectively.

Merensky Reef pyroxenite

The Merensky pyroxenite (Fig. 4.2 A&B) is a feldspathic orthopyroxenite, often referred to as a poikilitic pyroxenite (Eales & Cawthorn, 1996). It is medium-grained with crystals up to 10 mm in size. It is composed of approximately 85% brown/black euhedral orthopyroxene (up to 10 mm), 5% dark green interstitial clinopyroxene (up to 5 mm) 9% white/grey interstitial plagioclase (up to 10 mm) and 1% yellow/brown sulphides (up to 2 mm). Both species of pyroxene are subhedral, sometimes euhedral while plagioclase is subhedral occurring as laths. Sulphides occur as small disseminated grains variably distributed across the pyroxenite.

Merensky Reef pegmatoidal pyroxenite

The Merensky Reef pegmatoidal pyroxenite (Fig. 4.2 C&D) is very coarse grained orthopyroxenite with individual crystals up to 35 mm in size. It is mostly composed of approximately 85% anhedral to subhedral brown/black orthopyroxene (up to 25 mm), 9% interstitial plagioclase (up to 20mm) and 5% large discrete subhedral to euhedral dark green clinopyroxene oikocrysts (up to 35 mm). Accessory minerals include some micas, chromites and disseminated sulphides The presence of pegmatoidal texture and hydrous phases may suggest that some fluid–facilitated modification has taken place resulting in the obviously larger grain sizes compared to 'normal' pyroxenite.

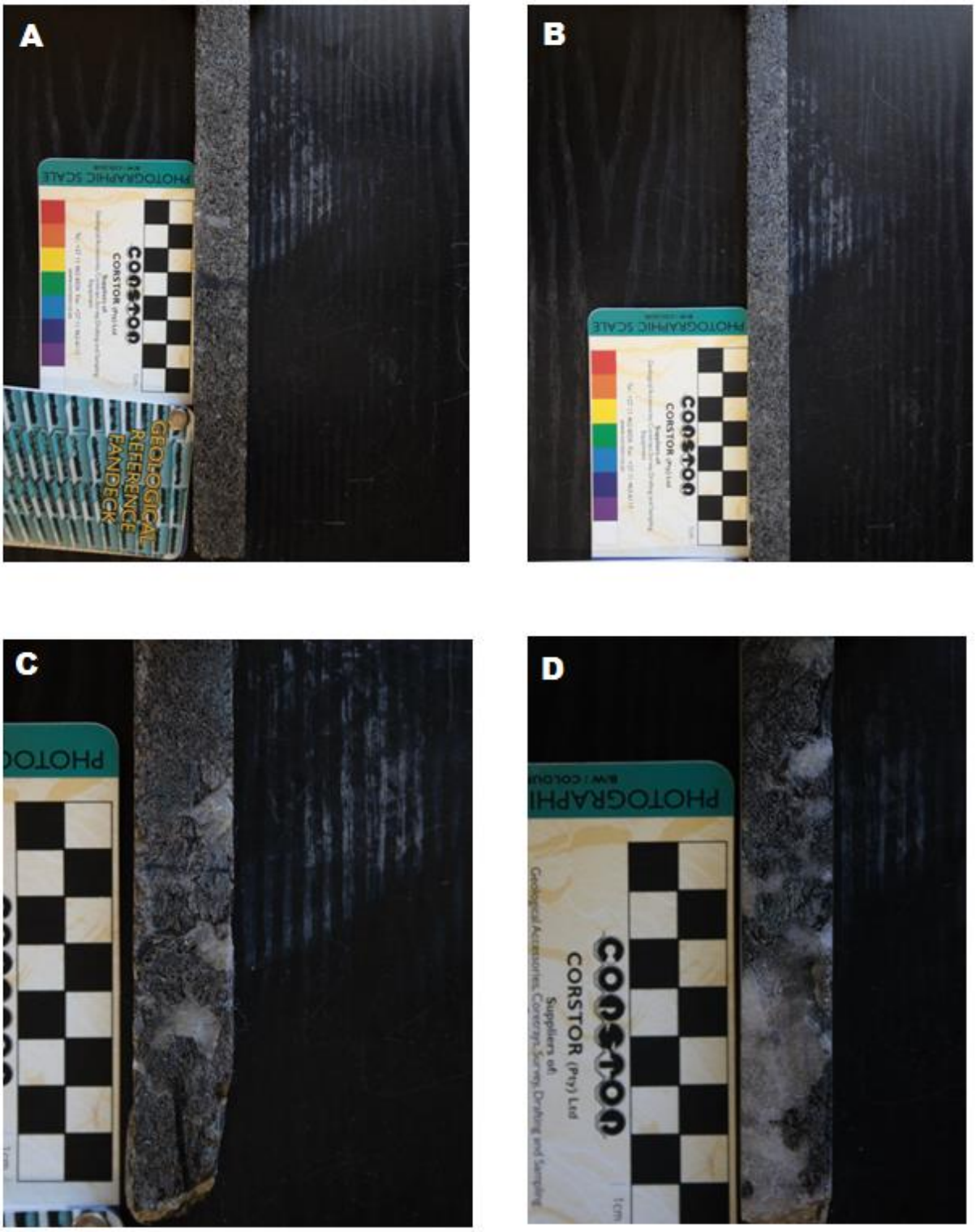

Fig. 4.2 Photographs of Merensky pyroxenite and Merensky pegmatoidal pyroxenite. Both rock types have cumulus pyroxene and interstitial plagioclase. A) Merensky pyroxenite from WH-14 core with crosscutting chromitite stringer. B) Merensky pyroxenite from WH-31 core with yellow disseminated sulphides. C) Merensky pegmatoidal pyroxenite from WH-14 with large plagioclase and pyroxene grains. D) Merensky pegmatoidal pyroxenite from WH-31 core with pegmatoidal features and a cm sized yellow sulphide on the right.

4.1.2 Core Log Descriptions

The following section uses the term cumulus, cumulate and intercumulate frequently. It is therefore defined here as follows after Eales (2001): Cumulus crystals are those which crystallized from a melt at an early stage and were allowed to grow to a large size as they were uninhibited by neighboring crystal boundaries during growth. A rock with a high proportion of cumulus crystals is termed a cumulate. Interstitial crystals are those crystals which crystallize from the residual liquid and fill the spaces between the cumulate assemblages.

WH-14

The WH-14 sample set (Fig. 4.3) is consist of just less than 10m of core from a depth of 49.7- 59.3 m. Mottled anorthosite was found between 49.7-54.0 m. Plagioclase dominates and is cumulus-textured while orthopyroxene occurs in patches and is not yet a cumulus phase. Between 52.3- 54.0 m the amount of orthopyroxene increases and slowly grades into cumulate orthopyroxene, at greater depth becoming a spotted anorthosite. This is followed by approximately 1m of leuconorite between 54.0- 55.1 m where both plagioclase and orthopyroxene are euhedral and grades into the Reef pyroxenite. The mottled anorthosite and leuconorite form the hanging wall with the Reef itself occurring between 55.2-56.5 m. The Reef is composed of two relatively thin (± 30cm) discrete pegmatoidal pyroxenite layers alternating with feldspathic pyroxenite (Fig. 4.3). Initially a few millimeter-sized sulphides are present but more sulphides are found with greater depth. A 5 mm-thick chromitite stringer (marking the upper Merensky chromitite stringer) crosscuts the pyroxenite (Fig. 4.3.) and it is noted that fewer sulphides occur above the stringer than below. The pegmatoidal pyroxenite contains plagioclase, orthopyroxene and large centimeter-sized blebs of clinopyroxene before it grades into 'normal' equigranular pyroxenite. The footwall is composed of approximately 4 m of pyroxenite with a few interspersed sulphides which diminish with depth. Centimeter-sized oikocrysts of clinoproxene occur within the pyroxenite, and pegmatoidal pyroxenite can still be found, albeit scarcely.

WH-31

The WH-31 sample set (Fig. 4.3) is composed of approximately 12.5 m of core from a depth of 187.5 m to 200.0 m. Similar to the WH-14 core, WH-31 starts with approximately 3 m (from 187.5-190.8 m) of mottled anorthosite dominated by cumulus-textured plagioclase with patchy interstitial orthopyroxene. The orthopyroxene content increases with depth gradually becoming cumulate. Where mottles are absent the anothosite takes on a spottled-texture with pyroxenes variably distributed. This is followed by just over a meter of leuconorite between 190.8-192.0 m where both plagioclase and orthopyroxene are cumulus phases. Once again the anorthosite and leuconorite form the hanging wall before grading into the Reef pyroxenite. The Merensky Reef occurs between 192.1-194.1 m which is slightly thicker than the Reef at WH-14. The contact with the hanging wall is irregular and wavy occurring at 192.04 m. The upper chromitite stringer is approximately is 5 mm thick, sub-parallel with ± 25° dip occurring at 192.3 m while the lower stringer is absent from this intersection. Disseminated sulphides occur variably throughout the feldspathic pyroxenite and pegmatoidal pyroxenite which occurs between 194.1- 194.4 m and contains abundant plagioclase with orthopyroxene and clinopyroxene oikocrysts. Only one pegmatoidal section is found in the WH-31 log in comparison to WH-14 which has two distinct layers of pegmatoid (Fig. 4.3). The footwall is composed of regular orthopyroxenite between 194.4- 200.0 m and is sparsely sulphide bearing. This is followed by leuconorite which slowly grades back into anorthosite over the remainder of the core for approximately 4 m.

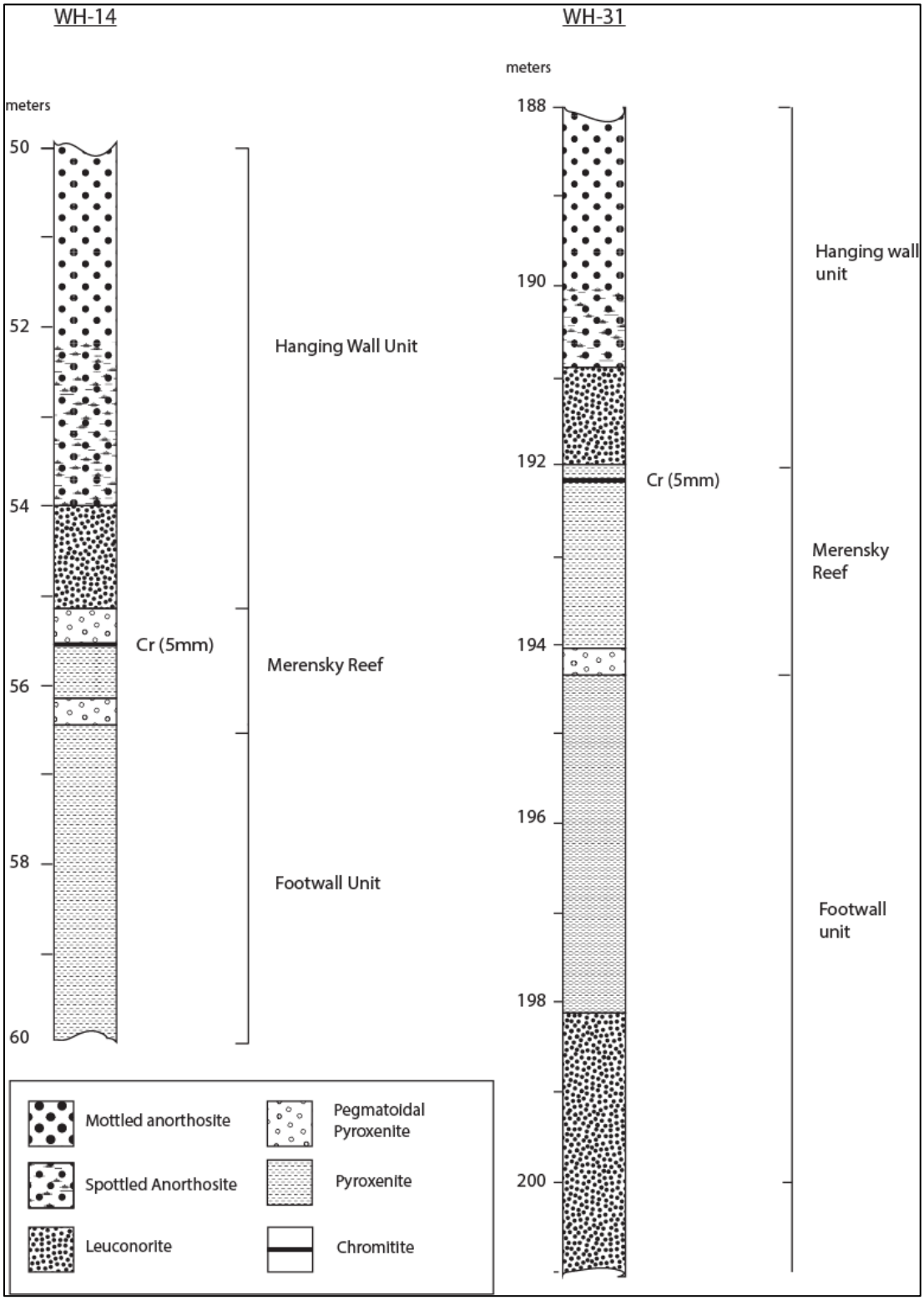

Fig. 4.3 Stratigraphic column depicting the WH-14 (left) and WH-31 (right) boreholes from Winnaarshoek, Eastern Bushveld Complex.

4.2 Microscopy and Petrography

4.2.1 Overview

This section describes an overview of the rock types present in the sample suite at a microscopic scale. It includes detailed descriptions of the petrography and mineralogy of the rocks present. Rock types which repeat over the stratigraphic sequence in the sample suite (i.e. occur in hanging wall and then again in footwall are discussed together, except where any specific textural differences may occur).

Anorthosite

In general the anorthositic samples in the hanging wall unit are composed of a majority of euhedral plagioclase with sparse interstitial orthopyroxene and in some instances accessory clinopyroxene (Fig. 4.4 A&B). Plagioclase is adcumulate and composed of grains with both lath and tabular habits which occur as medium sized (up to 3.5 mm) euhedral primocrysts as well as subhedral interstitial grains. Orthopyroxene occurs as interstitial material in the form of anhedral to subhedral grains (max. 1mm). Clinopyroxene is rare but where present it occurs as tiny (max. 100 μm) interstitial grains, as exsolution lamellae in larger orthopyroxene grains or as discontinuous rims around orthopyroxene. Anorthosite in the footwall unit is almost the same as that in the hanging wall unit except that interstitial orthopyroxene is more common and their grain size is generally larger (up to 150 mm). Some of the larger orthopyroxene grains contain small (100-200 μm) subhedral plagioclase inclusions.

Leuconorite

Anorthosite slowly grades in leuconorite as the pyroxene content of the rock increases with depth. The anorthosite-leuconorite contact is therefore gradational. Leuconorite in the hanging wall unit is composed of approximately 80% euhedral plagioclase and 20% interstitial orthopyroxene, clinopyroxene with some accessory olivine (Fig. 4.4 C&D). Plagioclase occurs as subhedral laths (up to 13 mm) often with rounded edges and also as smaller interstitial grains. Orthopyroxene still

occurs as an intercumulate phase as both large (up to 12 mm) discrete grains as well smaller grains dispersed among other interstitial phases. Orthopyroxene is generally subhedral but also sometimes occurs as irregular habits. Clinopyroxene is more abundant in the leuconorite as compared with the overlying anorthosite. It generally occurs as interstitial grains as well as exsolution lamellae and discontinuous rims in association with orthopyroxene but also as large (up to 2 cm) discrete oikocrysts (Fig. 4.4 E&F). Olivine, where present, usually occurs as small (100-150 μm) grains in association with orthopyroxene. Leuconorite in the footwall package is similar to that in the hanging wall unit although there are some discrepancies. Some plagioclase grains reach centimeters in size and often contain orthopyroxene as inclusions. Ophitic orthopyroxene containing plagioclase chadocrysts are also more common in the footwall leuconorite. Phlogopite also occurs in leuconorites of the footwall package where as it is seemingly absent in the hanging wall leuconorites.

Merensky Reef Pyroxenite

The Reef pyroxenite (feldspathic) is dominated by euhedral orthopyroxene (approx. 80%) with interstitial plagioclase and clinopyroxene and is therefore a feldspathic orthopyroxenite (Fig. 4.5 A). Phlogopite, K-feldspar and base-metal sulphides often occur as accessory phases. Chromite is also present comprising the thin 5 mm upper Merensky Reef chromitite stringer (Fig. 4.5 B). The chromitite is composed of chromite occurring as coarse (up to 3 mm) sub- to anhedral grains with interstitial silicate minerals. Plagioclase dominates the interstitial silicate phases along with lesser, almost rare orthopyroxene grains. Orthopyroxene in the feldspathic orthopyroxenite forms the cumulus phase (adcumulate) consisting of sub- to euhedral (Fig. 4.5 C), medium-grained (20-40 mm) crystals which are often rounded (Fig. 4.5 D). Euhedral crystals are generally associated with base-metal sulphides especially near the chromitite stringer. Plagioclase occurs as patches of interstitial material up to 2 cm in diameter while clinopyroxene occurs as large (1.5 –2 cm) dispersed oikocrysts. The most common base-metal sulphides are chalcopyrite, pyrrhotite and pentlandite and occur dispersed throughout the Reef zone but are more commonly associated near the chromitite stringer. Phlogopite is most commonly found associated with sulphide minerals, often forming intergrowths (Fig. 4.5 E).

Pegmatoidal Pyroxenite

The Reef pyroxenite- pegmatoid contact is gradational as medium-sized grain texture is gradually replaced with the large pegmatoidal texture seen in orthopyroxene and plagioclase especially (Fig. 4.5 F). The pegmatoidal pyroxenite is very similar to the Reef pyroxenite in terms of mineralogy but is set apart by its very coarse-grained texture. It is composed of coarse euhedral orthopyroxene with interstitial plagioclase and clinopyroxene. Olivine is also sometimes present and represents an accessory phase along with interstitial phlogopite, K-feldspar, quartz and dispersed sulphides. Orthopyroxene is generally anhedral to subhedral in shape and often occur as rounded grains up to 3 cm in size. Plagioclase occurs as subhedral (often irregular) laths or needles up to 1.5 cm in size or in patches of interstitial material up to 3 cm in diameter. Plagioclase chadocrysts enclosed orthopyroxene oikocrysts is uncommon. Clinopyroxene is mostly found as discrete anhedral to subhedral oikocrysts up to 2 cm in size. Phlogopite is the most commonly occurring accessory mineral in the pegmatoid and occurs interstitially as anhedral to subhedral grains up to 2 mm in size. The most common sulphides are chalcopyrite, pyrrhotite and pentlandite.

4.2.1 Microtextures

Several microtextures are evident throughout the sample suite. Some textures occur in the hanging wall, footwall and Reef units; while some textures are confined to specific units. Specific attention is paid to disequilibrium textures in order to attempt to constrain the paragenetic sequence and help determine the mode of magmatism responsible for the Merensky Unit. Such disequilibrium textures include: discontinuous rims, orthopyroxene rims on olivine, resorbed plagioclase in ortho- and clinopyroxene, resorbtion of orthopyroxene primocrysts by clinopyroxene, corona textures and orthopyroxene inclusions in plagioclase and vice-versa. Microtextures are discussed in the units in which they occur as follows:

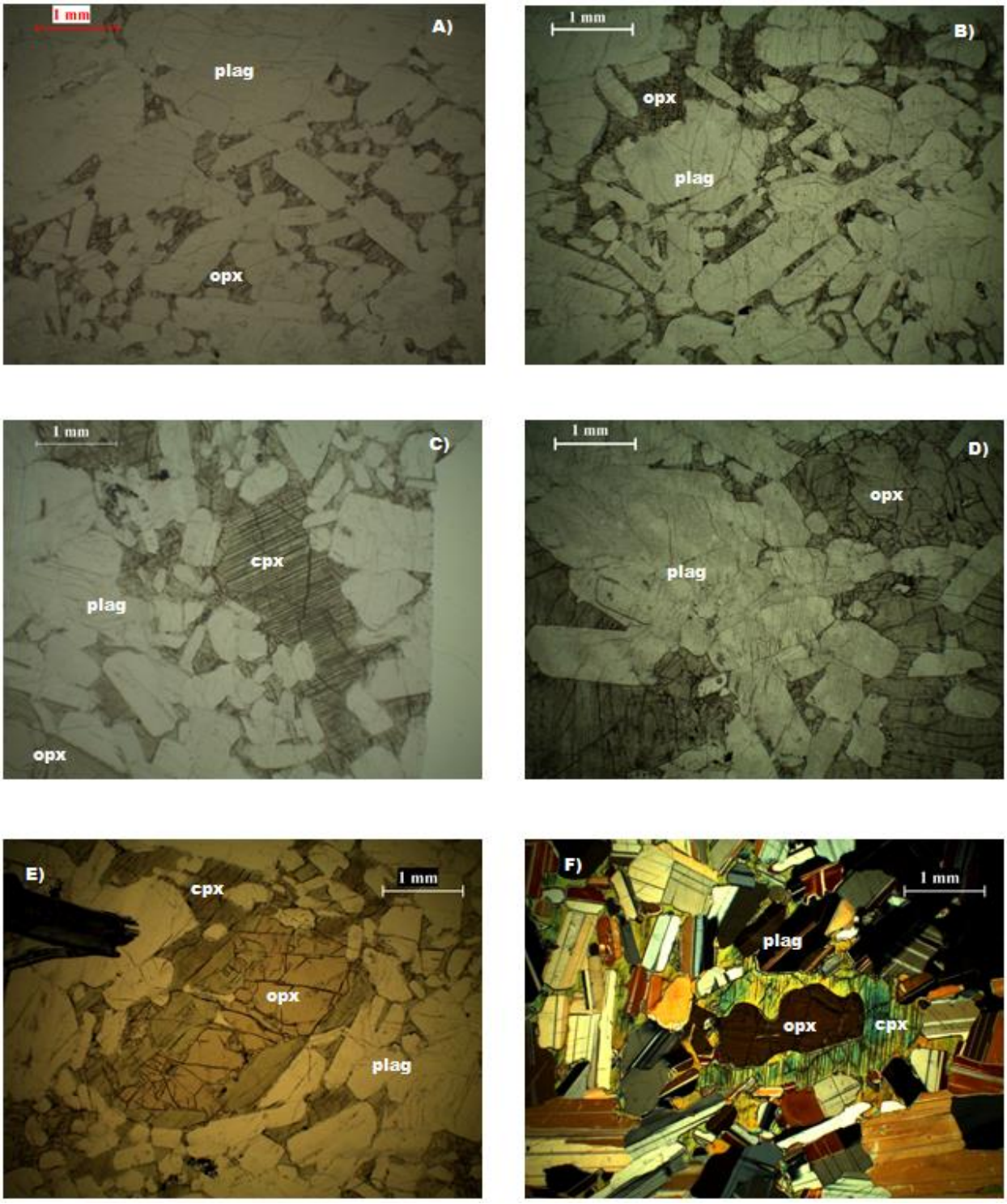

Fig. 4.4 Photomicrographs of anorthosite and leuconorite. A) Anorthosite with cumulate euhedral laths of plagioclase and intercumulus orthopyroxene from WH-31 core. B) Anorthosite from WH-14 core. C) Leuconorite with cumulus plagioclase and inter-cumulus ortho- and clinopyroxene from WH-31 core. D) Leuconorite from WH-14 core. E) Large clinopyroxene oikocryst containing orthopyroxene inclusion in leuconorite from WH-31 core. F) Cross polarized view of clinopyroxene oikocryst.

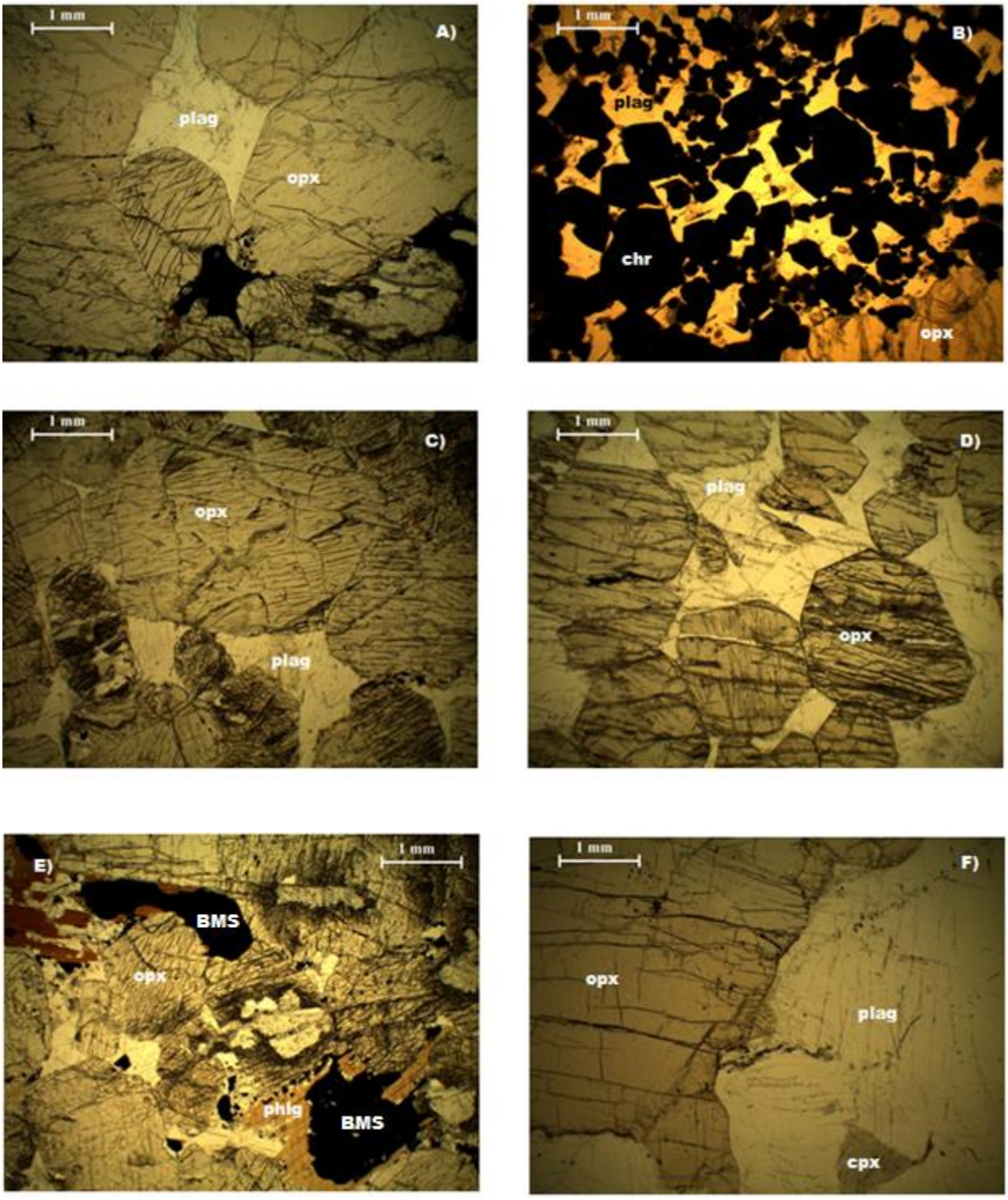

Fig. 4.5 Photomicrographs of Reef pyroxenite and pegmatoidal pyroxenite from WH-31 core. A) Orthopyroxenite with subhedral cumulus orthopyroxene and intercumulus plagioclase, sulphides and phlogopite. B) Chromitite stringer with euhedral chromite and interstitial plagioclase. C) Orthopyroxenite with subhedral orthopyroxene below the chromitite stringer. D) Orthopyroxenite with rounded orthopyroxene above the chromitite stringer E) Association of phlogopite and sulphides in orthopyroxenite. F) Pegmatoidal orthopyroxenite illustrating large pegmatoidal texture in orthopyroxene and plagioclase.

4.2.1.1 Hanging Wall

The most commonly occuring microtextures in the hanging wall rocks are the clinopyroxene exsolution lamellae in orthopyroxene (Fig. 4.6 A&B). They are common throughout the hanging wall unit and generally occur oriented with the orthopyroxene cleavage planes. They do not tend to show a bias in their formation as they occur in isolated orthopyroxene grains among euhedral plagioclase as well as in grains which share intergranular boundaries with other orthopyroxenes. Discontinuous clinopyroxene partially surrounding grain boundaries (Fig. 4.7 A&B) are often associated, but not limited to orthopyroxenes containing lamellae and tend to show bias towards orthopyroxene-orthopyroxene grain boundaries. Plagioclase relicts included in orthopyroxene (Fig. 4.7 C) are uncommon but some instances do occur especially closer to the Reef contact. The same is true for plagioclase grains included in other plagioclase grains (Fig. 4.7 D) which also only occur in leuconorite closer to the Reef. Perhaps the most interesting textures in the hanging wall are the large clinopyroxene oikocrysts (Fig. 4.7 E&F) which occur in the leuconorites. The oikocrysts contain inclusions of both plagioclase and orthopyroxene. While the plagioclase grains maintain their sub- to euhedral lath-like habit, the orthopyroxenes are often irregular, anhedral and partly digested by the enclosing clinopyroxene (Fig. 4.7 E&F). These inclusions are not only confined to clinopyroxene oikocrysts but also occur in interstial clinopyroxene as resorbed orthopyroxene primocrysts (Fig. 4.8 A) which often have relict plagioclase inclusions as well (Fig. 4.8 B).

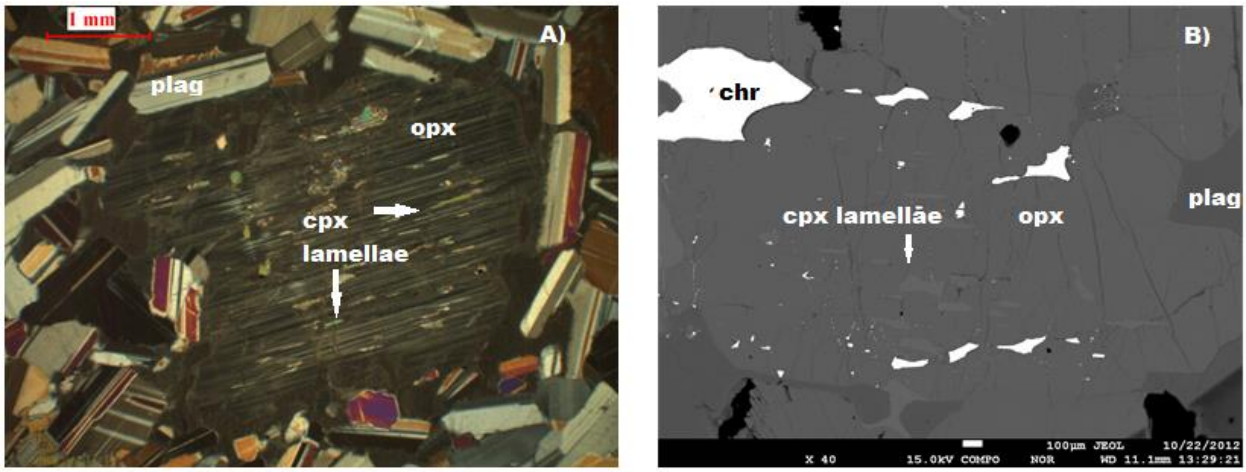

Fig. 4.6 A) Photomicrograph and B) Back-scatter electron image depicting large orthopyroxene grains exhibiting clinopyroxene exsolution lamellae.

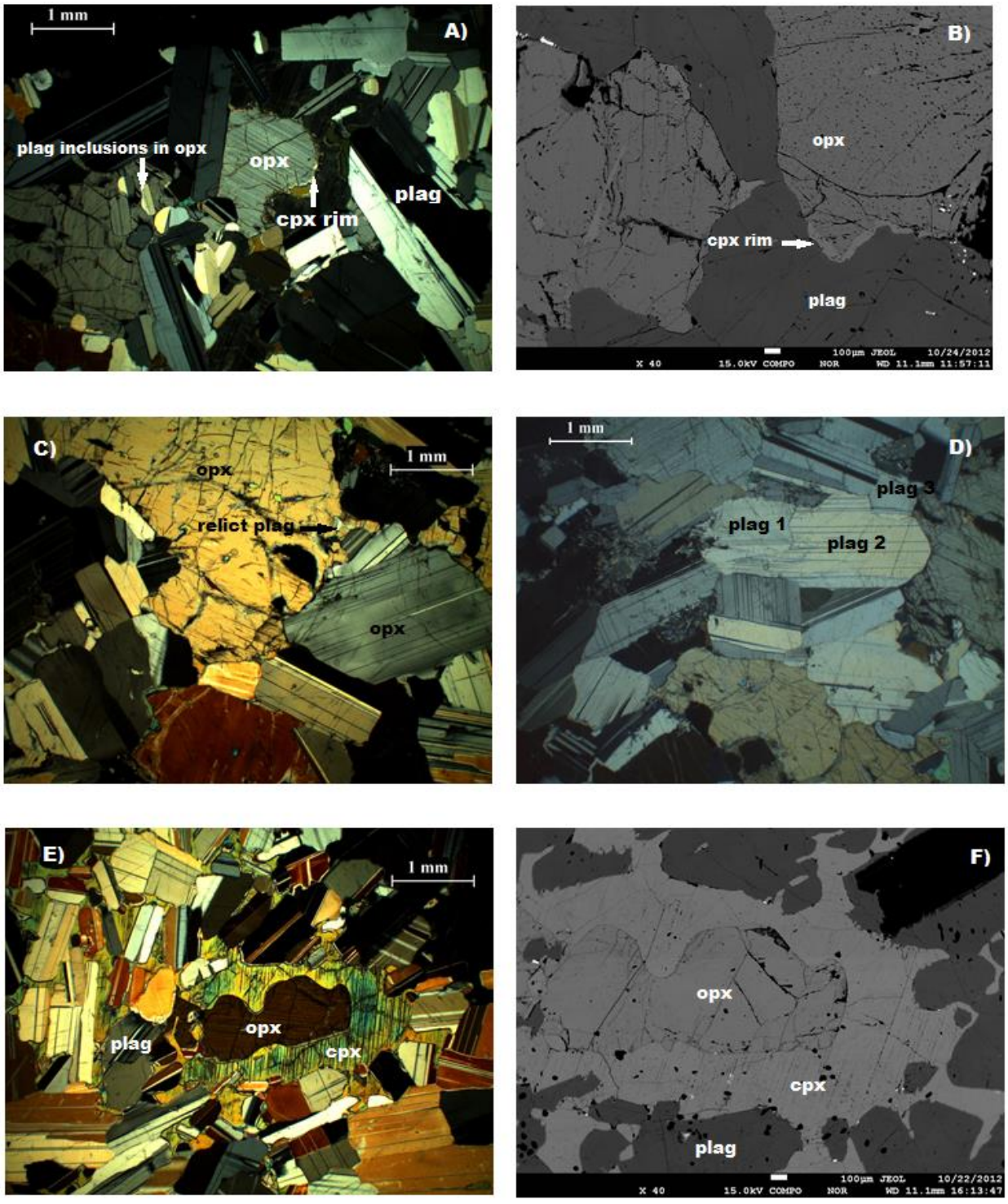

Fig. 4.7 A) Photomicrograph and B) Back-scatter electron image of clinopyroxene rims associated with (A) opx-opx grain boundaries and (B) opx-plag grain boundaries. C) Photomicrograph of orthopyroxene with inclusions especially relict plagioclase grains. D) Photomicrograph depicting plagioclase grains included or partly included in other plagioclase grains. E) Photomicrograph and F) Back-scatter electron image depicting plagioclase and orthopyroxene includeded in clinopyroxene oikocryst. Note how the orthopyroxene is irregular and being “digested’ by the clinopyroxene.

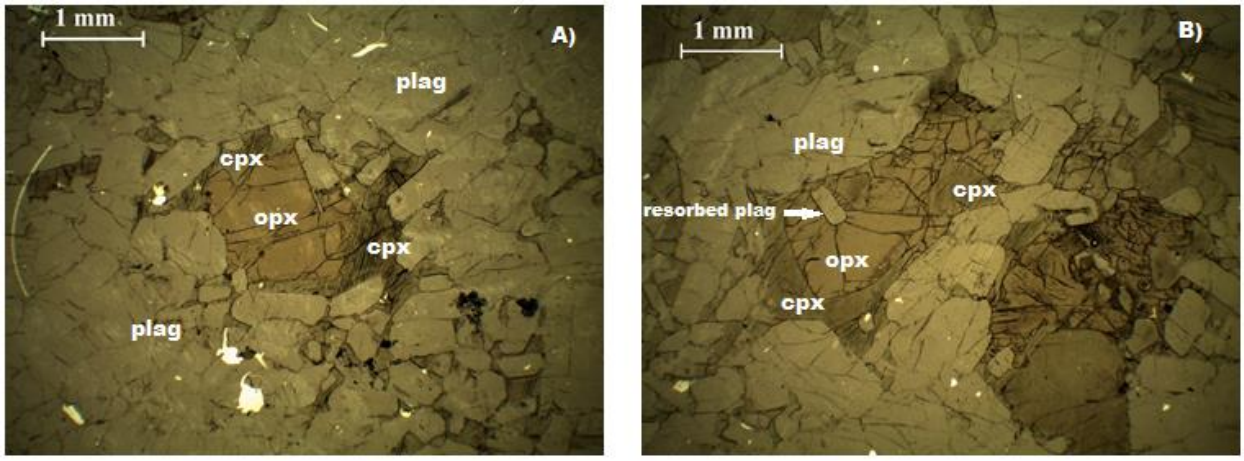

Figure 4.8 Photomicrographs depicting A) Resorbed orthopyroxene primocryst by interstitial clinopyroxene and B) resorbed plagioclase relict within resorbed orthopyroxene primocryst.

4.2.1.2 Merensky Reef and Reef Pegmatoid

As with the rocks of the hanging wall unit, the most common texture occurring in the Reef are the clinopyroxene exsolution lamellae and discontinuous rims on orthopyroxene (Fig. 4.9 A&B). In the case of the Reef however, a majority of the orthopyroxene grains are heavily exsolved (Fig. 4.9A) especially in those samples closer to the hanging wall contact. Large, irregular exsolutions are often found in occurrence throughout the Reef. Clinopyroxene reaction rims are also commonly found partly enclosing orthopyroxene grains, especially and more profoundly, at opx-opx grain boundaries as opposed to opx-plag grain boundaries (Fig. 4.9B). Resorbed plagioclase is frequently found as chadocrysts in orthopyroxene grains. These plagioclase relicts are usually rounded (Fig. 4.9C) however, irregular plagioclase relicts are also present (Fig. 4.9D). It is not uncommon for these resorbed plagioclase relicts to maintain their well-developed twin planes, especially in rounded grains (Fig. 4.9C). Orthopyroxene can also occur as irregular, rounded or sub-rounded inclusions in orthopyroxene or clinopyroxene oikocrysts (Fig. 4.10A) and is a texture found variably in the Reef but is especially prominent in the Reef pegmatoid nearer to the footwall contact (Fig. 4.10B). Examples of relict orthopyroxene grains in plagioclase (Fig. 4.10C) can be found which are seemingly limited to the Reef pegmatoid. Another texture which is more common in the pegmatoid is that of irregular, tricuspate-shaped relicts of plagioclase included in larger plagioclase grains (Fig.

4.10D) as well as in orthopyroxene grains. Triple-junction grain boundaries are also common between orthopyroxene and plagioclase grains usually occurring as opx-opx-opx or opx-plag-opx (rare) triple-junctions (Fig.4.10E). Phlogopite is generally found associated with base-metal sulphides (BMSs) which are usually developed around the irregular BMS grains or partly included within the BMS grain from orthopyroxene or plagioclase grain boundaries (Fig.4.10F).

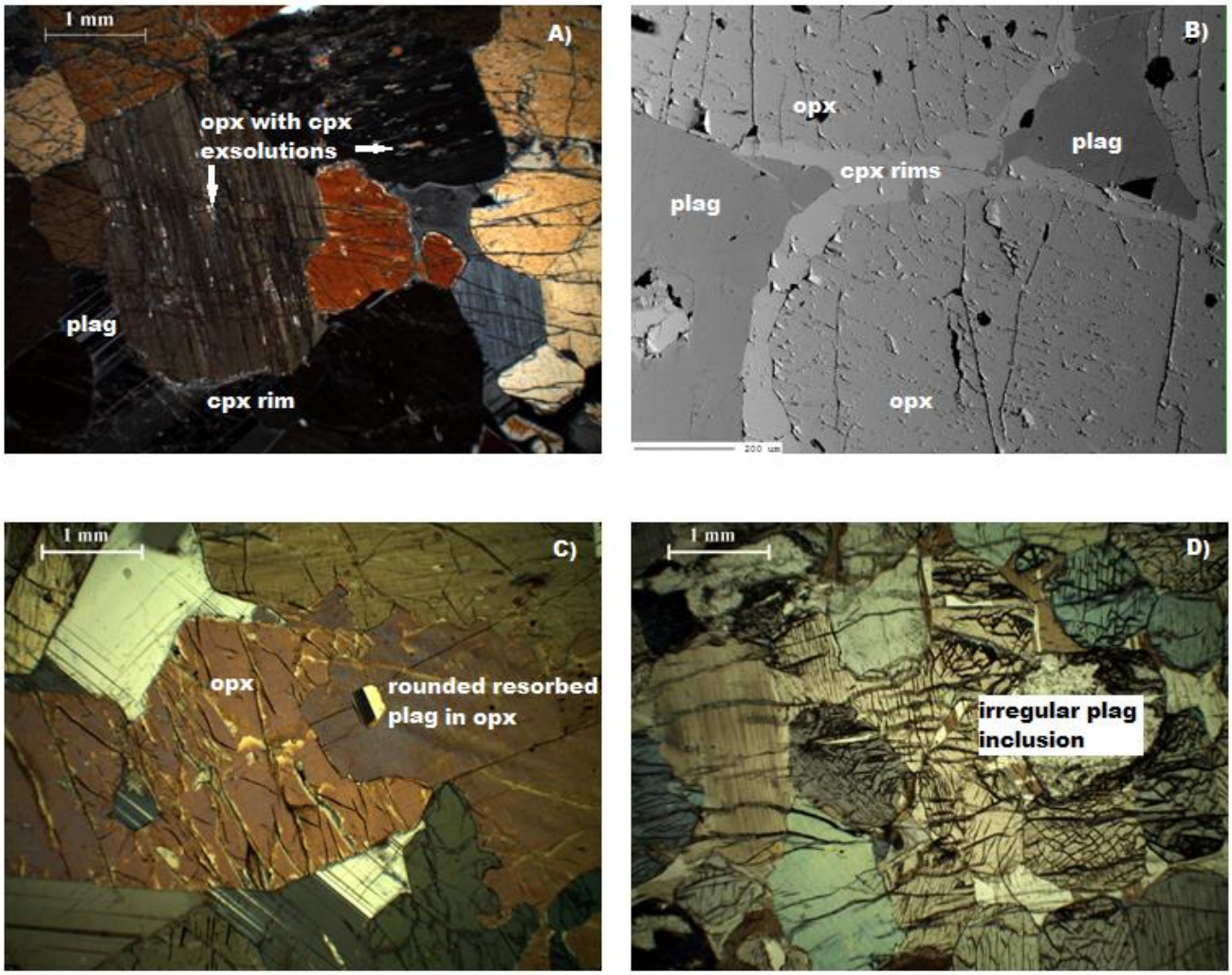

Figure 4.9 A) Photomicrograph of orthopyroxene grains with clinopyroxene exsolution lamellae and discontinuous rims in the Merensky Reef pyroxenite. Orthopyroxene triple-junctions are also clearly depicted. B) BSE image depicting discontinuous clinopyroxene rims on opx-opx grain boundaries in the Reef pyroxenite. C) Photomicrograph of rounded, resorbed relict plagioclase in orthopyroxene in the Merensky Reef pyroxenite. D) Photomicrograph of irregular relict plagioclase in orthopyroxene in the Reef pyroxenite.

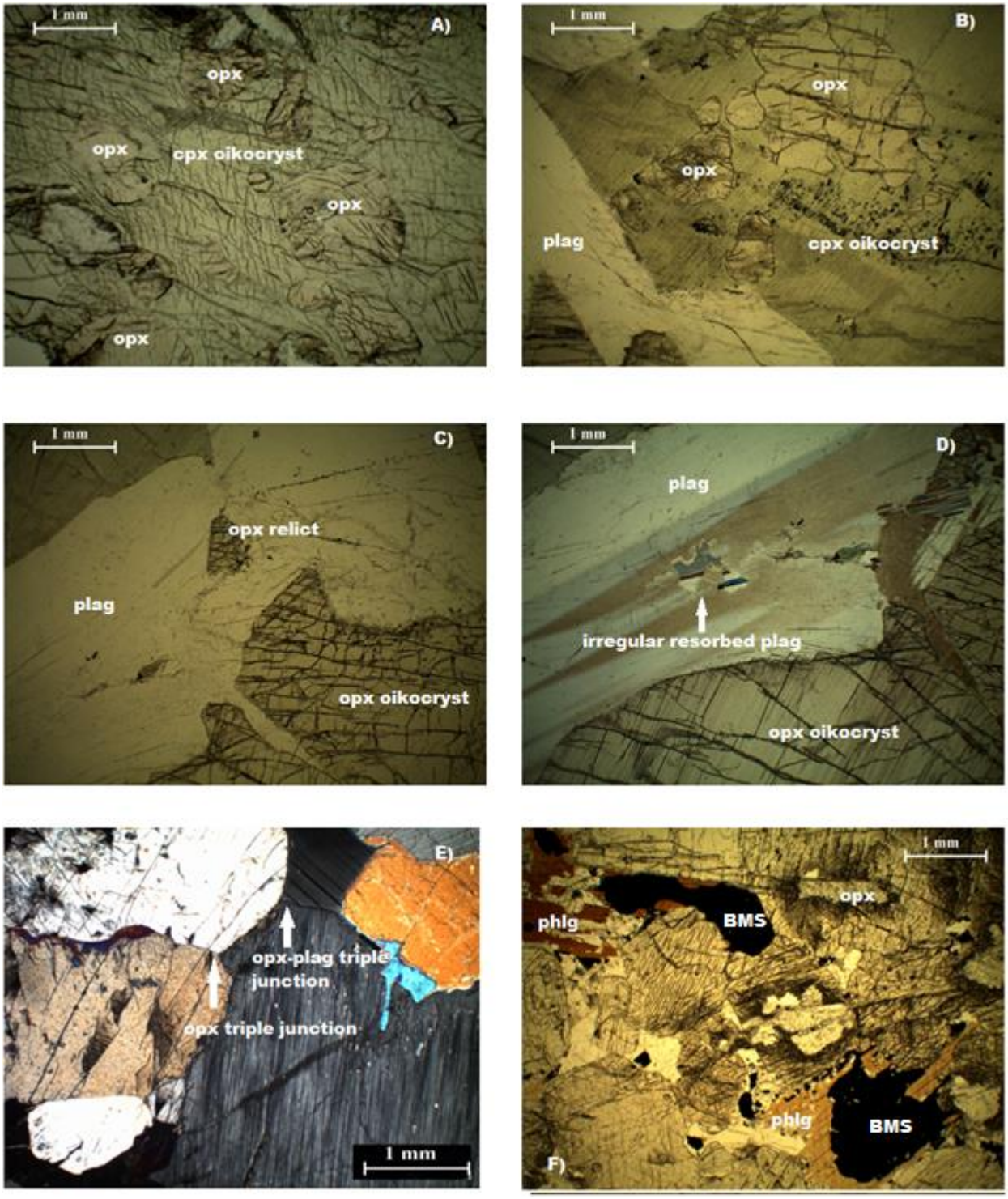

Figure 4.10 Photomicrographs illustrating A) rounded orthopyroxene grains included in large clinopyroxene oikocryst in the Reef pyroxenite and B) pegmatoidal pyroxenite. C) Relict orthopyroxene grain included in large plagioclase grain. D) Irregular shaped plagioclase grain included in larger plagioclase grain, possibly representing two generations of plagioclase crystallization. E) Orthopyroxene and plagioclase triple junctions in the Reef pyroxenite. F) Association of base-metal sulphides with phlogopite throughout the Reef.

4.2.1.3 Footwall

Many of the microtextures evident in the hanging wall and in the Reef are also present in the footwall rocks. The most common of these textures and probably the most common throughout the Merensky unit (in this sample suite) are the clinopyroxene exsolutions found in large orthopyroxene grains (Fig. 4.11 A). Another common texture is the discontinous clinopyroxene rims commonly found in association with orthopyroxene, especially those containing lamellae (Fig. 4.11 A). Evidence of oikocrystic clinopyroxene hosting orthopyroxene is also present with interstitial rims with preserved twinning (Fig. 4.11 B) where the clinopyroxene appears to be replacing the host orthopyroxene. The rims are not only confined to opx-opx grain boundaries but also occur at opx-plag grain boundaries. Resorbed plagioclase can be found as round inclusions in larger orthopyroxene grains (Fig. 4.12 A&B) especially within the footwall leuconorite, these inclusions are usually found in conjunction with clinopyroxene inclusions or exsolutions (Fig. 4.12 B). These plagioclase inclusions are not necessarily confined to large orthopyroxene grains as they occur in smaller orthopyroxenes as well (Fig. 4.12 C). It is notable that this texture is more prominent and common in the footwall leuconorite than in the hanging wall leuconorite. Perhaps the most interesting texture in the footwall, which is also confined to the footwall (in this sample suite), is that of the development of a coronitic texture around olivine (Fig. 4.12 D, E &F). Large olivine grains are surrounded by a corona of orthopyroxene which is in turn surrounded by a thin corona of some hydrous phase such as pargasite or clinozoisite (see section 5.2.4) before coming into contact with a plagioclase grain boundary (Fig. 4.12 D, E &F). In some cases the thin hydrous phase corona is

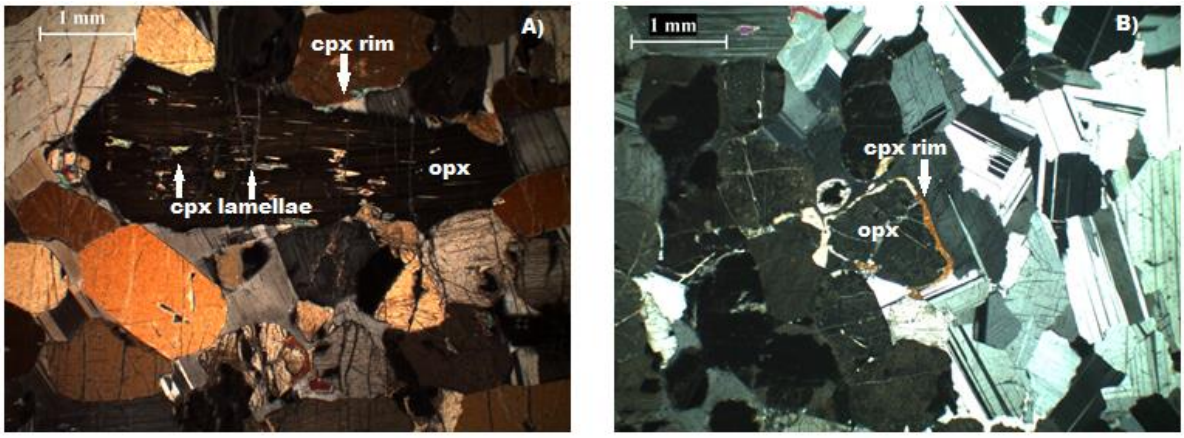

Figure 4.11 Photomicrographs of exsolution lamellae and discontinuous rims in the footwall unit rocks. A) Clinopyroxene exsolution lamellae and discontinuousrims on orthopyroxene. B) Clinopyroxene discontinuousrim on orthopyroxene displaying clinopyroxene twin-plane still intact as it almost completely surrounds the orthopyroxene.

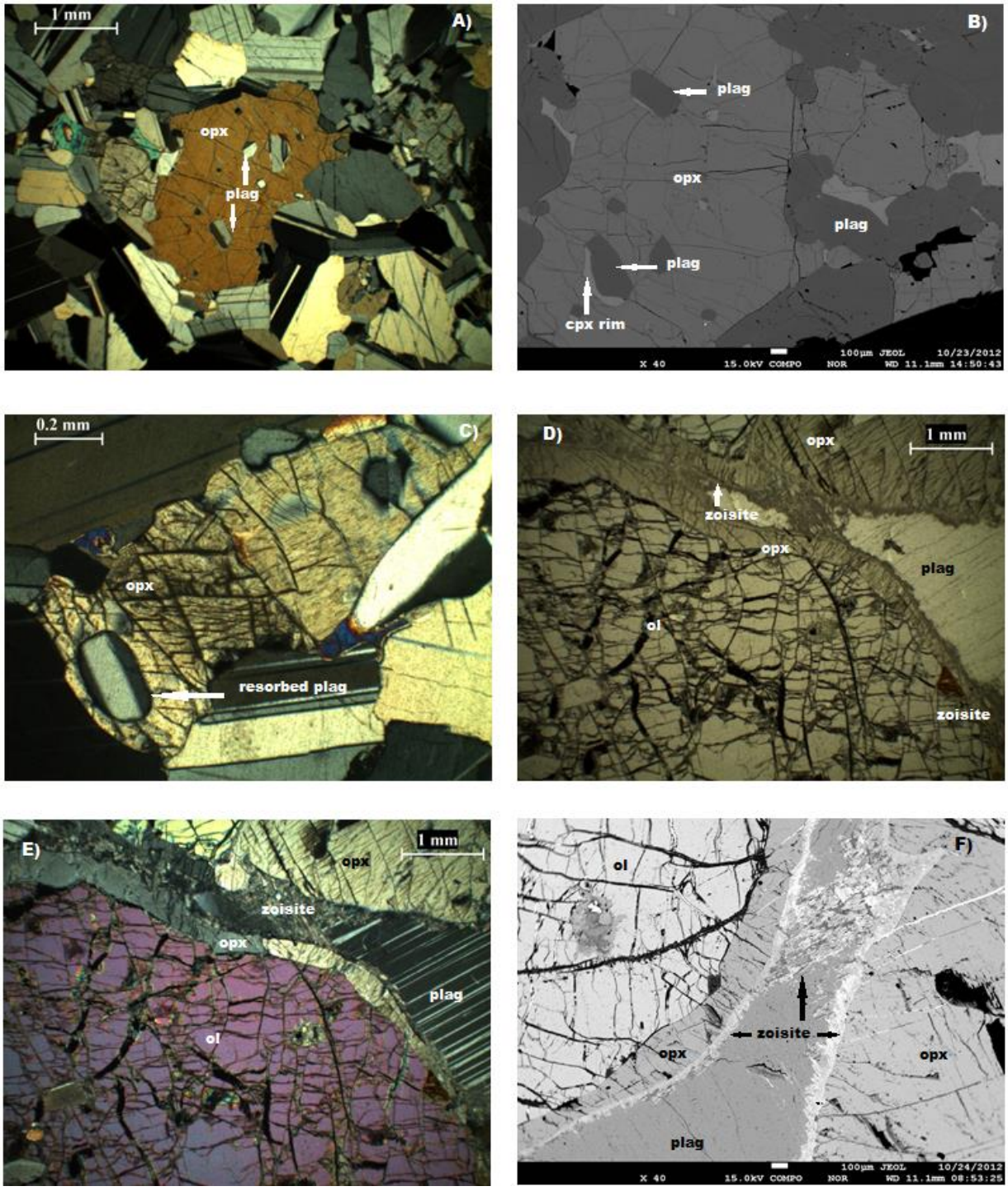

Figure 4.12 Photomicrographs and back-scatter electron images (BSE) illustrating various textures in rocks of the footwall unit. A) Resorbed plagioclase inclusions in orthopyroxene. B) BSE image of resorbed plagioclase with clinopyroxene rims in orthopyroxene. C) Resorbed plagioclase in small orthopyroxene grains. D) Coronitic texture where orthopyroxene and clinozoisite envelope olivine and vein-like plagioclase. E) Photomicrograph of corona texture with crossed polars. Note the preserved twin plane of the opx rim. F) BSE image of coronitic texture.

repeated at the boundary between the plagioclase and subsequent orthopyroxene grain boundary (Fig. 4.12 D, E &F). The plagioclase is vein-like and cross-cuts orthopyroxene (Fig. 4.12 D, E & F) and are associated with quartz and increased phlogopite content possibly having hydrothermal origins. The presence of olivine seems to be confined to the footwall leuconorite and carries examples where resorbed plagioclase is included in olivine (Fig.4.13 A). These olivine hosts are often serpentinized an irregular in shape bearing resemblance to interstitial phases (Fig 4.13 B). Although there are few examples, rounded, serpentinised olivine can also be found as inclusions in larger orthopyroxene grains (Fig. 4.13 C) in the footwall leuconorite.

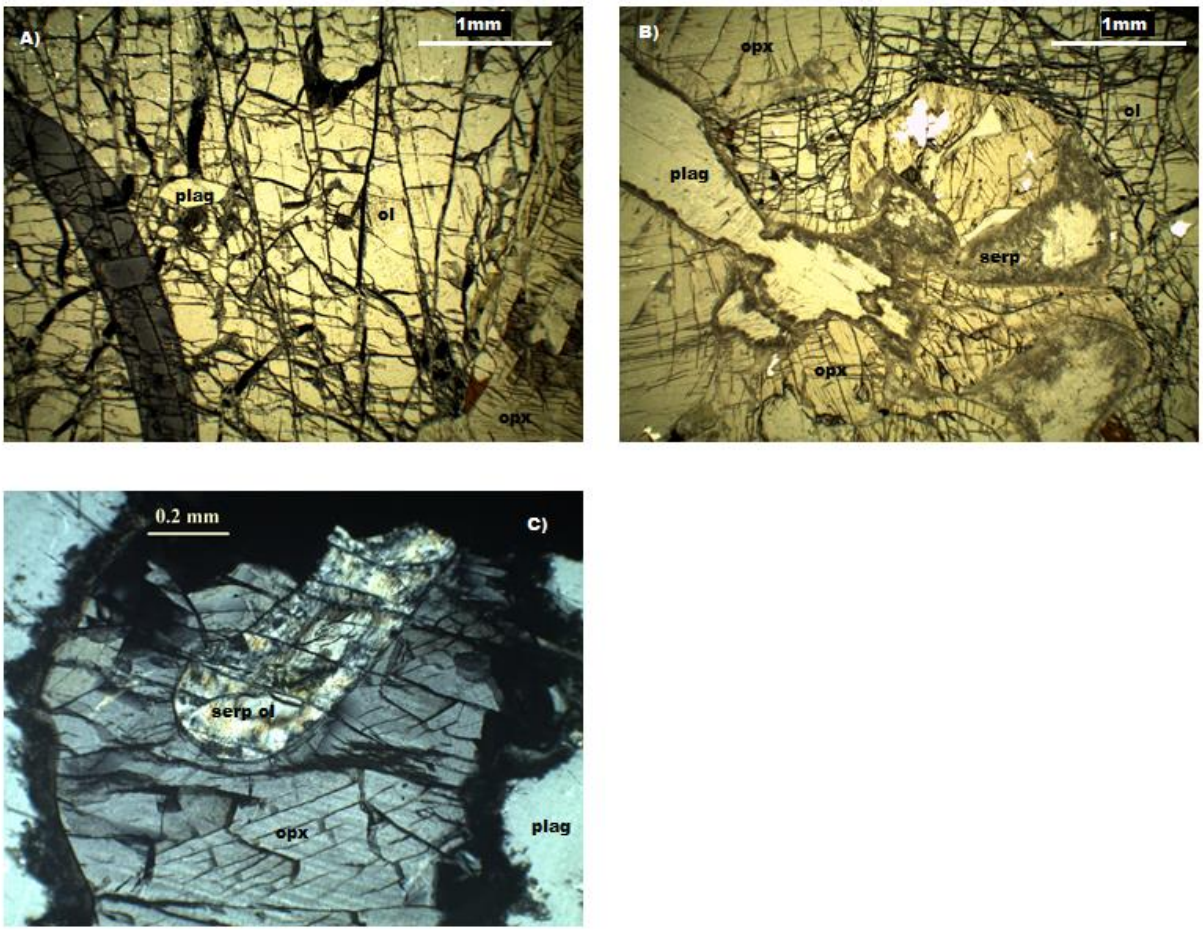

Figure 4.13 Photomicrographs illustrating resorbed plagioclase grains in olivine (A), irregular serpentinized olivine in association with plagioclase and orthopyroxene (B), and rounded, serpentinized olivine included in orthopyroxene (C) in the footwall leuconorite.

4.3 Summaries of Petrologic Observations

4.3.1 Orthopyroxene

Orthopyroxene mostly preserves its primary textures throughout the Merensky Cycle and occurs as an interstitial phase in the anorthosites and leuconorites of the Merensky hanging wall and footwall units. The existence of plagioclase chadocrysts and inclusions within larger orthopyroxene grains resulting in ophitic textures indicates that plagioclase had already crystallized prior to the crystallization of orthopyroxene. It therefore represents a post-cumulus phase in relation to plagioclase and most likely originated from the late crystallization of an orthopyroxene-saturated magma. Within the feldspathic pyroxenite and pegmatoidal pyroxenite, orthopyroxene comprises a majority of the rocks (over 80%) as a cumulus phase but can also be seen as a post-cumulus phase due the presence of irregular orthopyroxene relicts in plagioclase grains, a texture most prominent in the Reef pegmatoid. The triple-junctions present in the Reef are evidence that some recrystallization has taken place.

4.3.2 Clinopyroxene

Clinopyroxene occurs throughout the Merensky Cycle as an interstitial phase. It also occurs as large oikocrysts with inclusions of plagioclase and orthopyroxene which suggests it is post-cumulus and was the last of the three minerals to crystallize. This is supported by the presence of clinopyroxene exsolutions and discontinuous rims on orthopyroxene which are present throughout the Merensky Cyclic Unit and could represent clinoproxene crystallization out of a trapped interstitial liquid due to their irregular shape and grain boundary relationships.

4.3.3 Plagioclase

Plagioclase generally retains its primary igneous textures, except where altered to sericite in the footwall by hydrothermal fluid interaction as mentioned earlier. The source of the hydrothermal fluid responsible for alteration is most likely the same fluid which resulted in the formation of the Reef pegmatoid. Cawthorn (1991a) suggested that this alteration was a result of the fluid from the permeable pegmatoid decending to the footwall leuconorites increasing element mobility in

plagioclase and olivine resulting in alteration to sericite and serpentine, respectively. Zonation of plagioclase is not particularly prominent in these samples, although it has been recorded in literature e.g. (Eales *et al.*, 1990). The implication of unzoned plagioclase is that it supports magma mixing processes and those zoned plagioclases are relicts of earlier crystalization processes. Further evidence for the early crystallization of plagioclase is the existence of plagioclase chadocrysts included in orthopyroxene as well as the irregular tricuspate plagioclase grains included in orthopyroxene and plagioclase, while the existence of deformed plagioclase is further evidence to the early appearance of plagioclase in the mineral assemblage.

4.3.4 Chromite

Chromite occurs as the cumulus phase in the upper and lower chromitite stringers in the Merensky Reef pyroxenite. They are also found as tiny, often isolated grains as a minor interstitial phase in the Reef pyroxenite and sometimes in the Reef pegmatoidal pyroxenite. Dispersed interstitial chromite is more common below the upper chromitite stringer, which indicates that they are most likely derived from the stringer and occur dispersed below as a result of density contrasts. Current models accounting for the presence of chromitite infer that it resulted from the influx of chromite-rich liquid to preexisting pyroxenites, rich in orthopyroxene (Cameron, 1982; Hulbert & von Gruenewaldt, 1985) or the accumulation of chromite as a result of crystal settling from a chromite-rich melt (Kruger & Marsh, 1985). The latter agrees with the presence of interstitial chromite dispersed below the upper chromitite stringer mentioned above. The interstitial phase in the stringer is plagioclase and there is no evidence of inclusions of plagioclase within chromite crystals in this study.

4.3.5 Olivine and reaction phases

Olivine is not particularly predominant throughout sample suite but can be found especially in the footwall leuconorite, occurring as inclusions in orthopyroxene which would suggest that their crystallization preceded that of orthopyroxene. There are also examples of plagioclase inclusions in olivine grains indicating plagioclase crystallization preceding olivine and subsequent orthopyroxene crystallization. The corona textures evident on olivine grains in the footwall leuconorite may be a

result of secondary alteration processes. This may imply that not all olivine grains necessarily crystallized prior to orthopyroxene crystallization. An alternate possibility for the formation of this texture is that plagioclase crystallized and then underwent subsequent secondary alteration in the form of saussuritization resulting in the thin rims at opx-plag grain boundaries. These textures, their mineral associations, compositions and possible genetic origins are discussed further in Chapter 5.

4.3.6 Phlogopite

Phlogopite occurs dispersed in the hanging wall, Reef and footwall but is more prominent in the Reef especially in the Reef pegmatoid. In the hanging wall and footwall units it usually occurs as subhedral isolated grains whereas it occurs almost exclusively associated with BMS's in the Reef. The presence of phlogopite provides further evidence for the interaction of a thermal metasomatic fluid.

4.3.7 Base-Metal Sulphides (BMS)

BMSs are variably distributed throughout the Reef and Reef pegmatoid and tend to accumulate nearer the upper chromitite stringer. Coarser BMS grains tend to occur in the pegmatoid and are most commonly associated with phlogopite inferring that metasomatic fluid transport may have had something to do with its distribution.

Chapter 5- Mineral Chemistry

5.1 Hangingwall

Plagioclase

Plagioclase compositional data from the hanging wall rocks are illustrated in Figure 5.1. Plagioclase from the entire hanging wall package shows a compositional variation of 13.4 mol % from $An_{64.9}$ to $An_{82.3}$ (avg. $An_{75.1}$). Plagioclase cores have a compositional variation of 13.4 mol % from $An_{64.90}$ to $An_{78.3}$ (avg. $An_{73.3}$), rims have a compositional variation of 12.0 mol % from $An_{69.4}$ to $An_{81.4}$ (avg. $An_{76.7}$), and plagioclase inclusions have a compositional variation of 5.0 mol % from $An_{77.3}$to $An_{82.3}$ (avg. $An_{79.8}$).

The plagioclase compositional variation in the hanging wall anorthosite is 9.8 mol % from $An_{72.4}$ to $An_{82.3}$ (avg. $An_{76.9}$), while the plagioclase compositional variation in the hanging wall leuconorite is 16.9 mol % from $An_{64.9}$ to $An_{81.8}$ (avg. $An_{73.6}$). Average core compositions in the anorthosite and leuconorite are $An_{75.9}$ and $An_{71.6}$ respectively, while average rim compositions in the anorthosite and leuconorite are $An_{77.5}$ and $An_{75.8}$ respectively.

Orthopyroxene

Orthopyroxene in the hanging wall package is primarily enstatite with some anamalous pigeonite (Fig. 5.2) with an average composition of $En_{75}Fs_{22}Wo_{03}$ and has Mg# values which range between 74.6 and 82.9 (avg. 77.4). The Mg # values in the hanging wall anorthosite range between 75.9 and 82.9 (avg. 78.0) while, those in the hanging wall leuconorite range between 74.6 and 80.3 (avg. 77.2).

Clinopyroxene

Clinopyroxene in the hanging wall package are primarily diopsidic to augitic (Fig. 5.2) with an average composition of $En_{46}Fs_{10}Wo_{44}$ and has Mg# values which range between 77.0 and 88.6 (avg. 83.1). The Mg # values in the hanging wall anorthosite range between 77.0 and 88.6 (avg. 81.9) while, those in the hanging wall leuconorite range between 81.4 and 86.2 (avg. 83.9).

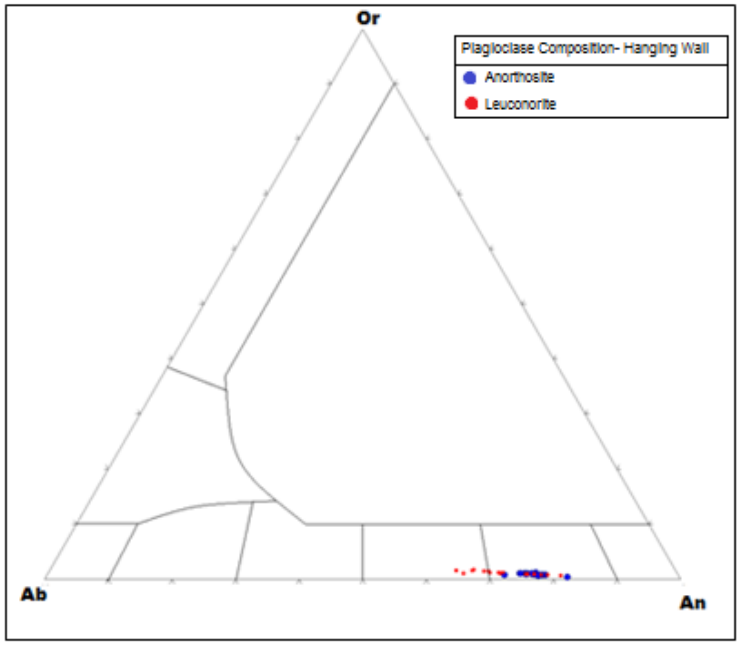

Figure 5.1 Plagioclase compositions in anorthosite and leuconorite of the hanging wall.

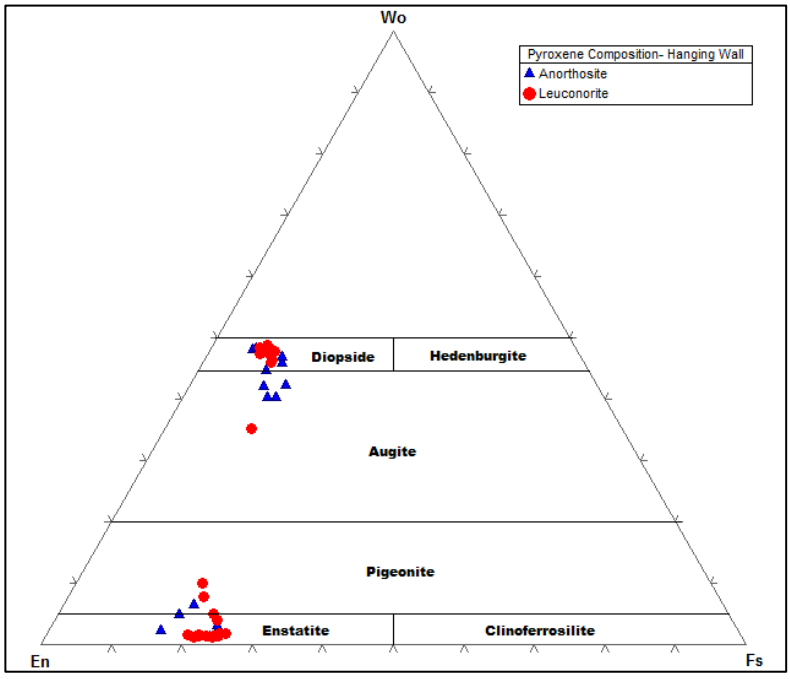

Figure 5.2 Compositions of all analyzed orthopyroxene and clinopyroxene in anorthosite and leuconorite of the hanging wall.

5.2 Merensky Reef

Plagioclase

Plagioclase compositional data from the Merensky Reef rocks are illustrated in Figure 5.3. Plagioclase in the Merensky Reef shows a compositional variation of 14.1 mol % from $An_{56.8}$ to $An_{70.8}$ (avg. $An_{62.7}$). Plagioclase cores have a compositional variation of 13.5 mol % from $An_{57.3}$ to $An_{70.8}$ (avg. $An_{62.9}$), rims have a compositional variation of 12.4 mol % from $An_{56.8}$to $An_{69.1}$ (avg. $An_{62.5}$), and plagioclase inclusions have a compositional variation of 4.6 mol % from $An_{61.4}$ to $An_{66.0}$ (avg. $An_{64.0}$).

The plagioclase compositional variation in the Merensky Reef feldspathic orthopyroxenite is 14.3 mol % from $An_{56.1}$to $An_{70.4}$ (avg. $An_{62.6}$), while the plagioclase compositional variation in the pegmatoidal feldspathic orthopyroxenite is 13.6 mol % from $An_{57.2}$ to $An_{70.8}$ (avg. $An_{63.0}$). Average core compositions in the pyroxenite and pegmatoid are $An_{62.5}$and $An_{63.4}$ respectively, while average rim compositions in the pyroxenite and pegmatoid are $An_{62.6}$ and $An_{62.4}$ respectively.

Orthopyroxene

Orthopyroxene in the Merensky Reef is primarily enstatite to pigeonite (Fig. 5.4) with an average composition of $En_{78}Fs_{19}Wo_{03}$ and has Mg# values which range between 78.5 and 87.1 (avg. 81.3). The Mg # values in the Merensky Reef feldspathic orthopyroxenite range between 78.5 and 87.0 (avg. 81.1) while, those in the Merensky Reef pegmatoidal orthopyroxenite range between 79.4 and 87.1 (avg. 81.8).

Clinopyroxene

Clinopyroxene in the Merensky Reef is primarily augite to diopside (Fig. 5.4) with an average composition of $En_{46}Fs_{08}Wo_{46}$ and has Mg# values which range between 79.0 and 89.2 (avg. 84.6). The Mg # values in the Merensky Reef feldspathic orthopyroxenite range between 80.5 and 88.2 (avg. 84.9) while, those in the Merensky Reef pegmatoidal orthopyroxenite range between 79.0 and 86.8 (avg. 83.4).

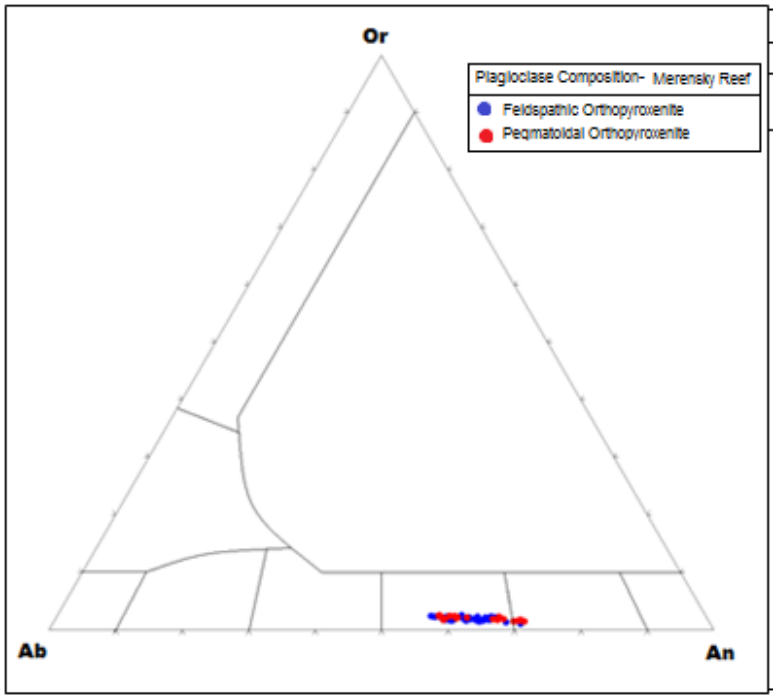

Figure 5.3 Plagioclase compositions in feldspathic orthopyroxenite and pegmatoidal feldspathic pyroxenite of the Merensky Reef.

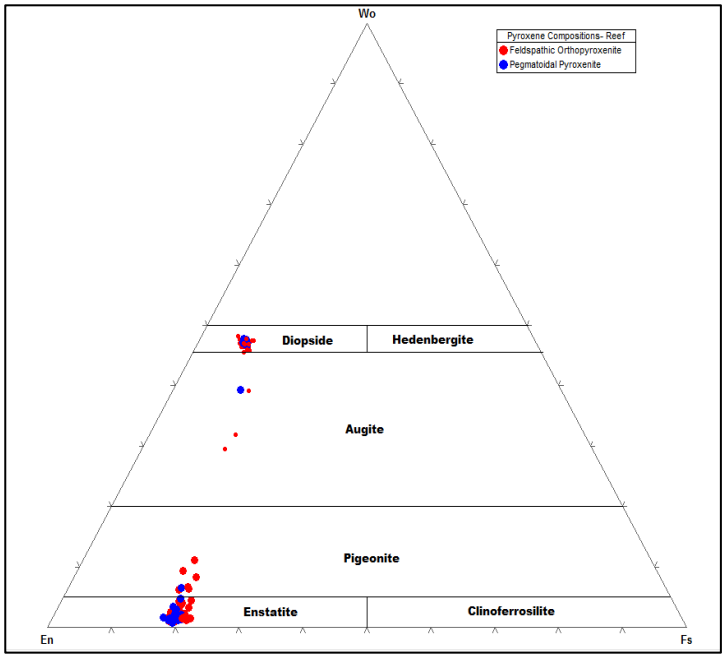

Figure 5.4 Compositions of all analyzed orthopyroxene and clinopyroxene in feldspathic orthopyroxenite and pegmatoidal feldspathic pyroxenite of the Merensky Reef.

5.3 Footwall

Plagioclase

Plagioclase compositional data from the footwall rocks are illustrated in Figure 5.5. Plagioclase from the footwall shows a compositional variation of 32.1 mol % from $An_{54.2}$ to $An_{86.3}$ (avg. $An_{73.2}$). Plagioclase cores have a compositional variation of 23.5 mol % from $An_{54.2}$ to $An_{77.7}$ (avg. $An_{71.5}$), rims have a compositional variation of 24.1 mol % from $An_{62.0}$ to $An_{86.0}$ (avg. $An_{76.3}$), and plagioclase inclusions have a compositional variation of 12.4 mol % from $An_{73.9}$to $An_{86.3}$ (avg. $An_{77.3}$).

The plagioclase compositional variation in the footwall leuconorite is 30.0 mol % from $An_{56.3}$ to $An_{86.3}$ (avg. $An_{72.5}$), while the plagioclase compositional variation in the footwall anorthosite is 31.8 mol % from $An_{54.2}$ to $An_{86.0}$ (avg. $An_{73.8}$). Average core compositions in the leuconorite and anorthosite are $An_{71.4}$ and $An_{71.5}$ respectively, while average rim compositions in the leuconorite and anorthosite are $An_{79.7}$ and $An_{75.1}$ respectively.

Orthopyroxene

Orthopyroxene in the footwall package is primarily enstatite to pigeonite (Fig. 5.6) with an average composition of $En_{79}Fs_{18}Wo_{03}$ has Mg# values which range between 77.9 and 84.1 (avg. 81.3). The Mg # values in the footwall leuconorite range between 80.7 and 82.8 (avg. 81.9) while, those in the footwall anorthosite range between 77.9 and 84.1 (avg. 81.8).

Clinopyroxene

Clinopyroxene in the footwall package is primarily diopside to augite (Fig. 5.6) with an average composition of $En_{46}Fs_{07}Wo_{47}$ and has Mg# values which range between 83.6 and 90.5 (avg. 87.7). The Mg # values in the footwall leuconorite range between 83.6 and 89.1 (avg. 87.6) while, those in the footwall anorthosite range between 86.1 and 90.5 (avg. 81.8).

Olivine and reaction phases

Olivine and reaction phases such as clinozoisite are present in the footwall leuconorite. Their compositions are presented in Table 5.1 below. Olivine Mg# values are uniform ranging between Mg# 83-84 with an average of 83. The mean olivine composition is $Fo_{83}Fa_{17}$ which plots as Chrysolite. Clinozoisite has an Al_2O_3 content range of 33.0-36.8 (ave. 35.2) wt% while SiO_2 and CaO content ranges between 38.7-41.7 (ave. 40.2) wt% and 21.2-24.0 (ave. 23.4) wt% respectively.

Table 5.1 Compositions of measured olivine and clinozoisite in the footwall leuconorite.

Olivine

Sample	MgO	SiO2	FeO	MnO	NiO	CaO	Total	Mg#
10-1-ol1	43.39	39.80	15.66	0.25	0.33	0.00	99.43	83
10-1-ol1	43.92	39.50	16.26	0.24	0.29	0.00	100.21	83
10-1-ol1	43.44	39.69	15.05	0.24	0.29	0.00	98.73	84
10-1-ol1	43.72	39.63	15.82	0.28	0.31	0.00	99.75	83
10-1-ol2	44.08	39.81	15.32	0.24	0.28	0.00	99.74	84
10-1-ol2	43.94	39.66	15.36	0.29	0.29	0.00	99.54	84
Average	**43.75**	**39.68**	**15.58**	**0.26**	**0.30**	**0.00**	**99.57**	**83**

Clinozoisite

Sample	Al2O3	CaO	K2O	SiO2	MgO	FeO	MnO	Cr2O3	TiO2	Na2O	Total
10-4-px2	36.82	23.59	0.03	40.05	0.03	0.91	0.06	0.01	0.00	0.04	101.53
10-4-px2	34.36	23.89	0.01	39.95	0.68	3.57	0.19	0.02	0.01	0.00	102.67
10-4-px2	35.63	22.84	0.02	41.72	0.01	1.39	0.06	0.00	0.01	0.07	101.77
10-4-px2	36.66	23.81	0.00	40.52	0.01	0.80	0.03	0.00	0.01	0.00	101.84
10-3b-px1	35.75	23.41	0.01	41.69	0.02	2.21	0.44	0.00	0.00	0.08	103.60
10-2-px1	34.95	23.59	0.03	41.03	0.00	2.26	0.10	0.02	0.03	0.00	101.99
10-2-px1	32.98	23.86	0.04	39.11	0.01	5.04	0.03	0.05	0.00	0.00	101.11
10-2-px1	34.79	21.21	0.02	38.93	1.75	3.46	0.12	0.01	0.00	0.01	100.29
10-2-px1	34.48	24.01	0.03	38.70	0.52	2.72	0.35	0.01	0.01	0.00	100.83
Average	**35.16**	**23.35**	**0.02**	**40.19**	**0.34**	**2.49**	**0.15**	**0.01**	**0.01**	**0.02**	**101.74**

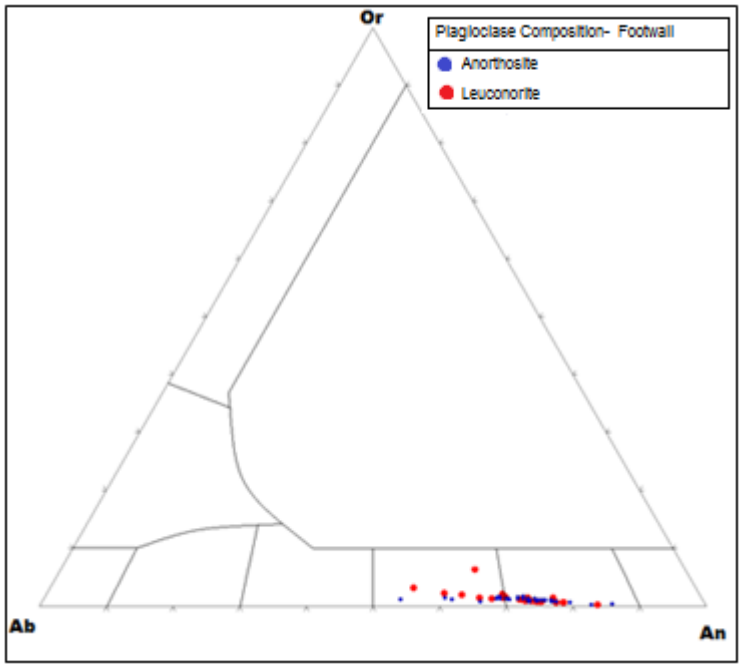

Figure 5.5 Plagioclase compositions in feldspathic orthopyroxenite and pegmatoidal feldspathic pyroxenite of the footwall.

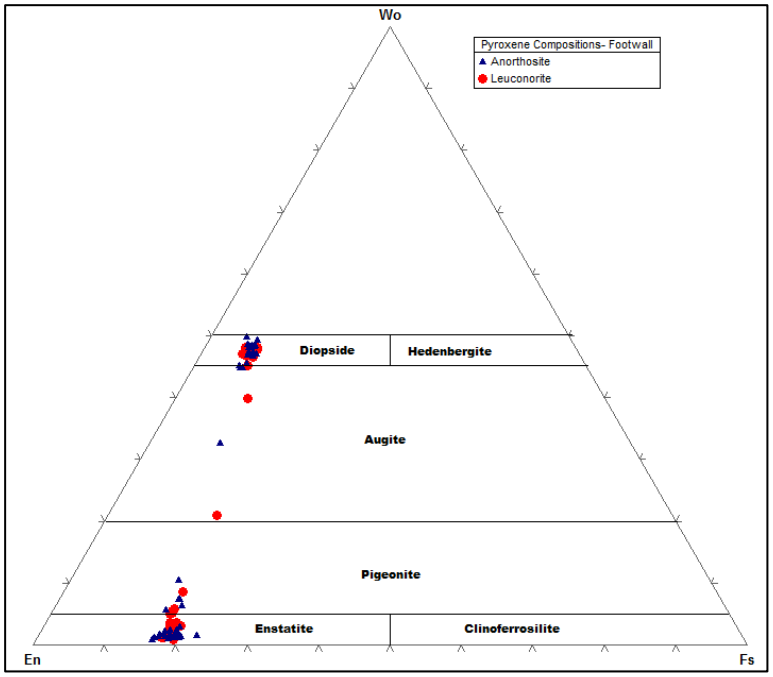

Figure 5.6 Compositions of all analyzed orthopyroxene and clinopyroxene in feldspathic orthopyroxenite and pegmatoidal feldspathic pyroxenite of the footwall.

5.4 Summary of Mineral Compositional Results

5.4.1 Orthopyroxene

Orthopyroxene compositions show little variation with depth throughout the Merensky sequence with only some slight variation in the hanging wall leuconorite which has Mg# values slightly lower than those found in other lithologies (Fig.5.8). Mean Mg# values in the hanging wall anorthosite (77.95) and leuconorite (77.20) are comparable albeit lower than the Mg# values in the corresponding footwall leuconorite (81.89) and anorthosite (81.66), which are also comparable. Mg# values in the Reef are more similar to the footwall rocks with Merensky orthopyroxenite (81.06) and pegmatoidal orthopyroxenite (81.79) also showing comparable values. The mean Mg# value for all analysed samples is 81.0 (Table 5.2) and the Mg# compositional range in the samples generally show very little variation.

Table 5.2 Mean compositions of measured clinopyroxene and orthopyroxene by type.

	Mg # AVE	**Standard Deviation *2**
All Clinopyroxene	86.0	5.1
Oikocrysts	82.2	5.8
Exsolutions	86.6	3.7
Inclusions	87.0	3.8
Discontinuous Rims	86.8	3.0
Interstial Liquid	88.3	1.3
All Orthopyroxene	81.0	4.8

5.4.2 Plagioclase

The full compositional range of plagioclase in the sample suite is illustrated in Figure 5.7. The mean plagioclase compositions in the hanging wall anorthosite ($An_{76.90}$) and leuconorite ($An_{73.56}$) are comparable, with only a marginally higher An content in the anorthosite. The same can be said for the footwall leuconorite ($An_{72.52}$) and anorthosite ($An_{73.84}$). Very little difference is seen in the mean compositions between corresponding rock types, although the hanging wall anorthosite has a slightly higher An content than the footwall anorthosite. Mean An composition in plagioclase of the Reef are comparable between the Merensky pyroxenite ($An_{62.55}$) and Merensky pegmatoidal pyroxenite ($An_{63.05}$). As illustrated in Figure 5.8 the mean compositions of plagioclase in the hanging wall are relatively uniform in the anorthosite before gradually decreasing with depth in the leuconorite and reaching a minimum in the Merensky Reef. From this point a gradual increase in plagioclase An content occurs in the leuconorites through to the anorthosites with increasing depth.

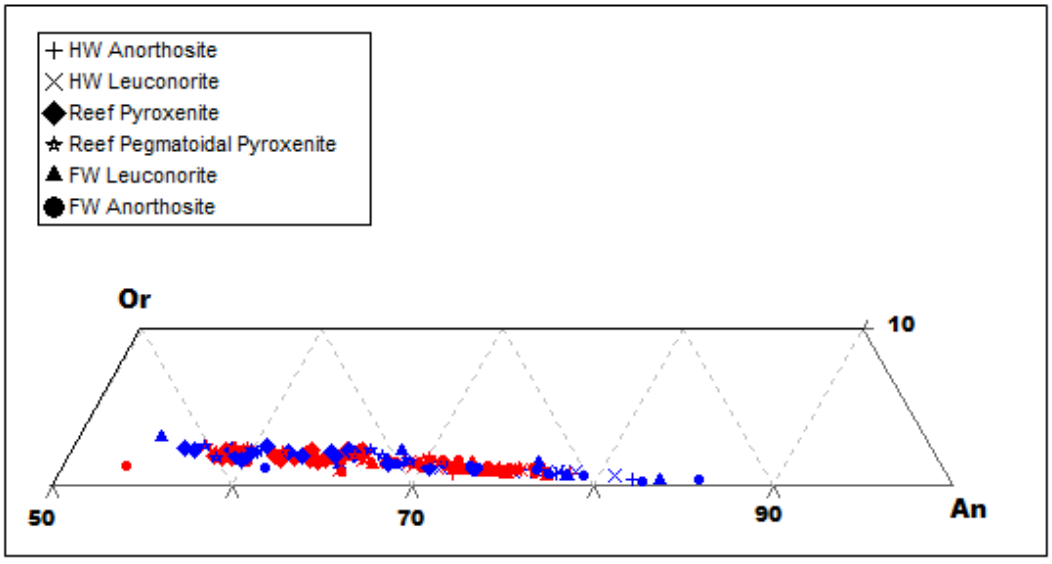

Figure 5.7 Compositions of all analyzed plagioclase in all lithologies of the Merensky Reef unit. Red symbols correspond to core compositions of that rock type's symbol, while blue symbols correspond to rim compositions of that rock type's symbol.

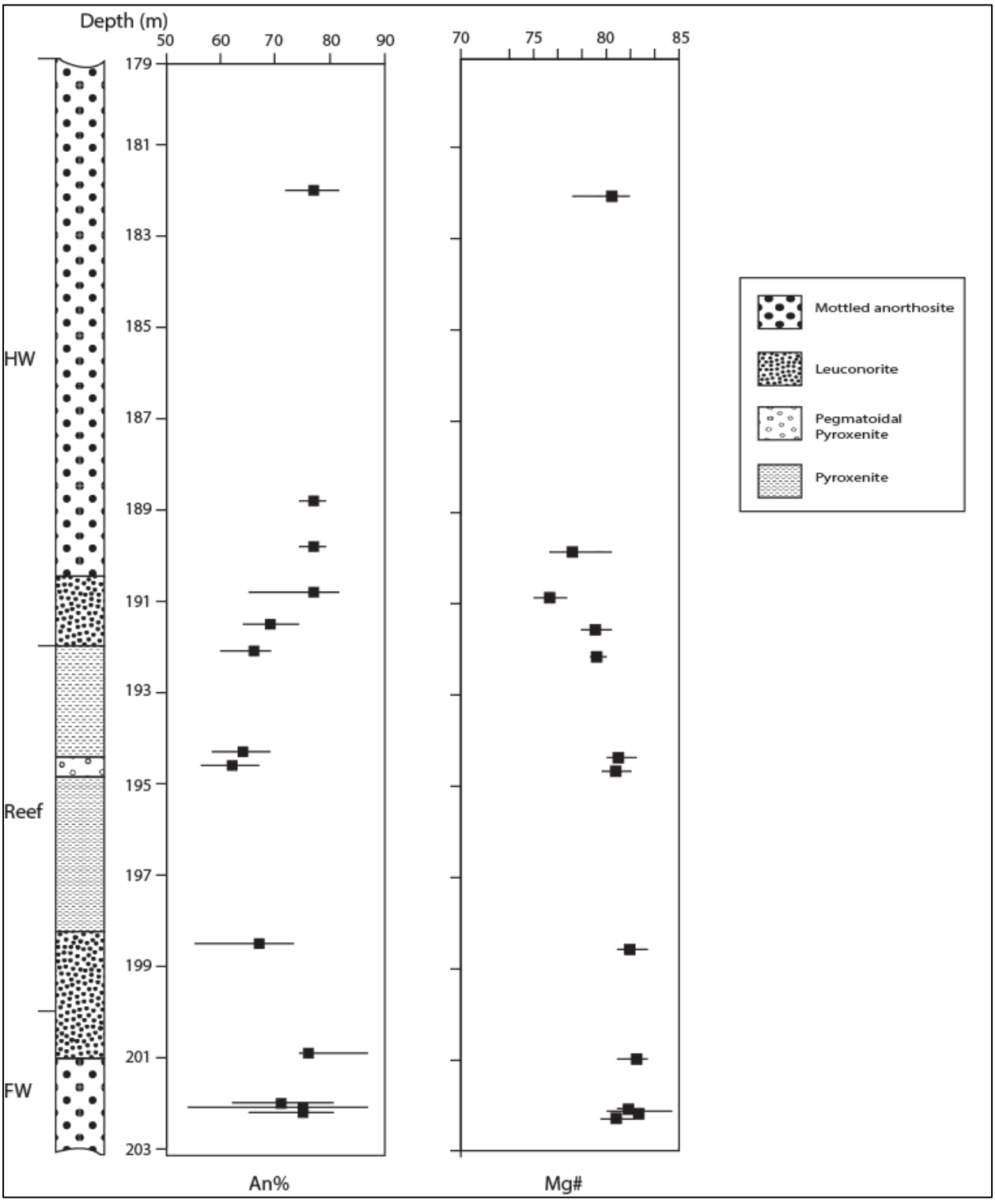

Figure 5.8 Mean values and compositional ranges of plagioclase and orthopyroxene expressed as % An and Mg# respectively, as a function of stratigraphic height.

5.4.3 Clinopyroxene

Mean compositions of all clinopyroxene throughout the Merensky unit show little variation with depth with the exception of lower Mg# values in the hanging wall leuconorite. These lower values correspond to the lower Mg# values seen in orthopyroxenes of the hangingwall leuconorite. Clinopyroxene occurs throughout the whole sequence as oikocrysts, exsolutions in orthopyroxene, inclusions in orthopyroxene, reaction rims with orthopyroxene, and as an interstitial liquid. All analyzed clinopyroxenes combined yield an average Mg# value of 86.0, oikocrysts have an average Mg# value of 82.2; exsolutions have an average Mg# value of 86.6; inclusions have an average Mg# value of 87.0; reaction rims have an average Mg# value of 86.8; and interstitial liquid has an average Mg# value of 88.3. The Mg# values of exsolutions, inclusions and discontinuous rims are within range of the average of all clinopyroxene, while clinopyroxene interstitial liquid is slightly above and clinopyroxene oikocrysts are significantly below average Mg# values (Table 5.2). The Mg# values of the oikocrysts are a lot closer in range to the Mg# values of orthopyroxenes than clinopyroxenes (Table 5.2). This could indicate that the oikocrysts are more evolved than the other observed textures of clinopyroxene possibly representing the final stage of crystallization from a clinopyroxene-saturated magma. This would allow for the oikocrysts to incorporate all other phases as xenocrysts.

5.4.4 Olivine and reaction phases

As mentioned in Chapter 4, there is an odd association of olivine with plagioclase, orthopyroxene and another phase identified as clinozoisite (Table 5.1). Unfortunately this association is limited to one sample in the footwall leuconorite where few olivine grains are rimmed by orthopyroxene which shares a grain boundary with plagioclase (Fig. 4.9 D, E & F). Alteration has taken place at this grain boundary and is repeated on the adjacent opx-plag grain boundary to form clinozoisite on each boundary. Upon closer inspection the plagioclase looks to be cross-cutting a larger orthopyroxene grain and might then represent the presence of a magmatic fluid as the texture is somewhat vein-like. The clinozoisite could then be an alteration product of plagioclase produced by saussuritization. The rim of orthopyroxene around olivine would then represent primary magmatic crystallization of orthopyroxene and olivine which shares a grain boundary before the orthopyroxene is cross-cut by a plagioclase vein. Evidence for hydrothermal fluid interaction is seen in vein-like textures composed

of plagioclase and quartz which cross-cut pre-existing crystals. The texture was initially speculated to be a 'corona' texture, with olivine reacting with plagioclase to form a corona of orthopyroxene and a symplectite-like hydrous phase, in this case clinozoisite. There are superficial problems with this association, such as that the paired reaction is not obviously continuous along the olivine-plagioclase contact, and that the symplectite would then be expected to have a comparable or greater thickness than the equilavent orthopyroxene. This is not the case here, as the orthopyroxene is far thicker than the clinozoisite which is extraordinarily thin compared to the classic 'coronitic gabbro' textures expected to result from this kind of reaction.

Chapter 6- Isotope Chemistry

6.1 Whole Rock Sm-Nd data

Whole rock Sm-Nd isotopic compositions are presented in (Table 6.1) and plotted on a $^{147}Sm/^{144}Nd$ vs. $^{143}Nd/^{144}Nd$ isotopic compositional plot (Fig. 6.1). ε_{Nd} values are plotted against stratigraphic height (Fig. 6.2). Whole rock Sm-Nd isotopic data are discussed for each unit as follows:

6.1.1 Footwall

Whole rock isotopic $^{147}Sm/^{144}Nd$ and $^{143}Nd/^{144}Nd$ ratios in the footwall show a large degree of variation. These data also show variation from unit to unit which is dependent on the plagioclase proportion which is LREE-enriched as opposed to pyroxene which is HREE-enriched. Plagioclase is therefore expected to have lower $^{147}Sm/^{144}Nd$ ratios in relation to pyroxene. Whole rock isotope samples in the footwall are scattered between two 2.06 Ga reference lines with initial ε_{Nd} values of -4.7 and -7.3 (Fig. 6.1). These data correspond to ε_{Nd} values between $\varepsilon_{Nd\ (2.06\ Ga)}$ = -4.5 to -6.3 ±0.7. The only measured anorthosite has an ε_{Nd} value of $\varepsilon_{Nd(2.06\ Ga)}$ = -5.6 ±0.7, while leuconorite has ε_{Nd} values which range between $\varepsilon_{Nd\ (2.06\ Ga)}$ = -4.5 to -6.3 ±0.7 and do not show any contamination trend (Fig. 6.2).

6.1.2 Merensky Reef

Whole rock isotopic $^{147}Sm/^{144}Nd$ and $^{143}Nd/^{144}Nd$ ratios in the Reef show slight variation with ratios that are generally greater than those found in the footwall and hanging wall units. The whole rock reef samples plot scattered between the two 2.06 Ga reference lines with most of the samples falling on or around the on the 2.06 Ga reference line with an initial ε_{Nd} value = -7.3 (Fig. 6.1). These data correspond to ε_{Nd} values ranging between $\varepsilon_{Nd\ (2.06\ Ga)}$ = -6.3 to -8.5 ±0.6. There is no variation between the "normal" pyroxenite and the pegmatoidal pyroxenite as the pegmatoid falls in the range of the "normal" pyroxenite with a value of $\varepsilon_{Nd\ (2.06\ Ga)}$ = -6.5 ±0.6. ε_{Nd} values in the reef show a trend

which becomes increasingly more radiogenic from the base of the pyroxenite upwards, reaching a peak in the pegmatoid, and then decreasing again upwards (Fig. 6.2).

6.1.3 Hanging Wall

Whole rock isotopic $^{147}Sm/^{144}Nd$ and $^{143}Nd/^{144}Nd$ ratios in the hanging wall show little or no significant variation with similar ratios to samples in the footwall. Samples H2 and H5 are colinear and plot on the 2.06 Ga reference line with an initial ε_{Nd} value = -4.7 while the other hanging wall samples are scattered between the two reference lines (Fig. 6.1). These data correspond to initial ε_{Nd} values ranging between $\varepsilon_{Nd\ (2.06\ Ga)}$ = -4.8 to -6.4 ±0.7. Anorthosite has ε_{Nd} values which range between $\varepsilon_{Nd\ (2.06\ Ga)}$ = -4.8 to -5.4 ±0.7, while leuconorite has ε_{Nd} values which range between $\varepsilon_{Nd\ (2.06\ Ga)}$ = -5.3 to -6.4 ±0.7. ε_{Nd} values in the hanging wall progressively become less radiogenic with distance upwards, away from the mineralized reef (Fig. 6.2).

The transition between units based on ε_{Nd} values is not easy to constrain due to the variable nature of the values presented in each unit, especially in the footwall where there is a slight increase in values upwards with two anomalously high and low ε_{Nd} values. Unfortunately a sample was not available for the footwall near the reef contact and it is thus impossible to determine the exact nature of the contact. We can however, infer that there would be a reasonably sharp contact between the footwall leuconorite and footwall pyroxenite as this is what is seen at the reef/hanging wall contact. At this contact the ε_{Nd} values gradually increase from the reef pyroxenite to the hanging wall leuconorite (possibly due its proximity to the reef contact) before sharply increasing in the leuconorite proper. The transition from leuconorite is gradational with a gradual increase in ε_{Nd} values upwards.

6.2 Mineral Separate Sm-Nd data

Mineral separate Sm-Nd isotopic compositions are presented in (Table 6.2) and plotted on a $^{147}Sm/^{144}Nd$ vs. $^{143}Nd/^{144}Nd$ isotopic compositional plot (Fig. 6.1). Mineral separate Sm-Nd isotopic data are discussed by mineral as follows:

6.2.1 Plagioclase

Plagioclase Sm-Nd isotopic ratios in the hanging wall are $^{147}Sm/^{144}Nd$ = 0.0936 and $^{147}Sm/^{144}Nd$ = 0.0791 in the anorthosite and leuconorite respectively. Plagioclase Sm-Nd isotopic ratios in the Merensky Reef are $^{147}Sm/^{144}Nd$ = 0.0964 and $^{147}Sm/^{144}Nd$ = 0.0670 in the pyroxenites, while ratios in the footwall leuconorite and anorthosite are $^{147}Sm/^{144}Nd$ = 0.0893 and $^{147}Sm/^{144}Nd$ = 0.0891 respectively. Plagioclase samples are colinear and plot on a 2.06 Ga aged reference isochron with an initial ε_{Nd} value of -7.3±1.1 (Fig. 6.1). ε_{Nd} values in plagioclase are generally uniform and range between $\varepsilon_{Nd\ (2.06\ Ga)}$ = -5.8 to -7.8±1.1 (averaging ε_{Nd}= -7.0). Although there is no obvious trend of decreasing crustal contamination with increasing height, plagioclase ε_{Nd} values are however, generally more contaminated than their corresponding mean whole rock ε_{Nd} values. Plagioclase (ε_{Nd}= -7.0 and -5.8±1.1) is less contaminated than coexisting orthopyroxene (ε_{Nd}= -9.1 and -11.6±1.1) in the hanging wall and footwall samples but plagioclase samples (ε_{Nd}= -7.3±1.1) are slightly more contaminated than coexisting orthopyroxene (ε_{Nd}= -7.1±1.1) in the Reef (Fig. 6.3).

6.2.2 Orthopyroxene

Orthopyroxene separates were only obtained from leuconorites and pyroxenites. The orthopyroxene Sm-Nd isotopic ratio in the hanging wall leuconorite is $^{147}Sm/^{144}Nd$ = 0.2330. Orthopyroxene $^{147}Sm/^{144}Nd$ isotopic ratios in the Merensky Reef are $^{147}Sm/^{144}Nd$ = 0.1333 and $^{147}Sm/^{144}Nd$ = 0.1930 in the pyroxenites, while the ratio in the footwall leuconorite is $^{147}Sm/^{144}Nd$ = 0.2474. Orthopyroxenes from the reef plot on a 2.06 Ga reference line with an initial ε_{Nd} value of -7.3±1.1, whereas the samples from the footwall and hanging wall plot slightly below this reference line (Fig. 6.1). ε_{Nd} values in orthopyroxene show some variation between the leuconorites and pyroxenites, with the leuconorites in the hanging wall and footwall having ε_{Nd} values of -9.1 and -11.6±1.1 respectively, while ε_{Nd} values in the Reef pyroxenite are both ε_{Nd}= -7.1±1.1. The mean ε_{Nd} value of all orthopyroxenes is -8.7 which is more contaminated than the corresponding whole rock values. ε_{Nd} values in orthopyroxenes are within range of their whole rock counterparts, while ε_{Nd} values in orthopyroxenes of the leuconorites are significantly more contaminated than their whole rock counterparts. An elemental budget problem exists in this case which is discussed in Chapter 7.2.

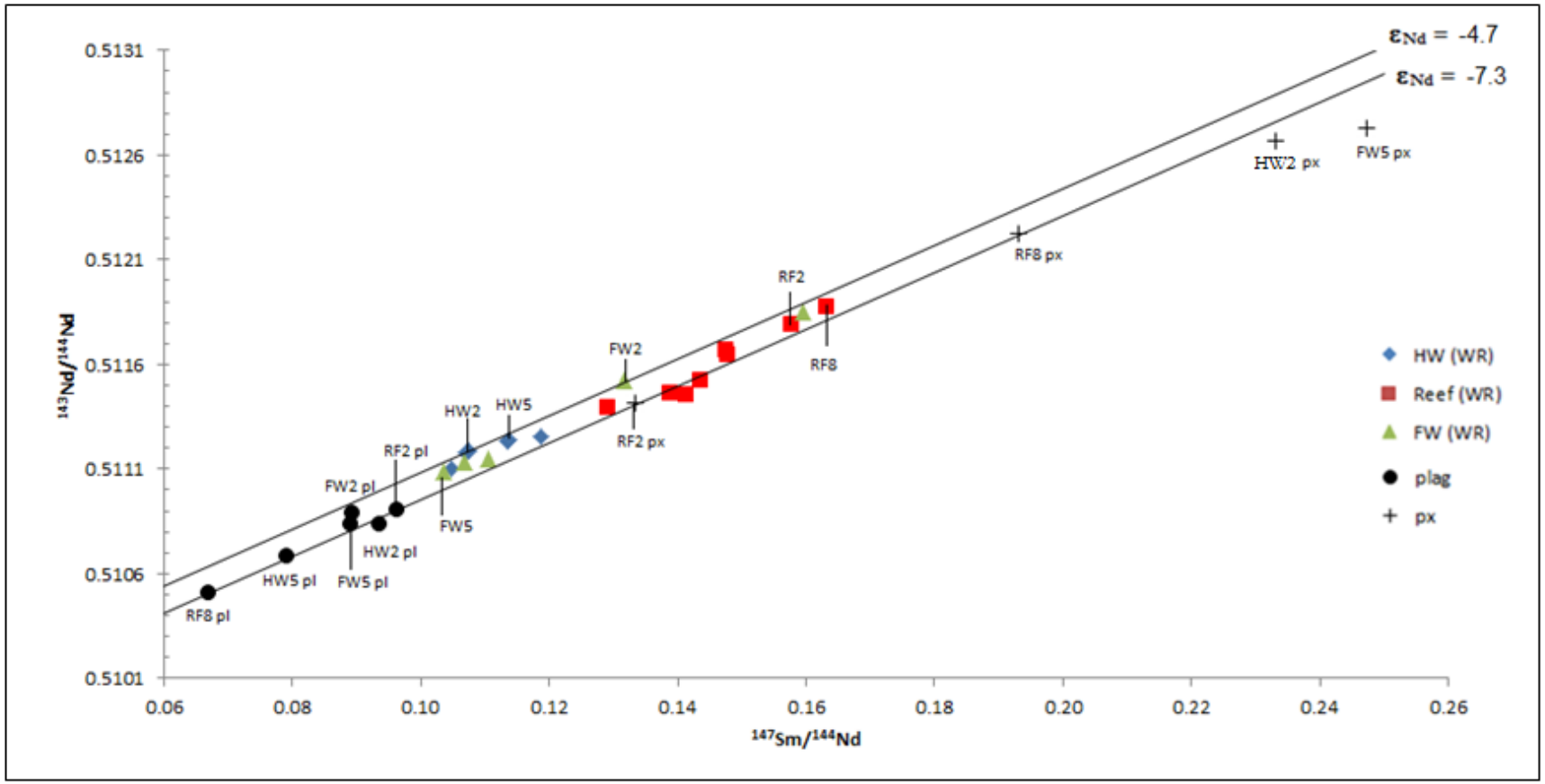

Figure 6.1 Whole rock and mineral separate Sm-Nd isotopic data from the Merensky Cyclic Unit at Winnaarshoek of the eastern Bushveld Complex, plotted against two 2.06 Ga reference isochrons. The top reference line is represented by the equation: y = 0.0136x + 0.50974 with an initial ε_{Nd} value corresponding to -4.7 while the bottom reference line is represented by the equation y = 0.0136x + 0.5096 corresponding to an initial ε_{Nd} value of -7.3. HW, RF and FW stand for hanging wall, Reef and footwall respectively and (WR) stands for whole rock. Labeled whole rock samples correspond to plagioclase and orthopyroxene separates.

Table 6.1 Sm-Nd whole rock and mineral separate isotope geochemistry for rocks of the Merensky Cyclic Units from Winnaarshoek in the eastern Bushveld Complex. * = duplicate samples.

Sample	Depth (m)	Rock Type/mineral	Nd (ppm)	Sm (ppm)	$^{147}Sm/^{144}Nd$	$Nd^{143}/Nd^{144}_{(2.060)}$	$(Nd^{143}/Nd^{144})m$	error2s	εNd(2.06)
Whole Rock									
H1	184.0	anothosite	2.51	0.45	0.1076	0.50973	0.51119	0.000023	-4.8
H2	187.5	anothosite	1.94	0.34	0.1069	0.50973	0.51118	0.000034	-4.8
H3	190.2	anothosite	1.65	0.31	0.1134	0.50970	0.51124	0.000018	-5.4
H4	190.8	leuconorite	1.58	0.27	0.1048	0.50968	0.51111	0.000029	-5.6
H5	191.5	leuconorite	1.40	0.26	0.1138	0.50970	0.51124	0.000020	-5.3
H6	192.0	leuconorite	1.38	0.27	0.1186	0.50965	0.51125	0.000023	-6.4
R1	192.1	pyroxenite	1.57	0.38	0.1478	0.50964	0.51164	0.000016	-6.5
R2	192.2	pyroxenite	3.07	0.80	0.1577	0.50965	0.51179	0.000014	-6.3
R3	192.4	pyroxenite	1.45	0.35	0.1477	0.50966	0.51167	0.000027	-6.0
R4	193.0	pyroxenite	4.58	1.09	0.1437	0.50957	0.51152	0.000019	-7.9
R5	193.6	pyroxenite	3.17	0.73	0.1388	0.50958	0.51146	0.000021	-7.7
R6	193.9	pyroxenite	4.91	1.15	0.1414	0.50953	0.51145	0.000015	-8.5
R6*	193.9	pyroxenite	0.87	0.20	0.1420	0.50959	0.51152	0.000016	-7.4
R7	194.3	peg pyroxenite	4.99	1.07	0.1292	0.50964	0.51139	0.000015	-6.5
R8	194.6	pyroxenite	2.71	0.73	0.1632	0.50966	0.51187	0.000016	-6.1
F1	198.5	leuco	1.93	0.51	0.1594	0.50969	0.51185	0.000021	-5.5
F2	200.0	leuco	1.23	0.27	0.1317	0.50974	0.51153	0.000029	-4.5
F2*	200.0	leuco	2.25	0.51	0.0135	0.50972	0.51155	0.000022	-5.0
F3	200.6	leuco	1.06	0.19	0.1105	0.50965	0.51115	0.000036	-6.3
F4	200.9	leuco	1.00	0.18	0.1067	0.50969	0.51114	0.000031	-5.5
F5	202.2	anoth	1.44	0.25	0.1035	0.50968	0.51109	0.000026	-5.6
Mineral Separates									
HW1P1	187.5	Plag-Anorthosite	0.68	0.11	0.0936	0.50957	0.51084	0.000456	-7.8
HW2P1	191.5	Plag-Leuconorite	1.00	0.13	0.0791	0.50961	0.51069	0.000024	-7.0
RF1P1	192.36	Plag-Pyroxenite	8.84	1.41	0.0964	0.50960	0.51091	0.000108	-7.3
RF2P1	194.6	Plag-Pyroxenite	1.76	0.20	0.0670	0.50960	0.51051	0.001824	-7.3
FW1P1	200	Plag-Leuconorite	0.65	0.10	0.0893	0.50968	0.51089	0.000314	-5.8
FW2P1	202.2	Plag-Anorthosite	0.53	0.08	0.0891	0.50963	0.51083	0.000424	-6.8
HW2PX	191.5	Opx-Leuconorite	0.54	0.21	0.2330	0.50950	0.51267	0.000464	-9.1
RF1PX	192.36	Opx-Pyroxenite	4.67	1.03	0.1333	0.50961	0.51142	0.001628	-7.1
RF2PX	194.6	Opx-Pyroxenite	1.37	0.44	0.1930	0.50961	0.51222	0.000314	-7.1
FW1PX	200	Opx-Leuconorite	0.26	0.11	0.2474	0.50938	0.51273	0.001452	-11.6

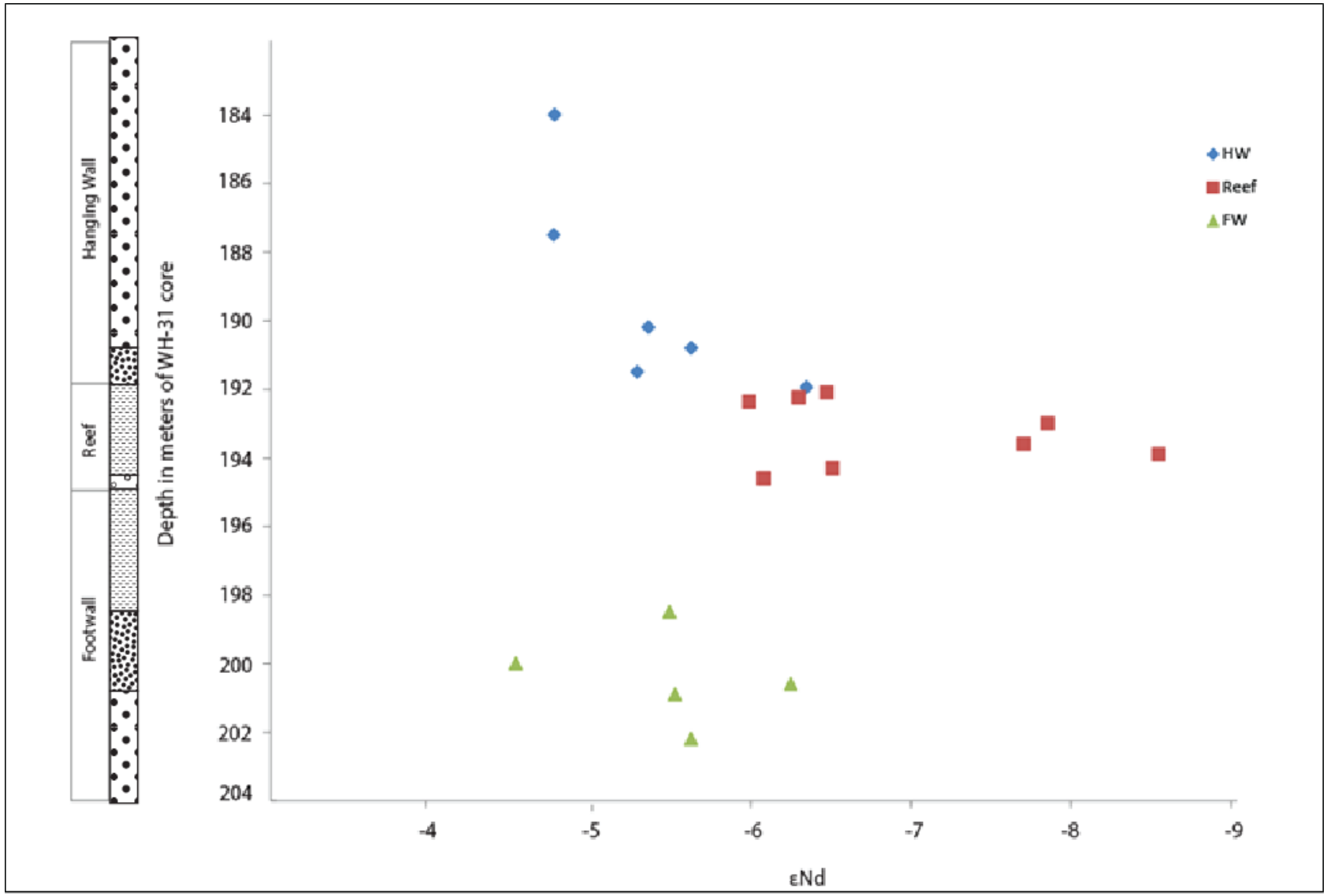

Figure 6.2 Plot of ε_{Nd} values calculated for 2.06 Ga vs. stratigraphic height of the Merensky Cyclic Unit at Winnaarshoek of the eastern Bushveld Complex, illustrating the variation in ε_{Nd} values in each unit. Note the progressive decrease in contamination from to the point of maximum contamination in the reef pegmatoid (ε_{Nd} = -8.5) to the top of the hanging (ε_{Nd} = -4.8). HW and FW stand for hanging wall and footwall respectively.

6.3 Summary of Isotopic Results

The $^{147}Sm/^{144}Nd$ and ε_{Nd} values in measured plagioclase show little variation with increasing stratigraphic height as opposed to orthopyroxene and whole rock $^{147}Sm/^{144}Nd$ and ε_{Nd} values which do show some variation with height (Fig 6.3). Whole rock $^{147}Sm/^{144}Nd$ compositions in the footwall gradually increase reaching a maximum of consistent values in the Reef before gradually declining in the hanging wall to match footwall compositions. The opposite is illustrated by ε_{Nd} values where footwall and hanging wall values are consistent, whereas there is a "spike" of lower values in the Reef. Orthopyroxene shows significant variation in both $^{147}Sm/^{144}Nd$ compositions and ε_{Nd} values with no apparent trend with increasing stratigraphic height. Whole rock $^{147}Sm/^{144}Nd$ compositions are generally greater than plagioclase and less than orthopyroxene $^{147}Sm/^{144}Nd$ compositions but are generally greater than both plagioclase and orthopyroxene in terms of ε_{Nd} values.

The ε_{Nd} values throughout the sample suite indicate that there is a clear "crustal spike" present at the level of the Merensky Reef. This is well illustrated in Figure 6.2 and Figure 6.3 which show an increase in crustal contamination with depth in the hanging wall before reaching maximum contamination in the Reef itself. Results obtained by Maier *et al.* (2000) illustrate peak contamination in the C_UZ in anorthosites directly above the Merensky Reef, whereas this study shows the contamination peak is in the Reef itself. Initial $^{87}Sr/^{86}Sr$ (Sr_0) has been shown to increase with increasing stratigraphic height from the base of the Merensky Reef to the base of the Bastard Reef in both the western (Kruger & Marsh, 1982, 1985; Eales *et al.*, 1990) and eastern (Lee & Butcher, 1990) lobes of the Bushveld Complex. This corresponds to a decrease in ε_{Nd} values with increasing stratigraphic height presented in this study for the eastern Bushveld Complex and by Maier *et al.* (2000) in the western Bushveld. The analytical error on the mineral separate data (corresponding to around $\pm$ 1 ε_{Nd} unit) is greater than that for the whole rocks (around $\pm$ 0.6 ε_{Nd} units), due to the low Nd and Sm abundances in the separates; nonetheless, some patterns are evident. Orthopyroxene ε_{Nd} values show variation outside of analytical error which is not correlated with increasing stratigraphic height, but can be correlated with "within-Reef" and ""outside the Reef" characteristics. Conversely, ε_{Nd} values of plagioclase have little variation and show a very slight decrease (i.e. more contaminated) in ε_{Nd} values with increasing height from -6.8 in the footwall anorthosite to -7.8 in the hanging wall anorthosite. This is consistent with $\delta^{18}O$ data obtained by Schiffries & Rye (1989) for the CZ, MZ and UZ and Harris *et al.* (2005) for the UZ and MZ. It is important to consider the effect of

analytical errors on the "spike". Errors on mineral separate data were anomalously high due to reasons mentioned earlier; however the error on whole rock isotope data is acceptable and should not greatly influence the basic premise of the postulated models.

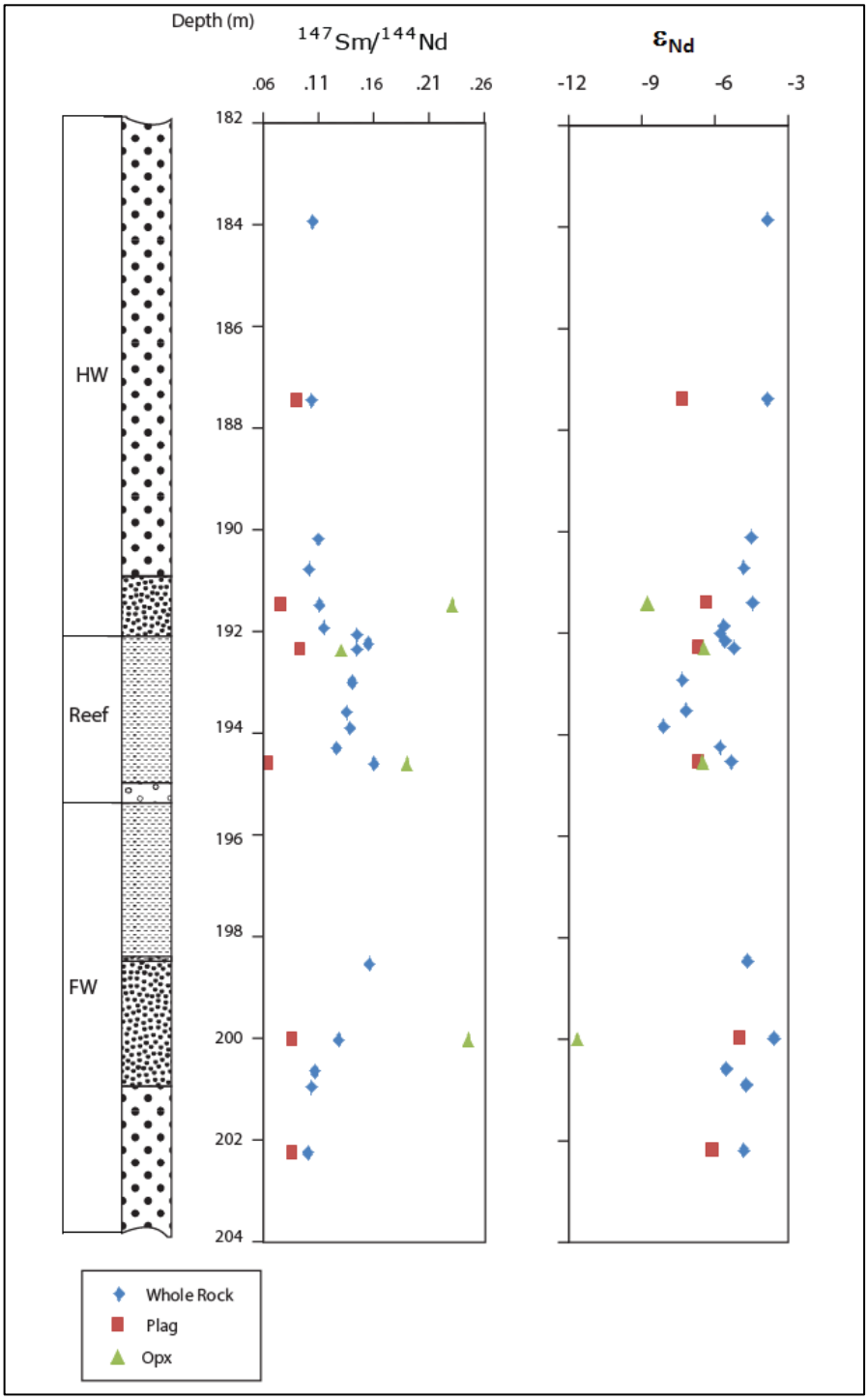

Figure 6.3 $^{147}Sm/^{144}Nd$ ratios and ε_{Nd} values in measured whole rock, plagioclase and orthopyroxene at Winnaarshoek of the eastern Bushveld Complex expressed as a function of height. Analytical uncertainties are smaller than the symbols shown.

Chapter 7- Discussion

7.1 Evidence of Disequilibrium

7.1.1 Petrography and mineral compositions

The following lines of evidence can be interpreted as being due to a lack of disequilibrium in the sample suite of rocks. Such evidence is found in petrographic textures, mineralogical compositions, and isotopic compositional disequilibrium. Textural evidence occurring in the studied rocks include: clinopyroxene exsolution lamellae in orthopyroxene; resorbed plagioclase in orthopyroxene or relict plagioclase; various inclusions such as orthopyroxene, plagioclase or clinopyroxene in larger oikocrysts of clinopyroxene or orthopyroxene; discontinuous rims of clinopyroxene surrounding orthopyroxene; resorbed orthopyroxene in clinopyroxene; and corona textures associated with olivine. In terms of compositional disequilibrium, evidence is presented in the range of compositions found in orthopyroxene, plagioclase and clinopyroxene with stratigraphic height with particular reference to the change in mineral composition in each unit (hanging wall, reef, and footwall). Compositions of minerals are also compared in similar rock types which occur separately in different units. In all three units, mean An content in plagioclase chadocrysts is greater than that in cumulus and interstitial plagioclase. There does not appear to be any compositional difference between chadocrysts hosted by earlier plagioclase or orthopyroxene.

Most of the textures evident in clinopyroxene mentioned above have similar compositions especially in terms of Mg numbers; however there are exceptions to this. Clinopyroxene occurring as interstitial liquid has a mean Mg # slightly higher than the mean compositional values of clinopyroxene exsolution lamellae, inclusions and discontinuous rims; while clinopyroxene oikocrysts have a significantly lower mean Mg # than these textures and are compositionally more similar to measured orthopyroxene Mg numbers, which is what is expected in "normal" equilibrium reactions between clinopyroxene and associated orthopyroxene. This indicates that clinopyroxene interstitial/trapped liquid is less evolved than other the other textures of clinopyroxene, while the oikocrysts are more evolved. These features represent and provide evidence for both textural and compositional disequilibrium throughout the sampled sequence.

The existence of plagioclase chadocrysts and inclusions within larger orthopyroxene grains indicates that plagioclase had already crystallized prior to the crystallization of orthopyroxene. Further evidence of early plagioclase crystallization is the inclusions of tricuspate-shaped plagioclase relicts within later plagioclase and orthopyroxene, as well as plagioclase with deformed twins in association with 'regular' (undeformed) plagioclase grains. The incorporation and resorption of earlier crystallized laths of plagioclase in orthopyroxene indicates interaction with a more evolved melt with subsequent incorporation into newly crystallized assemblages such as orthopyroxene or clinopyroxene oikocrysts. This is supported by polyphase inclusions of plagioclase and clinopyroxene in orthopyroxene oikocrysts. If only resorbed plagioclase was found included in orthopyroxene, this would imply that othopyroxene is also xenocrystic to its host rock and may have crystallized elsewhere as well. However, plagioclase inclusions are found in other plagioclase grains and some relict orthopyroxene also occurs in plagioclase grains, implying that orthopyroxene crystallized in-situ. This would require three separate stages of growth; a) initial plagioclase crystallization, b) incorporation into a second melt followed by plagioclase resorption and subsequent incorporation of the new crystals within the same melt; and c) the transportation of oikocrysts to a new assemblage.

In order to evaluate this it is necessary to evaluate resorbed plagioclase chadocrysts to test first, if they are compositionally different from the groundmass plagioclase and secondly, whether plagioclase is in thermal or compositional equilibrium with their host orthopyroxene. This early plagioclase crystallization and subsequent orthopyroxene crystallization can be depicted using the An-Fo-SiO_2 ternary phase diagram where plagioclase crystallizes out of the melt and exists in equilibrium with the residual liquid in bivariate field "A" (Fig. 7.1). As the system cools it begins to approach the An-Fo-En-liquid peritectic (point "x"). The absence of cumulus olivine supports a starting composition in field "A", or would allow for a starting composition in field "B" in which any Fo that may have crystallized was consumed at the peritectic. As the liquid composition approaches cotectic point "z", upon further cooling, a siliceous phase comes into consideration. The addition of silica would then be consistent with the crustal contamination models discussed in section 7.4, particularly in reference to the Reef.

The above phase equilibration sequence is representative of the hanging wall and Reef, however, the relationship in the footwall is slightly different due to the increased presence of olivine. Plagioclase in the footwall leuconorite can be found as resorbed grains within host olivine. Olivine exists as an

interstitial phase, but also occurs as rounded, serpentinized inclusions in orthopyroxene. Texturally, this supports early plagioclase crystallization followed by olivine and finally orthopyroxene crystallization. This can be depicted using the An-Fo-SiO_2 ternary phase diagram (Fig. 7.1), where once again plagioclase is in equilibrium with the liquid in either field "B" or "C". In the case of field "B"; the system cools and approaches the An-Fo-liquid cotectic (point "y"). Plagioclase and olivine are now in equilibrium with each other and the liquid at this point. Further cooling allows the bulk composition to move further down the liquid line of descent until it reaches the ternary peritectic at point "x", where all three phases can exist in equilibrium with the liquid. A rock with a bulk composition with plag-ol-opx could start in field "C"; however, it is unlikely that this sequence would be followed because a composition starting in field "C" would use up all the liquid before olivine is consumed. This is required in order to preserve olivine in the final rock with a plag-ol-opx crystallization sequence as olivine consumption leads to the orthopyroxene development as expressed by the following equation:

$CaAl_2Si_2O_8$(Plag) + **Mg_2SiO_4**(ol) + **liquid 1 = $CaAl_2Si_2O_8$**(Plag) + **$MgSiO_3$**(Opx) + **residual liquid**

The implication of the different units starting in different bivariate fields is that there could be at least two magmas responsible for the formation of the hanging wall, Reef and footwall units. One magma which crystallized the assemblages seen in the hanging wall and Reef, and another magma, slightly different in bulk composition, responsible for the footwall assemblage. It is also necessary to consider the effect of re-equilibration with variable amounts of trapped liquid, as this can vary in different rock types and that mineral variations may be a result of the amount of trapped liquid present in each lithology.

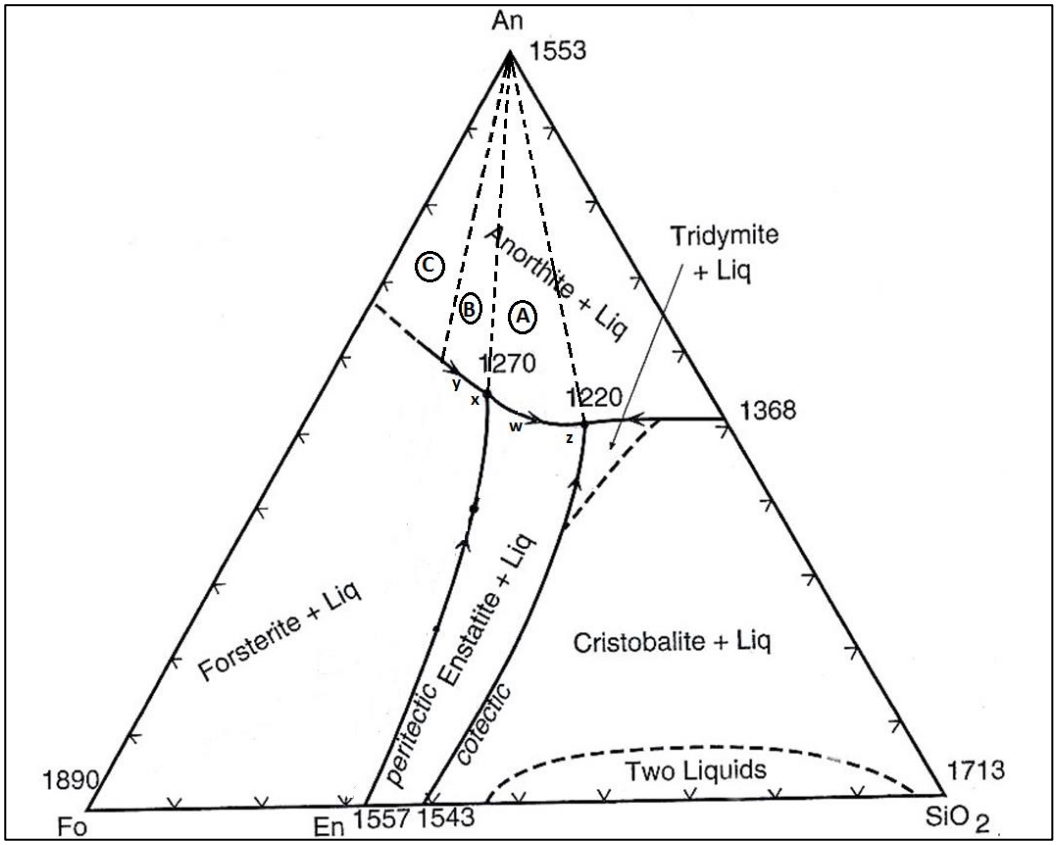

Figure 7.1 Isobaric diagrams illustrating the cotectic and peritectic curves in the An-Fo-Si system at 0.1 MPa. After (Anderson, 1915). Bivariate fields A, B and C are the fields where plagioclase-first crystallization (followed by either olivine and/or orthopyroxene) is supported. w= An-En-liq cotectic; x= plag-ol-opx-liq peritectic; y= plag-ol-liq cotectic; z= An-En-SiO_2-liq ternary eutectic.

Discontinuous clinopyroxene rims surrounding orthopyroxene may represent;

a) a trapped interstitial liquid crystallizing to form clinopyroxene;
b) A reaction between early orthopyroxene and liquid to produce clinopyroxene at the expense of the existing pyroxene;
c) The migration of exsolved clinopyroxene in host orthopyroxene to the grain boundaries of the host

Crystallization of a trapped later liquid should be manifested by relatively evolved clinopyroxene compositions of the rims. A liquid-orthopyroxene reaction is not expected to be discontinuous

and is not apparently supported by phase equilibria associations but may be superficially represented by the following equation:

$MgSiO_3$(Opx) + **$CaAl_2Si_2O_8$**(Plag) + **Liquid 1** = **$CaMgSi_2O_6$**(Cpx) + **residual liquid**

The discontinuous rims could also represent the migration of exsolved clinopyroxene in host orthopyroxene to the grain boundaries of the host. Sub-solidus migration would then be enabled by lengthy periods of high temperature cooling and the systematic removal of high-Ca pyroxene to grain boundaries and subsequent migration along these grain boundaries.

Resorbed orthopyroxene surrounded by oikocrystic clinopyroxene is resorbed by the reaction with an evolved liquid allowing for clinopyroxene to nucleate onto the dissolving orthopyroxene. The rims would then be expected to be more evolved than early clinopyroxene which exsolved from orthopyroxene. This is not the case as clinopyroxene rims and exsolutions have the same Mg# composition (Table 5.2). The existence of rims at opx-opx and plag-opx boundaries indicates no preferential migrational bias. The presence of resorbed orthopyroxene enclosed by a clinopyroxene host indicates that orthopyroxene crystallized prior to clinopyroxene and was then resorbed and incorporated within another melt which then crystallized interstitial clinopyroxene in this trapped liquid.

Plagioclase grains enclosed within orthopyroxene suggests that although orthopyroxene is the dominant cumulus phase (in the Reef), crystallization occurred after that of plagioclase and may be indicative of more than one crystallization event i.e. an influx and subsequent mixing and crystallization of a second magma, possibly supporting a lateral emplacement model for the Merensky Reef (see section 7.5). Triple-junctions of orthopyroxene in pyroxenite suggest that orthopyroxene has undergone some recrystallization and that orthopyroxenes in the Reef are in textural equilibrium. Clinopyroxene hosting partially resorbed orthopyroxene indicates that orthopyroxene crystallization precedes that of clinopyroxene within the melt. Clinopyroxene oikocrysts may then have developed in-situ, allowing for the incorporation and resorption of plagioclase and orthopyroxene inclusions (with resorbed opx and plag preceding cpx crystallization) or may have been developed elsewhere and been transported to their current position as xenocrysts within a later stage melt.

7.1.2 Sm-Nd isotopic evidence for disequilibrium

Sm-Nd isotopic disequilibrium is evident in both the whole rock isotopic data as well as mineral separate data. Whole rock ε_{Nd} values show a "spike" in the Reef where values are significantly lower than that of the hanging wall or footwall units. The hanging wall whole rock samples show a slightly different trend to the Reef and footwall (Fig. 6.1); favouring the 2.06 Ga reference isochron with an initial ε_{Nd} value of -4.7 as opposed to the Reef and footwall samples which align with the 2.06 Ga reference isochron with an initial ε_{Nd} value of -7.3. There does not seem to be an obvious analytical explanation so another mineral phase such as clinopyroxene or REE-bearing apatite could account for this discrepancy. Although not documented here, Mitchell & Scoon (2007) described "small but significant quantities of apatite and loveringite" (which is a REE-bearing late magmatic oxide mineral) in a similar section at Winaarshoek. This REE discrepency is discussed further in in the following sub-section. Mineral separate isotope data show that ε_{Nd} values in plagioclase grains are more primitive (i.e. less negative values) than their corresponding orthopyroxene grains. Footwall and hanging wall plagioclase and orthopyroxene are isotopically similar, whereas plagioclase and orthopyroxene in the Reef are dissimilar. This supports models where the Reef is genetically distinct from its host rocks (i.e. the hanging wall and footwall- see section 7.4).

The implication of these disequilibrium features is that the resultant rocks and textures cannot be solely the product of one fractionating magma and that multiple magma pulses (Kruger & Marsh, 1982) or secondary igneous or hydrothermal processes are required (Nicholson & Mathez, 1991; Boudreau, 2008; Chutas *et al.,* 2012). This implies that mixing of magmas of contrasting temperature, origin and composition took place (Eales & Cawthorn, 1996). It is then important to determine whether the new influxes of magma are multiple pulses of the same magma or if magmas of different compositions are interacting with residual liquid and crystal mush. Compositional and isotopic disequilibrium may not always be the result of multiple pulses and could in fact just be the product of crystals from greater depths being transported by a new liquid and settling or recrystallizing in a new location. The inherited crystals may have been in equilibrium in their previous setting yet are now in disequilibrium with their new host magma or crystal mush. If this is the case one would expect to find several examples in the newly crystalized rock with similar signatures (compositional and isotopic) to the original source rocks at depth. Couch *et al.* (2001)

have also proposed that certain instances of disequilibrium are the result of convection within a magma body of homogenous composition that is heated from below and cooled from above.

7.2 Evidence for magma- crystal mixing

When whole rock and mineral separate isotopic data are plotted on an isochron diagram (Fig. 6.1) there is both evidence for and against isotopic disequilibrium. Plagioclase and orthopyroxene in the Reef are collinear both plotting on the 2.06 Ga reference isochron with an initial ε_{Nd} value of -7.3. This would indicate that they are in isotopic equilibrium. If plagioclase and orthopyroxene had crystallized from a parent magma in equilibrium, then you would expect them to have indistinguishable initial isotopic compositions, otherwise the implication is that they were not in equilibrium with a common, homogenous isotopic reservoir. This is the case in the Reef itself but not true for samples in the hanging wall and footwall. This would imply that coexisting plagioclase and orthopyroxene in the hanging wall and footwall are not in equilibrium as they do not plot on the same reference isochron. This may imply disequilibrium by some process may have resulted in a lower initial $^{143}Nd/^{144}Nd$ ratio in orthopyroxene and higher initial $^{143}Nd/^{144}Nd$ ratio in plagioclase (Table 6.1) which corresponds to slightly more contaminated and less contaminated ε_{Nd} values in orthopyroxene and plagioclase respectively, within the hanging wall and footwall. This is in relation to corresponding orthopyroxene and plagioclase isotopic compositions of different lithologies at different depths. Although plagioclase values are more primitive they are by no means depleted as their corresponding ε_{Nd} values are still significantly less than zero. This data concurs with results obtained by Prevec *et al.* (2005) where plagioclase and whole rock data show similar characteristics at the Merensky Reef in the western Bushveld Complex.

The contrast in plagioclase and orthopyroxene isotopic composition may have resulted from plagioclase crystallizing from a distinct magma to that which crystallized the orthopyroxene. These could originate from enriched crust or magma contaminated by large quantities of crustal matter as magma migration occurs. Orthopyroxene shows a greater degree of contamination relative to plagioclase which could mean that orthopyroxene was exposed to more extensive contamination at the time of crystallization. Plagioclase would not then have to be contaminated to the same degree as orthopyroxene; as Ashwal *et al.* (1992) concluded that plagioclase is less affected by crustal contamination relative to other minerals which show greater contamination values, resulting in more

primitive plagioclase isotopic compositions. This may imply that plagioclase crystallized from a separate magma to orthopyroxene and the resultant mixing caused greater contamination in pre-existing and newly crystallized orthopyroxenes. Isotopic disequilibrium between plagioclase and orthopyroxene could be the result of crustal contamination during primary magmatism, secondary magmatic processes such as magma mixing and/or late magmatic fluid processes, or a combination of all of these processes. If this is the case parent magma would contain different isotopically-enriched components in order to crystallize cumulus rocks with different isotopic signatures. Primary and secondary models are considered as follows:

1. Primary magmatic models:
    a. One parent magma- this would be required to produce heterogeneous mineral isotopic compositions (Irvine, 1977). In order to accomplish this, the timing of contamination and crystallization become important. In this case plagioclase would have to crystallize first followed by magma contamination and subsequent orthopyroxene crystallization. This consistent with the crystallization sequence but issues arise if orthopyroxene is more evolved than the coexisting plagioclase composition.
    b. Multiple parent magmas- this requires two or possibly more magmas, each predominantly crystallizing different minerals with distinct isotopic compositions (Kruger & Marsh, 1982). For instance a plagioclase-saturated magma would crystallize plagioclase predominantly, while an orthopyroxene-saturated magma would predominantly crystallize orthopyroxene. These minerals assemblages would interact and be variably mixed creating hetrogenous isotopic compositions.

2. Secondary magmatic models:
    a. Trapped residual liquids- it may be possible for a cumulate mineral assemblage to be affected by the infiltration of trapped liquids from a separate magma. Compaction and liquid migration can result in the infiltration of silicate liquids into rocks with a different isotopic composition (Boorman *et al.,* 2004). If this is the case it could influence the manner and extent of contamination in different minerals. Orthopyroxene is more likely to have a variable budget of Sr and REE initially than plagioclase because it generally contains less Sr and REE to begin with. Diffusion

rates are an important factor here as they influence the susceptibility of minerals to be contaminated as ions will not be exchanged equally according to the different mineral structures. For example Sr and REE should follow Ca into plagioclase and clinopyroxene while orthopyroxene may accommodate HREE in solid solution with Fe and Mg or minor amounts of Ca which is also present in orthopyroxene and would explain why the REE content in orthopyroxene is so much thess than that of clinopyroxene. Sr is compatible in plagioclase, while Pb, U and Rb are incompatible in both plagioclase and orthopyroxene (Bedard, 1994) and so Sr and Pb in plagioclase should fall on a mixing line for equilibration partitioning between the parent melt, the B1 melt and the mineral (Chutas *et al.,* 2012). Orthopyroxene contains little Rb and Pb relative to other trace elements and so slight interactions with a silicate liquid enriched in Rb or Pb can affect their resevoirs in orthopyroxene to a larger degree than it would for other elements in orthopyroxene as well as other elements in plagioclase (Chutas *et al.,* 2012).

b. Late magmatic fluid control- this would involve the presence of upward percolating hyrdrous fluids (Nicholson & Mathez, 1991; Boudreau, 2008) as opposed to silicate magmas. The concept is similar to that described above, the main difference being the effect on the movement of more mobile elements. Hydrous fluids should better facilitate the movement of Rb and U over Sr and Pb, which is in turn better mobilized than the REE. The metasomatized rocks enriched in PGE have been suggested by some to be evidence that this metasomatic process may be responsible for PGE enrichment within the Merensky Reef (Mathez, 1995).

The fact that the whole rock isotope samples do not plot on the same reference isochron (Fig. 6.1) as their constituent minerals is problematic but not all together inexplicable. Abundances of Sm and Nd in the whole rock are generally higher than in the plagioclase and orthopyroxene separates. This could indicate that REE-bearing accessory phases such as apatite are present in the whole rock. Interstitial clinopyroxenes have also been shown to have higher REE contents than their cumulate hosts (Mathez, 1995). Rocks in this study have shown a high, albeit variable amount of interstitial clinopyroxene throughout the sampled sequence which could account for the larger initial Nd^{143}/Nd^{144} ratio values in the whole rock than coexisting plagioclase and orthopyroxene. Although

REE abundances were not measured for whole rocks or mineral separates in this study several authors have conducted such studies. Their results are plotted below for REE in the whole rock (Fig.7.2; Mitchell & Scoon, 2007) as well as for mineral separates of clinopyroxene (Fig.7.3a), orthopyroxene (Fig.7.3b) and apatite (Fig.7.3c; Mathez, 1995). The whole rock REE values (Fig.7.2) obtained by Mitchell & Scoon (2007) span a section from hanging wall through the Reef to the footwall in a similar fashion to sampling methods used in this study and are also from Winnaarshoek in the eastern Bushveld Complex. Their whole rock values for Sm and Nd abundances are comparable to values obtained in this study. Sm and Nd abundances in orthopyroxenes (Fig.7.3b) obtained by Mathez (1995) from the Atok Section in the northeastern Bushveld Complex are also comparable to those recorded in this study, however, it is their clinopyroxene (Fig.7.3a) and apatite (Fig.7.3c) data which is of real interest. As can be seen in the figures the abundances of all REE (except Eu) are significantly greater than those found in orthopyroxene particularly in apatite where abundances are four orders of magnitude greater than orthopyroxene. Mathez (1995) showed that interstitial minerals with which the Merensky Reef equilibrated are LREE enriched and that compositions of cumulus clinopyroxene and plagioclase infer that the initial Bushveld magma had six times more LREE than HREE, typical of continental basalts. This enriched nature indicates crustal contamination preceding emplacement which is consistent with radiogenic (Kruger & Marsh, 1982; Sharpe, 1985; Maier *et al.,* 2000; Prevec *et al.,* 2005; Maier *et al.,* 2013) and stable isotope data (Schiffries & Rye, 1989; Harris *et al.,* 2005).

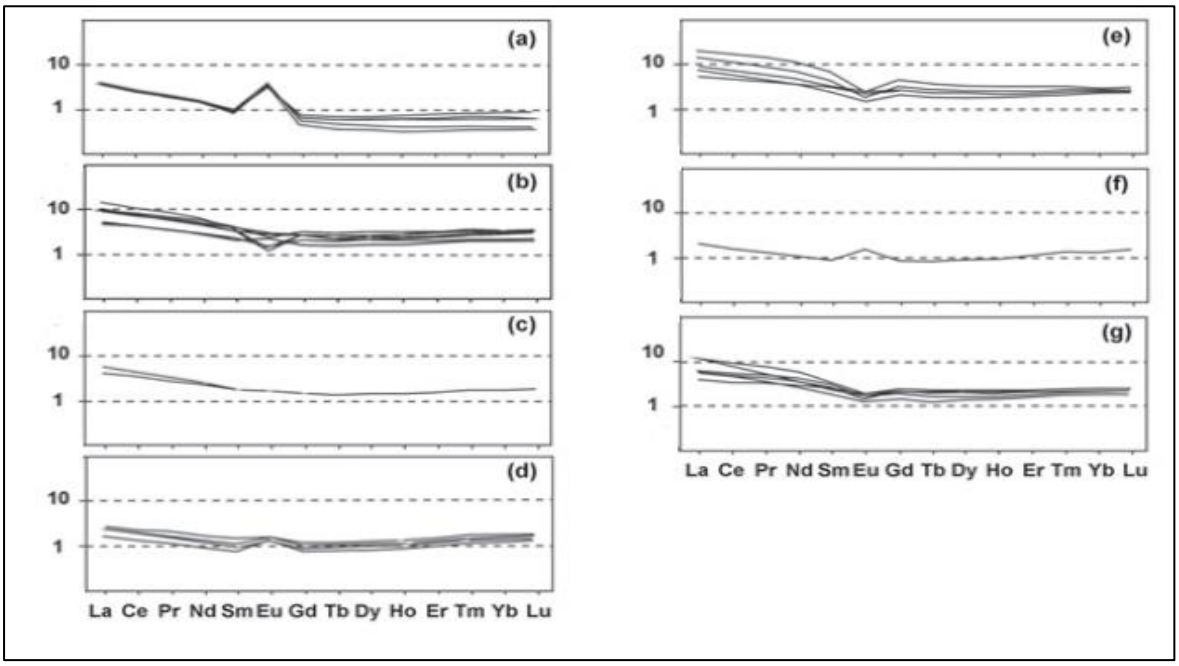

Figure 7.2 Chondrite-normalized whole rock REE contents of the Merensky Reef at Winnarshoek in the eastern Bushveld Complex obtained from Mitchell & Scoon (2007). (a-b) represent hanging wall samples, (c-f) represent Reef samples and (f) represents the footwall.

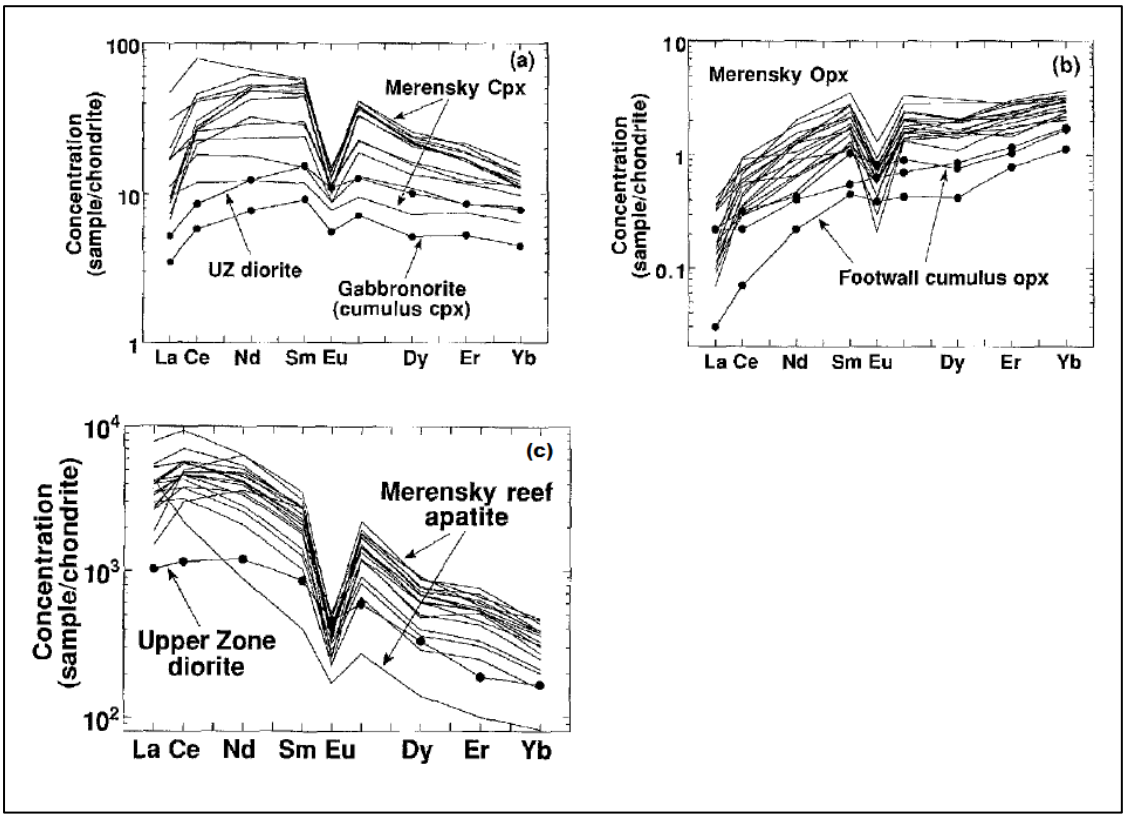

Figure 7.3 Chondrite-normalized REE contents of (a) clinopyroxene, (b) orthopyroxene and (c) apatite from the Merensky Reef at Atok Section in the northeastern Bushveld Complex obtained by Mathez (1995).

7.3 Features of the Mineralized Reef Zone

Texturally, the main differences between the Reef and the hanging wall and footwall are the cumulus phases. The Reef is dominated by cumulus orthopyroxene while the hanging wall and footwall units are dominated by cumulus plagioclase with orthopyroxene occurring primarily as an interstitial phase. Orthopyroxene in the Reef is general euhedral while in the hanging wall and footwall it is mostly subhedral. Base-metal sulphides occur in the Reef in abundance but only scarcely in the the footwall and are absent in the hangingwall. Pegmatoidal features are present in the pegmatoidal pyroxenite where grain sizes of the major constituent minerals are coarser than in the 'normal' pyroxenite. Pegmatoidal features also occur in one sample from the footwall leuconorite which shows increased grain size and has the odd 'coronitic' textures mentioned in previous chapters. From a microtextural point of view the Reef bears similar features to those found in the hanging wall and footwall, with some exceptions. Exsolution lamellae are common throughout the sampled sequence. Orthopyroxenes in the reef however, have been exsolved to a much greater extent, often showing very irregular exsolutions of clinopyroxene in orthopyroxene hosts. Triple junctions of orthopyroxene are also confined to the Reef and Reef pegmatoid indicating a certain degree of recrystallization took place. Deformed plagioclase twins in the Reef may indicate that plagioclase may have been transported in as a solid or be residual plagioclase after partial melting took place resulting in the evident deformation feature.

General petrographic observations are comparable to those made by Cameron (1982) and Mitchell & Scoon (2007) on the Merensky Reef in the eastern Bushveld Complex. Throughout the Merensky Cyclic Unit from hanging wall through the Reef to the footwall, the primary igneous textures are well preserved. Exceptions occur sporadically as a result of fluid interaction attributed to thermal and hydrothermal processes which are particularly evident in the Reef pegmatoid and Merensky footwall rocks (Cawthorn, 1999a). These exceptions occur as minor alterations of olivine (where present) to serpentine and plagioclase to sericite. Sericitic alteration is not particularly common in this sample suite. The general absence of olivine in the Winnaarshoek samples has also been documented by Mitchell & Scoon (2007), who account for the lack of olivine due to the Winnaarshoek "facies" being formed at more passive conditions at lower temperatures than elsewhere (e.g. Swartklip facies). Most of the textural observations made are consistent with those of previous authors on the Merensky Reef, for example Cameron (1982) and Eales *et al.* (1990) reported the presence of plagioclase chadocrysts included in large orthopyroxene grains while

Cawthorn (1999a) identified sericitic alteration and ophitic textures of orthopyroxene in footwall leuconorites. Cawthorne & Boerst (2006) recognized inclusions of tricuspate shaped plagioclase grains included in orthopyroxene of the Reef pegmatoid, a feature which is also noted in this study. Also noted in this study is the presence of irregular tricuspate plagioclase included in other plagioclase grains (Fig. 4.10D). Corona textures on olivine observed in the footwall leuconorite are scarcely mentioned in literature for the Critical Zone of the Bushveld Complex. Maier (1991) recognized "corona structures" of euhedral olivine surrounded by plagioclase halos in the UG2 footwall, although these textures differ markedly to the "coronas" presented in this study, whereby the "corona texture" consists of orthopyroxene followed by a thin corona of pargasite or clinozoisite and bordered by plagioclase (Fig. 4.12 D, E, F).

Compositionally, orthopyroxene throughout the sampled sequence shows little variation in terms of mean Mg number. Conversely, plagioclase does show variation with mean An content in the Reef pyroxenites significantly lower than that of the hanging wall and footwall rocks. Orthopyroxene in the Reef pyroxenite and pegmatoidal pyroxenite (Mg# = 81.1 and 81.8, respectively) have more comparable compositions to the footwall leuconorites and anorthosites (Mg# = 81.9 and 81.7, respectively) than to the hanging wall anorthosites and leuconorites (Mg# = 78.0 and 77.2, respectively). An content in plagioclases from the Reef are markedly lower for the pyroxenite and pegmatoidal pyroxenite ($An_{62.6}$ and $An_{63.1}$, respectively) compared to the footwall leuconorite and anorthosite ($An_{72.5}$ and $An_{73.8}$, respectively); and hanging wall anorthosite and leuconorite ($An_{76.9}$ and $An_{73.6}$, respectively). The lack of a clear cut trend with increasing height for orthopyroxene is consistent with results obtained by Mitchell & Scoon (2007) but differ to those obtained by Kruger and Marsh (1985), who presented a decline in Mg# values with increasing stratigraphic height. The general homogeneity in orthopyroxene compositions is accounted for by subsolidus slow cooling where only the movement of Mg^{2+} and Fe^{2+} are required in order to reach homogenization.

Relicts of orthopyroxene in plagioclase show no anomalously lower or higher values than other orthopyroxene grains. This may indicate that some resorption of orthopyroxene took place as plagioclase from a separate melt crystallized. As new plagioclase crystallizes, relict grains from a residual liquid which have already crystallized would be incorporated into the new melt. Resorption of these grains would then take place specifically at the grain boundaries causing a rounding effect on the relict crystal. If this is the case then the resorbed orthopyroxene would not be expected to have a different composition to larger, older crystals (except perhaps near the rim where the relict

interacted with the new melt at the grain boundary interface). Plagioclase compositional variation shows a gradual decrease with height from the footwall rocks to the Merensky Reef where a significant decrease in An content is illustrated before a gradual increase in An content occurs from the Reef to the overlying hanging wall lithologies. This is consistent with results obtained by Kruger & Marsh (1982) and Mitchell & Scoon (2007). The range in plagioclase composition is variable but generally quite large compositional ranges are presented for each unit, especially in the footwall (Fig. 5.8). Mean compositions of plagioclase inclusions in the hanging wall ($An_{79.77}$) and footwall ($An_{77.26}$) are comparable while compositions of inclusions in the Reef ($An_{65.11}$) are significantly lower. This large range in composition is accounted for by the high energy processes required to modify plagioclase by breaking up the (Si-Al)-O_4 tetrahedra in order to allow Ca-Na substitutions. These data are comparable to data presented by Eales *et al.* (1990) where inclusions and chadocrysts are more calcic then cumulus or interstitial plagioclase grains. The implications of more calcic inclusions of plagioclase than cumulus or interstitial material is that the inclusions may represent an earlier crystallization event. An influx of magma would then incorporate these plagioclase inclusions as resorbed relict grains whose original chemical compositions are maintained. As a result of mixing and recrystallization it is perceivable that the newly crystallized plagioclase grains would have a different chemical composition than those that crystallized earlier. Cameron (1982) conducted work indicating that plagioclase crystallizing under normal circumstances in layered intrusions should yield compositions in range of An_{75} to An_{82}. Compositions outside this range may then have been affected by external or secondary processes such as magma mixing or hydrothermal fluids. The mean plagioclase compositions in the hanging wall and footwall generally fall just short of this compositional range and will have then likely been affected by a secondary igneous process. Mean plagioclase compositions in the Reef are significantly lower than the given range and are most likely severely affected by a secondary igneous process such as magma mixing and hydrothermal activity or a combination of both resulting in more variable mineral compositions. This is supported by plagioclase relicts with higher An content than regular plagioclase grains as well as the pegmatoidal nature of the lower portion of the Reef pyroxenite which infers hydrothermal fluid interaction.

7.4 Contamination

Evidence for contamination in the C_UZ is well documented in literature especially for Sr isotopic data (e.g. Kruger & Marsh, 1982, 1985; Eales *et al.*, 1990; Lee & Butcher, 1990). In contrast, relatively little Sm-Nd isotopic data are available, however more authors have begun using the Sm-Nd system to constrain the contamination in recent literature (e.g. Maier *et al.,* 2000; Prevec *et al.,* 2005) as well as in this study. $\delta^{18}O$ isotope data is also a relatively small database in relation to Sr isotope data; but has also been used in an attempt to constrain the effect of contamination in the UZ, MZ and CZ of the Bushveld Complex (e.g. Schiffries & Rye, 1989; Harris *et al.,* 2005). Existing initial $^{87}Sr/^{86}Sr$ (Sr_0) data shows an increase in Sr_i with increasing stratigraphic height from the base of the Merensky Cyclic Unit to that of the Bastard Unit Cycle in the western (Kruger & Marsh, 1982, 1985; Eales *et al.*, 1990) and eastern (Lee & Butcher, 1990) lobes of the Bushveld Complex. The corresponding inverse relationship is true for ε_{Nd} which presents a decrease in ε_{Nd} values with increasing stratigraphic height (Maier *et al.,* 2000). Measured orthopyroxene ε_{Nd} values in this study show some variation but no clear trend with increasing stratigraphic height, while coexisting ε_{Nd} values of plagioclase have little variation and show a very slight decrease in ε_{Nd} values with increasing height. This is also consistent with $\delta^{18}O$ plagioclase data which shows little variation with increasing stratigraphic height in the RLS (Schiffries & Rye, 1989; Harris *et al.,* 2005) and Platreef (Harris & Chaumba *et al.,* 2001) of the Bushveld Complex. Harris *et al.* (2005) recorded data with $\delta^{18}O$ values which are an average of 1·4‰ higher than expected in an uncontaminated mantle-derived magma which should have an $\delta^{18}O$ value 5·7‰, invoking crustal contamination as the likely reason for such high $\delta^{18}O$ values.

7.4.1 Modeling the Contamination

In an attempt to constrain the contamination processes, there are two possible end member compositions to consider. The possible end member compositions could be derived from the mantle (i.e. mantle-derived magmas) or from crustally contaminated components as discussed below. Modeling has been undertaken assuming simple mixing of mantle and crustal end-members, without accounting for the effects of crystallization enhanced by the energy used during assimilation.

Since the bulk crystallizing assemblage has $D^{REE}<1$, we can assume that the amount of crustal contamination modelled will be a minimum value.

7.4.1.1 Mantle-derived magma

Three prospective mantle-derived end-member compositions can be realistically modeled. The first of the mantle-derived possible source magmas is a "depleted" or "depleting" mantle reservoir compositions as modeled by DePaolo (1981) with an ε_{Nd} value of approximately +3.3 at 2.06 Ga (Fig. 7.4). The second magma source is derived from enriched, near-chondritic mantle (i.e. CHUR) with an ε_{Nd} value = 0. The third potential mantle source is enriched mantle represented by Barberton komatiites aged ca. 3.45 Ga (5 ppm Nd) and 3.3 Ga (6 ppm Nd; Lahaye *et al.,* 1995) respectively, which are only slightly more depleted than the most depleted Bushveld Complex samples at Winnaarshoek (Fig. 7.4) at the time of the emplacement of the Bushveld Complex.

7.4.1.2 Crustal contaminants

The Bushveld Complex was emplaced into sedimentary successions of the Transvaal Supergroup. It is therefore pertinent to consider rocks of the Transvaal Supergroup as potential contaminants. Available data for 2.5 Ga metapelites of the Black Reef formation yield ε_{Nd} value of approximately -7 at 2.06 Ga (Fig. 7.4) with an average Nd concentration of 23 ppm (Dia, *et al.,* 1990; Jahn & Condie, 1995). This is within range of the most contaminated sample from Winnaarshoek with an ε_{Nd} value of -8.5. Older basement rocks must also be considered as potential contaminants as Bushveld magmas may have interacted and assimilated these crustal components upon ascension. Available data produced by Schoene *et al.* (2009) for older than 3.45 Ga crust (34 ppm Nd); 3.2-3.3 Ga crust (26 ppm Nd); and 3.1 Ga crust (39 ppm Nd) yields ε_{Nd} values of -15.0, -16.0 and -14.0, respectively at a Bushveld age of 2.06 Ga (Fig. 7.4). Each of the aforementioned values show significantly more contamination than the most contaminated Bushveld rocks from this sample set. Granitic plutons from the upper crust are also considered as potential contaminants for the same reason mentioned above. Sm-Nd data obtained for the 2.78 Ga Turfloop Batholith (28 ppm Nd; Henderson *et al.*, 2000) and 2.73 Ga granites (97 ppm Nd) of the eastern Kaapvaal Craton (Schoene *et al.,* 2009) yield ε_{Nd} values of -10.0 and -15.0, respectively at 2.06 Ga. The Turfloop Batholith is then only slightly

more contaminated than the maximum contaminated sample from Winnaarshoek. Data acquired from Buchanan *et al.* (2004) for the Rooiberg Felsites gives a range in ε_{Nd} values from -6.5 to -10.0. The Rooiberg Suite has an almost identical age to the Rustenburg Layered Suite leading some authors to believe they are cogenetic (e.g. Buchanan *et al.,* 2004; Mathez *et al.,* 2013). It is unlikely that it could act as a major contaminant as it probably would not be able to significantly change the ε_{Nd} value (Fig. 7.5).

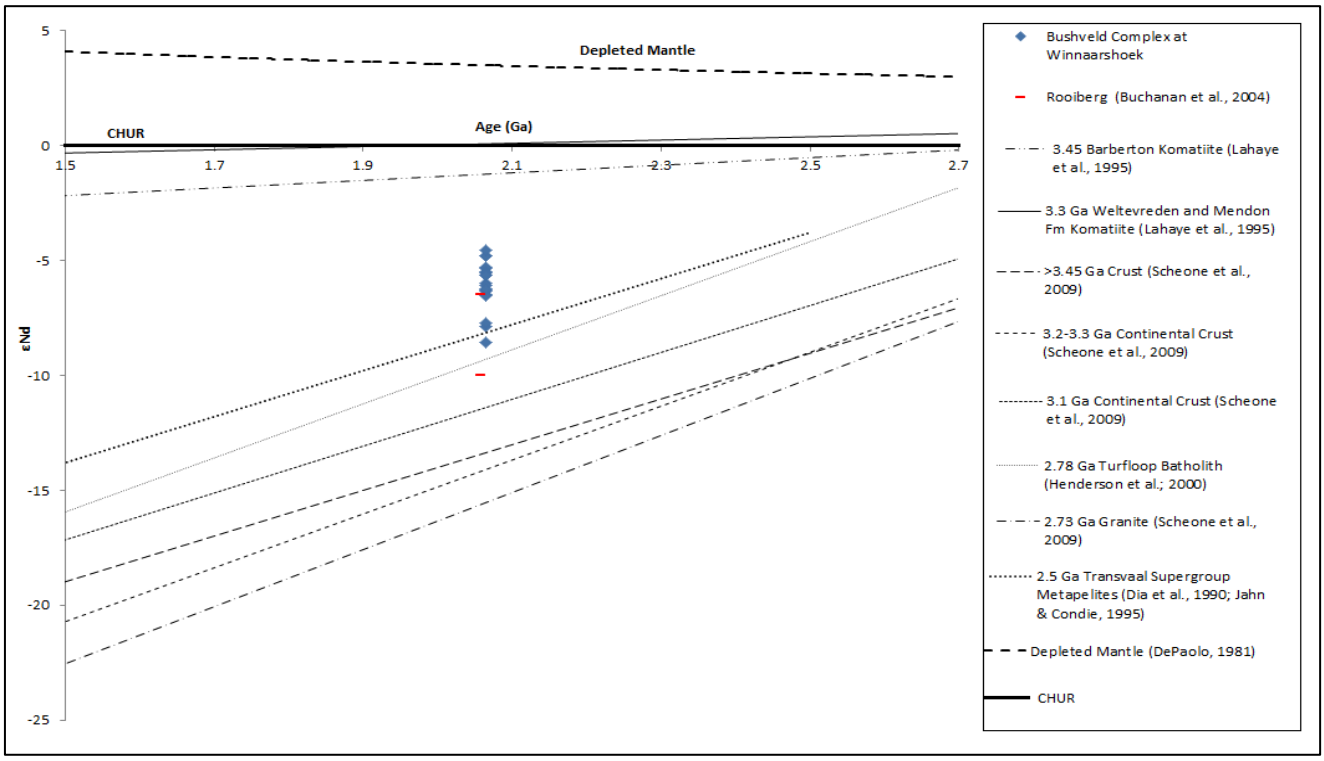

Figure 7.4 Possible magma reservoirs and country rock contaminants plotted against the ε_{Nd} values from the Merensky Reef at Winnaarshoek. Depleted mantle from DePaolo (1981); enriched mantle from Lahaye *et al.* (1995); Archaean and Neoarchaean TTGs and granites from Schoene *et al.* (2009) and Henderson *et al.* (2000); Transvaal metapelites from Dia *et al.* (1990) and Jahn and Condie (1995); Rooiberg Suite from Buchanon *et al.* (2004).

7.4.2 Contamination Model

A depleted mantle and a more enriched mantle (B2-"like" mantle) based on Barberton komatiites were chosen as potential parent magmas for the Merensky Cycle for modeling purposes. The starting composition of the depleted mantle at ca. 2.06 Ga is 2 ppm Nd corresponding to an initial ε_{Nd} value = +3.3 (DePaolo, 1981). The starting composition of the enriched B2-"like" magma based on Barberton komatiites is 6 ppm Nd corresponding to an initial ε_{Nd} value = -1 (Lahaye *et al.*, 1995). Two contaminants were chosen to model the effect of contamination on these parent magmas. The first contaminant was chosen as it represents the roof of the Bushveld Complex and the roof contamination models are the most commonly modeled for the formation of layered intrusions as a result of pluming (e.g. Campbell *et al.,* 1983; Kinnaird *et al.,* 2002; Kruger, 2005). The roof of the Bushveld Complex is the Rooiberg Group. The basal portion of the Rooiberg is represented by felsites of the Damwal and Dullstroom formations which have an average Nd concentration of 64 ppm, corresponding to an initial ε_{Nd} value = -8.6 (Buchanan *et al.*, 2004). Based on the heat capacity of the country rock and the enthalpy of fusion of the crystallizing cumulates, Taylor (1980) derived calculations limiting the amount of country rock that magmas could assimilate to about 30%. The Winnaarshoek samples lie in a field to the left of the mixing lines (Fig. 7.6 a&b) because they are essentially adcumulates with very little trapped liquid. The effects of fractional crystallization drag the composition to the left of the contaminated liquid mixing line (Fig. 7.5) because the partition coefficients for trace elements in the major rock forming minerals of cumulate rocks are a great deal less than 1 (e.g. $D^{Nd}<<1$). If the partition coefficient was equal or greater than 1, we would expect to see the bulk compositions of the samples plotting on or to the right of the mixing line.

Figure 7.6a shows the effect of the Rooiberg as a contaminant on the proposed parent magmas. As illustrated in Figure 7.6a; neither a depleted mantle source nor an enriched B2-"like" source could be sufficiently contaminated by the basal Rooiberg rocks to produce the maximum amount of contamination in the Winnaarshoek samples at 30% contamination. In fact, based on the mass balance calculations in Appendix D, both source magmas would require more than 90% contamination by the Rooiberg in order to produce the depletion seen at Winnaarshoek. The Rooiberg rocks may have contributed to the contamination; as some samples do fall within range of between 10 and 25% (for both depleted mantle and B2 modeled parents) contamination but it is very unlikely that assimilation of the Rooiberg alone could produce the required depletion. Figure 7.6b shows the effect of the Archaean TTGs as a contaminant on the proposed parent magmas. As

illustrated in Figure 7.6b; the Archaean TTGs could account for the bulk depletion seen at Winnaarshoek with less than 5% contamination of depleted mantle and between 5 and 10% for a B2-"like" parent magma. It would then only require 10% contamination of depleted mantle and ±15% contamination of a B2-"like" parent magma in order to reach the maximum depletion of ε_{Nd} = -8.5 at Winnaarshoek. It is therefore more likely that contamination of a depleted mantle or B2-"like' source by Archaean TTGs took place, than that of the Rooiberg. Subsequently, it is more likely that the source is depleted mantle as it is able to achieve the required peak contamination with lesser degrees of crustal contamination.

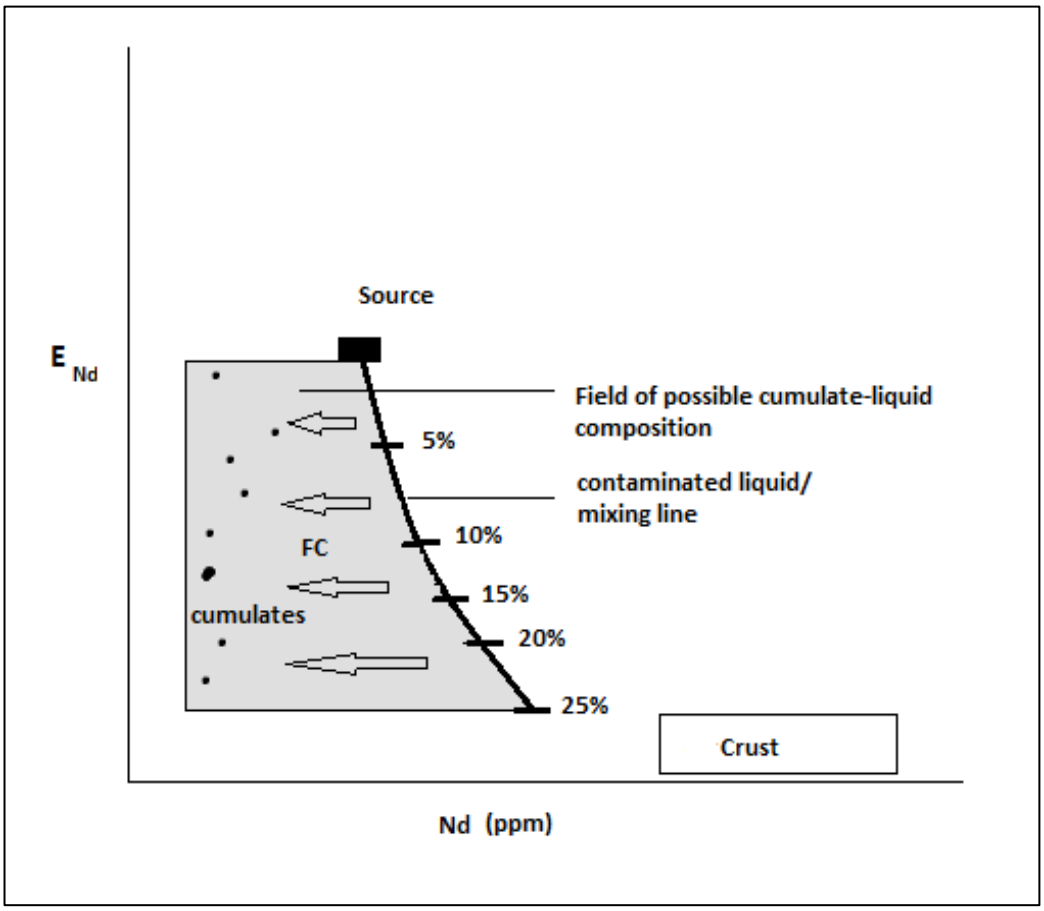

Figure 7.5 Schematic ε_{Nd} vs Nd diagram showing the effect of fractional crystallization and mixing on cumulate rock samples from Winnaarshoek. The samples bulk Nd composition plots in the field of possible cumulate-liquid composition to the left of the liquid mixing line because D^{Nd}<<1 for cumulus minerals undergoing fractional crystallization processes.FC= fractional crystallization.

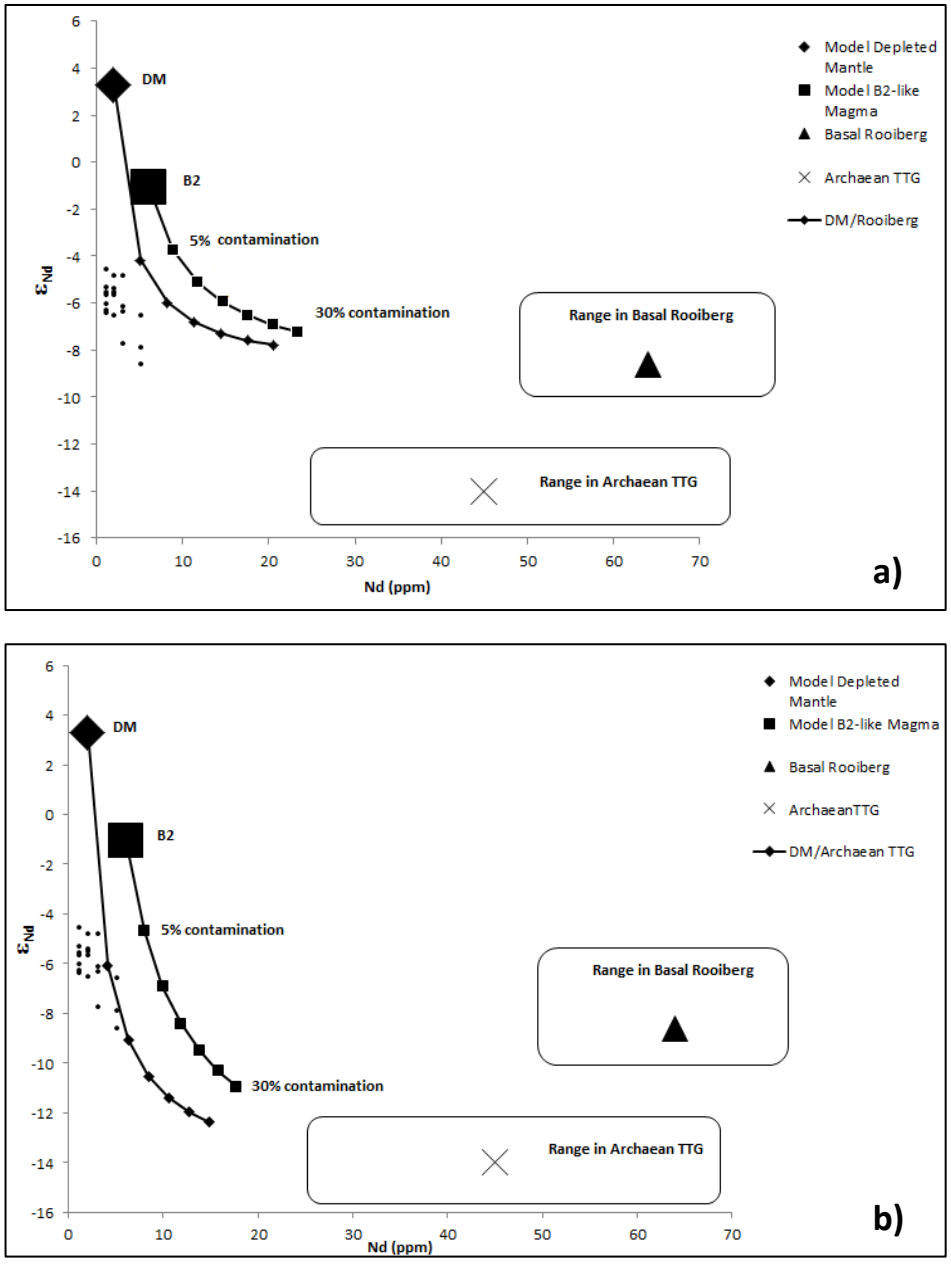

Figure 7.6 ε_{Nd} versus Nd concentration, demonstrating mixing of a) the basal Rooiberg felsites (c. 2.06 Ga; Buchanon *et al.,* 2004) and b) Archaean TTGs (3.1-3.45 Ga; Schoene *et al.*, 2009) with depleted mantle (DePaolo, 1981) and a B2-"like" komatiitic enriched mantle from Barberton (Lahaye *et al.,* 1995). Mixing lines are demarcated for every 5% of crustal contamination. Large symbols represent the modeled compositions for each of the contaminants (based on average) and source rocks e.g. diamond= Depleted Mantle (DM); square= B2-"like" magma; triangle= basal Rooiberg and; X= Archaean TTGs. Boxes represent the range of data for the basal Rooiberg and Archaean TTGs.

7.5 Implications for Genetic Models

Compositionally the hanging wall and footwall are quite similar so it is unlikely that the Reef was sandwiched between them as a result of the mixing of hanging wall and footwall magmas. The footwall does however; contain more olivine than the hanging wall which resulted in different crystallization sequences of plagioclase, olivine, orthopyroxene and clinopyroxene as mentioned in section 7.1.

The Reef has more affinity to the hanging wall than the footwall in terms of the crystallization sequence, in that the paragenetic sequence in the Reef is more similar to that of the hanging wall (i.e. early plagioclase, followed by orthopyroxene with consumption of olivine). Potentially, the Reef could then be representative of modified hanging wall supporting a model where a vertical settling process took place. If the reef showed affinity to the footwall, then an upwards-percolation model of magma or aqueous fluids would be supported. Compositionally the Reef does show some affinity to the footwall as orthopyroxene compositions in the Reef are more similar to those in the footwall than the hanging wall. If the Reef was distinct from either the hanging wall or footwall it would imply that the Reef was injected in laterally. This is supported by the isotopic "spike" found in the Reef in these samples. The problem here is that the Reef provides some evidence in support of all three of the scenarios mentioned above, which makes constraining a genetic model particularly problematic.

A few existing models are discussed as follows in relation to the outcomes of this study (Fig. 7.7). Figure 7.7a is a simple schematic diagram illustrating the upward migration of magmatic/hydrothermal fluids. Such a model has been proposed for the precipitation of PGEs in layered complexes by various authors (e.g. Nicholson & Mathez, 1991; Boudreau & McCallum, 1992; Boudreau, 2008). As the most primitive isotopic values of the hanging wall and footwall are within the same range, with the footwall being slightly more enriched, it is possible that and enriched fluid or melt may have percolated upwards and only partly re-equilibrated with the assemblage in the footwall. The texture of the reef pegmatoid is a result of extensive recrystallization and this coupled with an enriched, upward percolating fluid may have resulted in more extensive isotopic equilibration. Such a model is not considered in relation to observations made in this study because upwards-migrating magmatic fluids (as distinct from fluids derived from the country rocks underlying the complex) would not be expected to have a pronounced effect on the isotopic composition of the whole rock, specifically not in terms of creating an isotopic "spike" to the extent

as seen in this study and there is no solid evidence of the effects of an enriched fluid passing through the footwall. This may be attributed to the cessation of crystal aging resulting in slow re-equilibration.

A second model is the classic mixing model of Irvine (1977) where two compositionally different parent magmas known as U (ultramafic) and A (Al_2O_3) magmas are responsible for the crystallization of PGE-mineralized layered intrusions (Fig. 7.7b). Although this may account for an isotopic shift (i.e. a change across the Reef from one isotopic composition below to a different one above) as a result of mixing (e.g. Kruger & Marsh, 1985; Naldrett *et al.,* 1987), it is not expected to create an isotopic spike in a particular portion of the intrusion (e.g. the Merensky Reef) and not elsewhere. Other authors prefer a model where pluming of the incoming magma causes contamination by assimilating rocks associated with the roof of the intrusion, in this case the basal Rooiberg Group (Kinnaird *et al.,* 2002; Kruger, 2005) prior to lateral emplacement of the Reef as a density current (Fig. 7.7c). As previously shown in this study (section 7.4) it is virtually impossible for the assimilation of the basal Rooiberg group alone to cause the peak of contamination documented herein, in the Merensky Reef.

The results of this study therefor favour a model whereby a mantle-derived plume allowed for the ascension of magma which assimilated crust prior to emplacement (e.g. Maier *et al.,* 2000; Harris *et al.,* 2005). This model would allow for crustal contamination and the precipitation of PGEs to occur prior to emplacement (Fig. 7.7d). Emplacement would then occur as a lateral sill where slumping and cumulate unmixing occurs which could result in the formation of chromite- and sulphide-rich pyroxenites, as well as sorting of cumulus layers, as outlined by Maier *et al.* (2013). Results in this study favour this model because firstly there is an isotopic "spike" in the Reef. This could be explained by contamination prior to emplacement. This is supported in section 7.4, where it was shown that contamination of a depleted mantle or B2-"like" parent by lower crustal components would be able to achieve the "spike" in ε_{Nd} values documented. The fact that depleted mantle or a komatiitic magma was successfully modeled with old crust is further evidence of the presence of a mantle plume as a mechanism to generate the required heat and energy to create melting and ascension of magma. Secondly, mineral separate data obtained herein (Chapter 6), suggests that coexisting plagioclase and orthopyroxene in the Reef are in equilibrium. This is possible if they were derived from the same isotopic reservoir prior to emplacement. The premise that the Reef was then injected in as a lateral sill is further supported by this mineral equilibrium in the Reef because

coexisting plagioclase and orthopyroxene in the hanging wall and footwall units have been shown to be in disequilibrium with one another. This indicates that they underwent separate processes to that of the Reef, supporting the possibility of the Reef being derived from a distinct emplacement event. The affinity of the Reef to the footwall in terms of the similarities in composition between orthopyroxene in the Reef and hangingwall could then be explained by a crystal settling process. Orthopyroxene from the Reef would move downwards through the crystal mush due to gravity settling into the partially crystallized footwall magma below. This would partly account for the different textures and disequilibrium features evident in the footwall. This concept is similar to that of Seabrook *et al.* (2005) who explained the presence of Main Zone plagioclase compositions found in the Critical Zone by a similar process. As mentioned earlier the reef and hanging wall have similar crystallization sequences. This could imply that they were part of the same magma but it is more likely that that they were separate magmas, both of which lacked olivine, and which just followed similar crystallization sequences. The implications based on the observations made and data acquired in this study could indicate that multiple magmas were required to produce the Reef, the hanging wall and the footwall units.

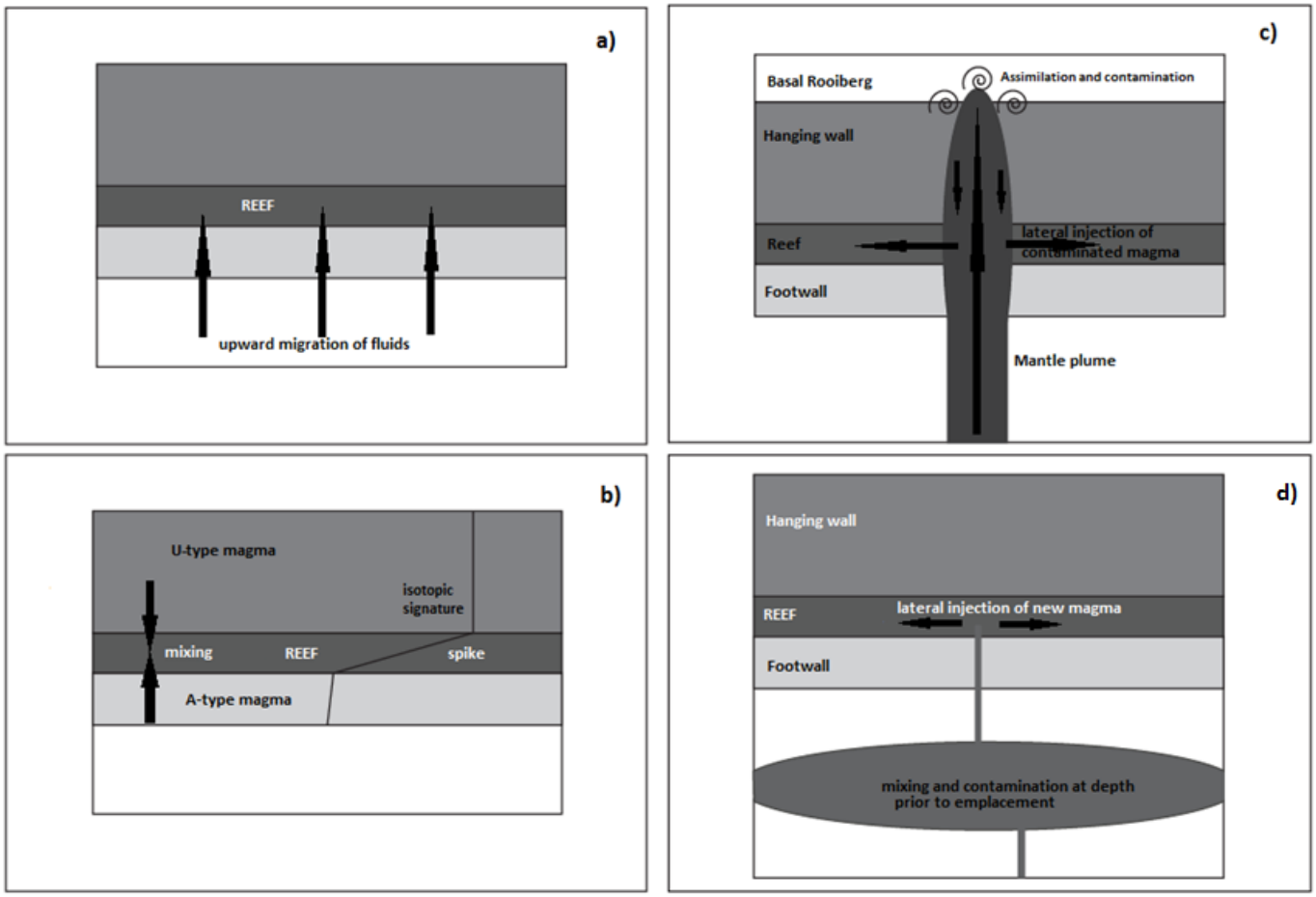

Figure 7.7 Schematic diagrams representing some postulated models for the Merensky reef. a) Upwards percolation of magmatic fluids responsible for the precipitation of PGEs, but not expected to change the isotopic composition. b) Classic magma mixing of A- and U- type magmas to create the Reef and precipitate PGEs and Chromite. This model could cause a shift in the isotopic composition but is not expected to create the "spike" documented in this study. c) Proposed model of a mantle-derived plume assimilating rocks of the basal Rooiberg roof before the Reef is injected in laterally. Although a popular model, it has been shown in this study that contamination of the Rooiberg alone could not produce the extent of contamination documented in this study. d) The proposed model of contamination and precipitation of PGEs and chromite prior to the emplacement of the Merensky Reef as a lateral sill following melting by a mantle plume which causes magma ascension and contamination by lower crust.

Summary and Conclusions

Mineral disequilibrium in the Merensky Reef at Winnaarshoek in the eastern Bushveld Complex is present as disequilibrium textures among coexisting orthopyroxene, plagioclase and clinopyroxene in the hanging wall, Reef and footwall units. Disequilibrium is also present in the mineral compositions of these same minerals throughout the sampled sequence. A third incidence of mineral disequilibrium in the sampled sequence is that of Sm-Nd isotopic compositions in not only whole-rock samples but also coexisting plagioclase and orthopyroxene. The Sm-Nd isotopic system was preferentially chosen over the Rb-Sr isotopic system because firstly, Nd tells us about plagioclase and both pyroxenes (clino- and orthopyroxene), while Sr only really tells us about plagioclase. Secondly, Nd is less affected by hydrothermal or late magmatic fluids; and thirdly, the Sm-Nd database for the Merensky Reef (and to an extent the Bushveld Complex as a whole) is very limited in comparison to the Rb-Sr database.

From the disequilibrium features mentioned above it was possible to derive a mineral crystallization sequence in which plagioclase crystallization precedes that of orthopyroxene crystallization followed by late clinopyroxene crystallization. In some instances, olivine crystallization takes place after early plagioclase and then is consumed to produce orthopyroxene. From this it was deduced that multiple magmas were responsible for the Merensky Reef and its hanging wall and footwall units. Textural evidence such as resorbed plagioclase grains within orthopyroxene and/or olivine; resorbed orthopyroxene in clinopyroxene and orthopyroxene with discontinuous clinopyroxene rims were used (among others) to infer the crystallization sequence in context with the observed changes in corresponding mineral compositions.

Sm-Nd isotopic disequilibrium was used to further illustrate that the Merensky Reef is a distinct unit from its hanging wall and footwall and was done so by illustrating a peak of ε_{Nd} contamination in the reef itself of ε_{Nd}= -8.5.The Sm-Nd isotopic system was also used to constrain the contamination process responsible for the "spike" in ε_{Nd} values. The contamination was modeled using simple mass balance mixing calculations which showed that the peak in ε_{Nd} values in the Reef could be achieved by a depleted mantle or B2-"like" source (originating from mantle pluming) assimilating old, lower crust such as Archaean TTGs. The required contamination is between 5 and 10% of this old, lower crust.

The textural, geochemical and isotopic evidence presented thus far was used to constrain a model for the genesis of the Merensky Reef. The model postulates that a mantle-derived magma as a consequence of pluming rose through the crust assimilating old, lower crust. Contamination and precipitation of PGEs and chromite then took place prior to the lateral emplacement of the Reef as a density current. The implications of this are that several magmas and magmatic processes are responsible for the emplacement of the Merensky Reef and its footwall and hanging wall units, each with distinct emplacement and contamination mechanisms.

References

Anderson, O. (1915). The system anorthite-forsterite-silica. *American Journal of Science, 4th Series, 39*, 407-454.

Ashwal, L. D., Wiebe, R. A., Wooden, L. J., & Whitehouse, M. J. (1992). The role of crustal contamination in the petrogenesis of anorthosites: isotopic evidence. *Abstracts, Third Meeting, I.C.G.P. Project No.209, Anorthosite and related Rocks*, (pp. 1-3). Moi, Norway.

Bedard, J. H. (1994). A procedure for calculating the equilibrium distribution of trace elements among the minerals of cumulate rocks, and the concentration of trace elements in the coexisting liquids. *Chemical Geology, 118*, 143-153.

Boorman, S., Boudreau, A. E., & Kruger, F. J. (2004). The lower zone-critical zone transistion of the Bushveld Complex: a quantitive textural study. *Journal of Petrology, 45*(6), 1209-1235.

Boudreau, A. E. (2008). Modelling the Merensky Reef, Bushveld Complex, Rebublic of South Africa. *Contributions to Mineralogy and Petrology, 156*, 431-437.

Boudreau, A. E., & McCallum, I. S. (1992). Concentration of platinum-group elements by magmatic fluids in layered intrusions. *Economic Geology, 87*, 1830-1848.

Brynard, H. J., De Villiers, J. P., & Viljoen, E. A. (1976, November). A Mineralogical Investigation of the Merensky Reef at the Western Platinum Mine, near Marikana, South Africa. *Economic Geology, 71*, pp. 1299-1307.

Buchanon, P. C., Reimold, W. U., Koeberl, C., & F J, K. (2002). Geochemistry of intermediate to siliceous volcanic rocks of the Rooiberg Group, Bushveld Magmatic Province, South Africa. *Contributions to Mineral Petrography, 144*, 131-143.

Buchanon, P. C., Reimold, W. U., Koeberl, C., & Kruger, F. J. (2004). Rb–Sr and Sm–Nd isotopic compositions of the Rooiberg Group, South Africa: early Bushveld-related volcanism. *Lithos, 29*, 373-388.

Buchanan, D. L., Nolan, J., Suddaby, P., J E, R., Viljoen, M. J., & Davenport, W. J. (1981). The genesis of sulphide mineralization in a portion of the Potgietersrus Limb of the Bushveld Complex. *Economic Geology, 76*, 568-579.

Buick, I. S., Maas, R., & Gibson, R. (2001). Precise U-Pb titanite age constraints on the emplacement of the Bushveld Complex, South Africa. *Journal of the Geological Society, 158*, 3-6.

Cameron, E. N. (1978). The Lower Zone of the eastern Bushveld Complex in the Olifants River Trough. *Journal of Petrology, 75*, 845-871.

Cameron, E. N. (1982). Upper Critical Zone, Eastern Bushveld Complex. *Economic Geology, 77*(6), pp. 1307-1327.

Campbell, I. H., & Murck, B. W. (1993). Petrology of the G chromitite zones in the Mountain View area of the Stillwater Complex. *Journal of Petrology, 34*, 291-316.

Campbell, I. H., Naldrett, A. J., & Barnes, S. J. (1983). A model for the origin of the platinum-rich sulfide horizons in the Bushveld and Stillwater Complexes. *Journal of Petrology, 24*, 133-165.

Capobianco, C. J., Hervig, R. L., & Drake, M. J. (1994). Experiments on crystal/liquid partitioning of Ru, Rh and Pd into magnetite and hematite solid solutions crystallized from silicate melts. *Chemical Geology, 113*, 23-43.

Cawthorn, R. G. (1999a). Permeability of the footwall cumulates to the Merensky Reef, Bushveld Complex. *South African Journal of Geology, 102*, 293-302.

Cawthorn, R. G. (1999b). Platinum-group element mineralization in the Bushveld Complex- a critical reassessment of geochemical models. *South African Journal of Geology, 102*(3), 268-281.

Cawthorn, R. G. (2010). Geological interpretations from the PGE distribution in the Bushveld Merensky and UG2 chromitite reefs. *The 4th International Platinum Conference, Platinum in transition 'Boom or Bust'* (pp. 57-69). The Southern African Institute of Mining and Metallurgy.

Cawthorn, R. G., Davies, G., Clubley-Armstrong, A., & McCarthy, T. S. (1981). Sills associated with the Bushveld Complex, South Africa: an estimate of the parental magma composition. *Lithos, 14*, 1-15.

Cawthorn, R. G., & Boerst, K. (2006). Origin of the Pegmatitic Pyroxenite in the Merensky Unit, Bushveld Complex, South Africa. *Journal of Petrology, 47*(8), 1509-1530.

Chutas, N. I., Bates, E., Prevec, S. A., Coleman, D. S., & Boudreau, A. E. (2012). Sr and Pb isotopic disequilibrium between coexisting plagioclase and orthopyroxene in the Bushveld Complex, South Africa: microdrilling and progressive leaching evidence for sub-liquidus contamination within a crystal mush. *Contributions to Mineralogy and Petrology, 163*, 653-668.

Couch, S., Sparks, R. S., & Carroll, M. R. (2001). Mineral disequilibrium in lavas explained by convective self-mixing in open magma chambers. *Nature, 411*(6841), 1037-1039.

Davies, G., & Cawthorn, R. G. (1984). Mineralogical data on a multiple intrusion in The Rustenburg Layered Suite of the Bushveld Complex. *Mineralogical Magazine, 48*, 469-480.

DePaolo, D. J. (1981). Neodymium isotopes in the Colorade Front Range and crust-mantle evolution in the Proterozoic. *Nature, 291*, 193-196.

Dia, A., Allegre, C. J., & Erlank, A. J. (1990). The development of continental crust through geological time: the South African case. *Earth and Planetary Science Letters, 98*, 74-89.

Eales, H. V. (2000). Implications of the chromium budget of the Western Limb of the Bushveld Complex. *South African Journal of Geology, 103*, 141-150.

Eales, H. V. (2001). *A first introduction to the geology of the Bushveld Complex and those aspects of South African geology that relate to it.* Pretoria: Council for Geoscience, Geological Survey of South Africa.

Eales, H. V., & Cawthorn, R. G. (1996). The Bushveld Complex. In R. G. Cawthorn (Ed.), *Layered Intrusions* (pp. 181-229). Amsterdam: Elsevier.

Eales, H. V., & Costin, G. (2012). Crustally Contaminated Komatiite: Primary Source of the Chromitites and Marginal, Lower, and Critical Zone Magmas in a staging Chamber Beneath the Bushveld Complex. *Economic Geology, 107*, 645-665.

Eales, H. V., de Klerk, W. J., & Teigler, B. (1990). Evidence for magma mixing processes within the Critical and Lower Zones of the northwestern Bushveld Complex, South Africa. *Chemical Geology, 88*, 261-278.

Engelbrecht, J. P. (1985). The chromitites of the Bushveld Complex in the Nietverdiend area. *Economic Geology, 80*, 896-910.

Frost, C. D., & Frost, B. R. (2011). On ferroan (A-type) granitoids: their compositional variability and modes of origin. *Journal of Petrology, 52*, 39-53.

Harmer, R. E., & Sharpe, M. R. (1985). Field relations and strontium isotope systematics of the marginal rocks of the eastern Bushveld Complex. *Economic Geology, 80*, 813-837.

Harris, C., & Chaumba, J. B. (2001). Crustal contamination and fluid-rock interaction during the formation of the Platreef, northern limb of the Bushveld Complex, South Africa. *Journal of Petrography, 42*(7), 1321-1347.

Harris, C., Pronost, J. J., Ashwal, L. D., & Cawthorn, R. G. (2005). Oxygen and hydrogen isotope stratigraphy of the Rustenburg Layered Suite, Bushveld Complex: constraints on crustal contamination. *Journal of Petrology, 46*(3), 579-601.

Hatton, C. J. (1995). Mantle plume origin for the Bushveld and Ventersdorp magmatic provinces. *Journal of African Earth Sciences, 21*, 571-577.

Hatton, C. J., & Schweitzer, J. K. (1995). Evidence for synchronous extrusive and intrusive Bushveld magmatism. *Journal of African Earth Sciences, 21*, 579-594.

Henderson, D. R., Long, L., & Barton, J. M. (2000). Isotopic ages and chemical and isotopic composition of the Archaean Turfloop Batholith, Pietersburg granite-greenstone terrane, Kaapvaal Craton, South Africa. *South African Journal of Geology, 103*(1), 38-46.

Hill, M., Barker, F., Hunter, D., & Knight, R. (1996). Geochemical characteristics and origin of the Lebowa Granite Suite, Bushveld Complex. *International Geology Review, 38*, 195-227.

Hulbert, L. J., & von Gruenewaldt, G. (1985). Textural and compositional features of chromite in the Lower and Critical Zones of the Bushveld Complex south of Potgietersrus. *economic Geology, 80*, 872-895.

Irvine, T. N. (1977). Origin of chromitite in the Muskox intrusion and other stratiform intrusions: a new interpretation. *Geology, 5*, 273-277.

Irvine, T. N., Keith, D. W., & Todd, S. G. (1983). The J-M Platinum-Palladium Reef of the Stillwater Complex, Montana. *Economic Geology, 78*, 1287-1334.

Jacobsen, S.B. & Wasserburg, G.J. (1980) Sm–Nd evolution of chondrites. *Earth and Planetary Science Letters, 50*, 139–155.

Jahn, B., & Condie, K. C. (1995). Evolution of the Kaapvaal Craton as viewed from geochemical and Sm-Nd isotopic analyses of intracratonic pelites. *Geochimica et Cosmochirnica Acta, 59*(11), 2239-2258.

Kinnaird, J. A., Hutchinson, D., Schurmann, L., Nex, P. A., & de Lange, R. (2005). Petrology and mineralization of the southern Platreef: northen limb of the Bushveld Complex, South Africa. *Mineral Deposita, 40*, 576-597.

Kinnaird, J. A., Kruger, F. J., Nex, P. A., & Cawthorn, R. G. (2002). Chromite formation – a key to understanding processes of platinum enrichment. *Transactions Institute Mining Metallurgy, 111*, B23-B35.

Kruger, F. J. (1990). The stratigraphy of the Bushveld Complex: a reappraisal of the Main Zone boundaries. *S. Afr. J> Geol., 93*, 376-381.

Kruger, F. J. (2005). Filling the Bushveld Complex magma chamber: lateral expansion, roof and floor interaction, magmatic unconformities, and the formation of giant chromitite, PGE and Ti-V-magnetitite deposits. *Mineralium Deposita, 40*, 451-472.

Kruger, F. J., & Marsh, J. S. (1982). Significance of 87Sr/86Sr ratios in the Merensky Cyclic Unit of the Bushveld Complex. *Nature, 298*, 53-55.

Kruger, F. J., & Marsh, S. J. (1985). The mineralogy, petrology and origin of the Merensky Cyclic Unit of the Bushveld Complex. *Economic Geology, 80*, 958-974.

Lahaye, Y., Arndt, N., Byerly, G., Chauvel, C., Fourcade, S., & Gruau, G. (1995). The influence of alteration on the trace-element and Nd isotopic compositions of komatiites. *Chemical Geology, 126*, 43-64.

Lee, C. A. (1996). A Review of Mineralisation in the Bushveld Complex and some other Layered Intrusions. In R. Cawthorn, & R. Cawthorn (Ed.), *Layered Intrusions* (pp. 103-146). Amsterdam: Elsevier.

Lee, C. A., & Butcher, A. R. (1990). Cyclicity in the Sr isotope stratigraphy through the Merensky and Bastard Reef Units, Atok Section,eastern Bushveld Complex. *Economic Geology, 85*, 877-883.

Lipin, B. R. (1993). Pressure increases, the formation of chromite seams, and the development of the Ultramafic Series in the Stillwater Complex, Montana. *Journal of Petrology, 34*, 955-976.

Maier, W. D. (1991). Geochemical and Petrological trends in the UG2-Merensky Unit interval of the Upper Critical Zone in the Western Bushveld Complex. *PHD Thesis- Rhodes University*, 1-354.

Maier, W. D., Arndt, N. T., & Curl, E. A. (2000). Progressive crustal contamination of the Bushveld Complex: Evidence from Nd isotopic analyses of the cumulate rocks. *Contributions to Mineralogy and Petrology, 140*, 316-327.

Maier, W. D., Barnes, S.-J., & Groves, D. I. (2013). The Bushveld Complex, South Africa: formation of platinum–palladium, chrome- and vanadium-rich layers via hydrodynamic sorting of a mobilized cumulate slurry in a large, relatively slowly cooling, subsiding magma chamber. *Mineralium Deposita, 48*(1), 1-56.

Mathez, E. A. (1995). Magmatic metasomatism and formation of the Merensky reef, Bushveld Complex. *Contributions to Mineralogy and Petrology, 119*, 277-286.

Mathez, E. A., Van Tongeren, J. A., & Schweitzer, J. (2013). On the relationships between the Bushveld Complex and its felsic roof rocks, part 1: petrogenesis of Rooiberg and related felsites. *Contributions to Mineral Petrology, 166*, 435-449.

McLaren, C. H., & De Villiers, J. P. (1982). The platinum-group chemistry and mineralogy of the UG2 chromitite layers of the Bushveld Complex. *Economic Geology, 77*, 1348-1366.

Mitchell, A. A. (1990). The stratigraphy, petrography and mineralogy of the Main Zone of the Northwestern Bushveld. *South African Journal of Geology, 93*, 818-831.

Mitchell, A. A., & Scoon, R. N. (2007). The Merensky Reef at Winnaarshoek, Eastern Bushveld Complex: A primary magmatic hypothesis based on a wide reef facies. *Economic Geology, 102*, 971-1009.

Molyneux, T. G. (1974). A geological investigation of the Bushveld Complex in Sehukhuneland and part of the Steelpoort Valley. *Transactions of the Geological Society of South Africa, 77*, 329-338.

Mondal, S. K., & Mathez, E. A. (2007). Origin of the UG2 chromitite layer, Bushveld Complex. *Journal of Petrology, 48*(3), 495-510.

Murck, B. W., & Campbell, I. H. (1986). The effects of temperature, oxygen fugacity and melt composition on the behaviour of chromium in basic and ultrabasic melts. *Geochimica et Cosmochimica Acta, 50*, 1871–1888.

Naldrett, A. J. (1989). Stratiform PGE deposits in layered intrusions. *Reviews in Economic Geology, 4*, 135-166.

Naldrett, A. J., Cameron, G., von Grunewaldt, G., & Sharpe, M. R. (1987). The formation of stratiform PGE deposits in layered intrusions. In I. (. Parsons, *Origins of Igneous Layering* (pp. 313-397). Dordrecht: Reidel.

Nicholson, D. M., & Mathez, E. A. (1991). Petrogenesis of the Merensky Reef in the Rustenburg section of the Bushveld Complex. *Contributions to Mineralogy and Petrology, 107*, 293-309.

Prevec, S. A., Ashwal, L. D., & Mkaza, M. S. (2005). Mineral disequilibrium in the Merensky Reef, western Bushveld Complex, South Africa: new Sm-Nd isotopic evidence. *Contributions to Mineral Petrology, 149*, 306-315.

Schiffries, C. M., & Rye, D. M. (1989). Stable isotope systematics of the Bushveld Complex: Constraints of magmatic processes in layered intrusions. *american Journal of Science, 289*, 841-873.

Schoene, B., Dudas, F. O., Bowring, S. A., & de Wit, M. (2009). Sm–Nd isotopic mapping of lithospheric growth and stabilization in the eastern Kaapvaal craton. *Terra Nova, 21*, 219-228.

Schweitzer, J. K., & Hatton, C. J. (1995). Chemical alteration within the volcanic roof rocks of the Bushveld Complex. *Economic Geology, 90*, 2218-2231.

Scoon, R. N., & Teigler, B. (1994). Platinum-group element mineralization in the Critical Zone of the western Bushveld Complex:1. Sulphide-poor chromitites below the UG2. *Economic Geology, 89*, 1094-1121.

Seabrook, C. L., Cawthorn, R. G., & Kruger, F. J. (2005). The Merensky Reef, Bushveld Complex: Mixing of minerals not mixing of magmas. *Economic Geology, 100*, 1191-1206.

Sharpe, M. R. (1981). The chronology of magma influxes to the eastern compartment of the Bushveld Complex as exemplified by its marginal border groups. *Journal of the Geological Society of London, 138*, 307-326.

Sharpe, M. R. (1985). Strontium isotope evidence for preserved density stratification in the Main Zone of the Bushveld Complex, South Africa. *Nature, 316*, 119-126.

Stratigraphy), S. (. (1980). *Stratigraphy of South Africa* (8 ed.). (L. Kent, Ed.) Pretoria: Geological Survey of South Africa.

Tanaka, T., Togashi, S., Kamioka, H., Amakawa, H., Kagami, H., Hamamoto, T., et al. (2000). JNdi-1: a neodymium isotopic reference in consistency with Lajolla neodymium. *Chemical Geology, 168*, 279-281.

Taylor Jr, H. P. (1980). The effects of assimilation of country rocks by magmas on 18O/16O and 87Sr/86Sr systematics in igneous rocks. *Earth and Planetary Science Letters, 47*, 243-254.

Teigler, B., Eales, H. V., & Scoon, R. N. (1992). The cumulate succession in the Critical Zone of the Rustenburg Layered Suite at Brits, western Bushveld Complex. *South African Journal of Geology, 95*, 17-28.

Twist, D., & French, B. M. (1983). Voluminous acid volcanism in the Bushveld Complex: a review of the Rooiberg Felsite. *Bulletin of Volcanism, 46*, 225-242.

Vermaak, C. F. (1976). The Merensky Reef-thoughts on its environment and genesis. *Economic Geology, 71*, 1270-1298.

Vermaak, C. F., & von Gruenewaldt, G. (1986). Introduction to the Bushveld Complex. In C. R. Anhaeusser, & S. Maske (Eds.), *Mineral Deposits of Southern Africa* (Vol. 2, pp. 1021-1029). Geol. Soc. South Africa.

Viljoen, M. J. (1999). The nature and origin of the Merensky Reef of the western Bushveld Complex based on geological facies and geophysical data. *South African Journal of Geology, 25*(3), 208-221.

Viljoen, M. J., & Schurmann, L. W. (1998). Platinum- Group Metals. In M. Wilson, & C. Anhaeusser, *The Mineral Resources of South Africa* (pp. 532-568). Pretoria: Council for Geosciences.

von Gruenewaldt, G. (1973). The Main and Upper Zones of the Bushveld Complex in the Roossenakel area, eastern Transvaal. *Transactions of the Geological Society of South Africa, 76*, 207-227.

von Gruenewaldt, G., Sharpe, M. R., & and Hatton, C. J. (1985, June-July). The Bushveld Complex: Introduction and Review. *Economic Geology, 80*(4), pp. 803-812.

Walraven, F. J. (1985). Genetic-aspects of the granophyric rocks of the Bushveld Complex. *Economic Geology, 80*, 1166-1180.

Walraven, F. J. (1987). Textural, geochemical, and genetic aspects of the granophyric rocks of the Bushveld Complex. *Geological Survey of South Africa Memorandum 72*.

Walraven, F. J. (1997). Geochronology of the Rooiberg Group, Transvaal Supergroup, South Africa. *Economic Geology Research Unit, University of Witwatersrand Information Circular, 316*.

Walraven, F. J., & Hattingh, P. J. (1993). Geochronology of the Nebo Granite, Bushveld Complex. *South African Journal of Geology, 96*, 31-41.

Appendix A- Orthopyroxene compositions (EPMA) from the Merensky Reef at Winnaarshoek

Table A1 Orthopyroxene compositions from the hanging wall anorthosite, Merensky Reef, Winnaarshoek.

Depth (m)	182	182	188.8	188.8	188.8	188.8	188.8
Sample	WH31_01_4	WH31_01_8	WH31_03_13	WH31_03_14	WH31_03_15	WH31_03_16	WH31_03_17
SiO2	56.76	54.22	54.40	54.57	54.55	53.70	53.25
TiO2	0.10	0.15	0.16	0.23	0.17	0.21	0.05
Al2O3	1.19	1.41	1.24	1.13	1.21	1.01	3.52
Cr2O3	0.34	0.43	0.33	0.06	0.28	0.06	0.42
Fe2O3	0.00	2.20	0.52	0.38	0.57	0.99	0.00
FeO	10.22	9.24	14.62	14.69	15.03	14.31	9.95
MnO	0.28	0.24	0.28	0.33	0.32	0.36	0.08
NiO	0.00	0.00	0.00	0.00	0.00	0.00	0.00
MgO	30.26	29.24	27.08	27.86	27.42	27.35	22.84
CaO	1.11	2.53	1.59	0.60	0.90	0.75	2.69
Na2O	0.00	0.03	0.00	0.00	0.00	0.00	0.04
Total	100.25	99.69	100.20	99.84	100.45	98.74	92.83
Si	1.99	1.94	1.96	1.97	1.96	1.96	2.01
Ti	0.00	0.00	0.00	0.01	0.00	0.01	0.00
Al	0.05	0.06	0.05	0.05	0.05	0.04	0.16
Cr	0.01	0.01	0.01	0.00	0.01	0.00	0.01
Fe	0.30	0.34	0.45	0.45	0.47	0.46	0.31
Mn	0.01	0.01	0.01	0.01	0.01	0.01	0.00
Ni	0.00	0.00	0.00	0.00	0.00	0.00	0.00
Mg	1.58	1.56	1.45	1.50	1.47	1.49	1.29
Ca	0.04	0.10	0.06	0.02	0.03	0.03	0.11
Na	0.00	0.00	0.00	0.00	0.00	0.00	0.00
Total	3.98	4.02	4.00	4.00	4.01	4.01	3.90
Mg#	84	82	76	77	76	76	80
Wo	2	5	3	1	2	1	6
En	82	78	74	75	74	75	75
Fs	16	17	23	23	24	24	19

Table A2 Orthopyroxene compositions from the hanging wall leuconorite, Merensky Reef, Winnaarshoek.

Depth (m)	190.8	190.8	190.8	190.8	190.8	190.8	191.5
Sample	WH31_04_20	WH31_04_24	WH31_04_25	WH31_04_26	WH31_04_27	WH31_04_28	WH31_05_30
SiO2	54.36	53.91	53.96	53.96	54.11	54.23	55.33
TiO2	0.09	0.17	0.12	0.17	0.16	0.14	0.15
Al2O3	1.57	1.55	1.80	1.54	1.49	1.38	1.52
Cr2O3	0.49	0.51	0.43	0.52	0.49	0.47	0.49
Fe2O3	0.00	0.00	0.00	0.00	0.00	0.00	0.00
FeO	13.80	14.52	15.17	14.95	14.92	15.17	14.60
MnO	0.30	0.31	0.25	0.32	0.34	0.43	0.36
NiO	0.00	0.00	0.00	0.00	0.00	0.00	0.00
MgO	26.18	26.30	26.16	27.04	26.89	26.82	28.09
CaO	2.49	2.00	0.85	0.59	0.72	0.73	0.72
Na2O	0.02	0.04	0.00	0.00	0.00	0.00	0.00
Total	99.31	99.31	98.75	99.08	99.11	99.37	101.25
Si	1.97	1.96	1.97	1.96	1.96	1.97	1.96
Ti	0.00	0.00	0.00	0.00	0.00	0.00	0.00
Al	0.07	0.07	0.08	0.07	0.06	0.06	0.06
Cr	0.01	0.01	0.01	0.02	0.01	0.01	0.01
Fe	0.42	0.44	0.46	0.45	0.45	0.46	0.43
Mn	0.01	0.01	0.01	0.01	0.01	0.01	0.01
Ni	0.00	0.00	0.00	0.00	0.00	0.00	0.00
Mg	1.41	1.42	1.42	1.46	1.45	1.45	1.48
Ca	0.10	0.08	0.03	0.02	0.03	0.03	0.03
Na	0.00	0.00	0.00	0.00	0.00	0.00	0.00
total	3.99	4.00	3.98	4.00	3.99	3.99	4.00
Mg#	77	76	75	76	76	76	77
Wo	5	4	2	1	1	1	1
En	73	73	74	75	75	74	76
Fs	22	23	24	24	24	24	23

Table A2 Continued, Orthopyroxene compositions from the hanging wall leuconorite, Merensky Reef, Winnaarshoek.

191.5	191.5	191.5	191.5	191.5	191.5	191.5
WH31_05_31	WH31_05_32	WH31_05_105	WH31_05_106	WH31_05_107	WH31_05_112	WH31_05_113
54.13	54.04	54.73	54.00	54.61	54.57	54.19
0.13	0.11	0.15	0.19	0.16	0.21	0.18
1.51	1.42	1.37	1.57	1.38	1.30	1.37
0.08	0.46	0.40	0.48	0.44	0.45	0.09
0.00	0.00	0.00	0.00	0.00	0.00	0.00
16.10	15.37	13.67	11.23	12.36	13.40	13.58
0.34	0.34	0.28	0.21	0.29	0.27	0.29
0.00	0.00	0.00	0.00	0.00	0.00	0.00
26.50	26.66	27.93	25.75	27.64	28.13	27.49
0.89	0.74	0.84	5.01	0.75	0.57	0.68
0.00	0.00	0.00	0.00	0.00	0.03	0.04
99.67	99.15	99.38	98.44	97.62	98.92	97.92
1.96	1.97	1.97	1.96	1.99	1.97	1.98
0.00	0.00	0.00	0.01	0.00	0.01	0.01
0.06	0.06	0.06	0.07	0.06	0.06	0.06
0.00	0.01	0.01	0.01	0.01	0.01	0.00
0.49	0.47	0.41	0.34	0.38	0.40	0.41
0.01	0.01	0.01	0.01	0.01	0.01	0.01
0.00	0.00	0.00	0.00	0.00	0.00	0.00
1.43	1.45	1.50	1.40	1.50	1.51	1.49
0.03	0.03	0.03	0.20	0.03	0.02	0.03
0.00	0.00	0.00	0.00	0.00	0.00	0.00
4.00	3.99	3.99	3.99	3.97	3.99	3.99
75	76	78	80	80	79	78
2	1	2	10	2	1	1
73	74	77	72	78	78	77
25	24	22	18	20	21	22

Table A3 Orthopyroxene compositions from the Reef pyroxenite, Merensky Reef, Winnaarshoek.

Depth (m)	192.1	192.1	192.1	192.1	192.1	192.1	192.1	192.1	192.1	192.1	192.1	192.1	192.1
Sample	R1-opx-1	R1-opx-2	R1-opx-3	R1-opx-4	R1-opx-5	R1-opx-6	R1-opx-7	R1-opx-8	R1-opx-9	R1-opx-10	R1-opx-11	R1-opx-12	R1-opx-13
SiO2	55.79	55.70	54.85	55.84	55.62	55.42	55.39	55.39	55.59	54.91	56.19	55.16	55.52
TiO2	0.14	0.17	0.16	0.13	0.19	0.12	0.02	0.13	0.16	0.26	0.15	0.23	0.20
Al2O3	1.23	1.11	1.31	1.16	1.14	1.52	1.49	1.38	1.07	1.46	1.29	1.04	1.06
Cr2O3	0.42	0.47	0.57	0.41	0.44	0.55	0.51	0.46	0.40	0.59	0.43	0.43	0.47
Fe2O3	0.00	0.00	1.14	0.00	0.00	0.00	0.00	0.00	0.00	0.00	0.00	0.00	0.42
FeO	14.04	12.04	11.34	13.60	13.11	13.64	13.23	13.49	13.19	10.89	13.52	13.21	12.00
MnO	0.29	0.22	0.27	0.32	0.26	0.28	0.23	0.30	0.28	0.28	0.25	0.28	0.24
NiO	0.12	0.09	0.16	0.18	0.09	0.14	0.14	0.05	0.14	0.15	0.15	0.11	0.10
MgO	28.66	27.48	27.02	28.87	27.86	28.69	28.19	28.61	29.08	25.73	28.95	28.56	27.89
CaO	0.79	3.45	4.31	0.83	2.29	0.60	1.65	0.81	0.77	5.60	0.89	0.83	3.32
Na2O	0.04	0.10	0.06	0.00	0.03	0.04	0.01	0.02	0.01	0.14	0.00	0.00	0.06
Total	101.51	100.82	101.16	101.33	101.02	100.98	100.85	100.63	100.68	100.00	101.82	99.85	101.29
Si	1.97	1.97	1.95	1.97	1.97	1.96	1.96	1.97	1.97	1.97	1.97	1.97	1.96
Ti	0.00	0.00	0.00	0.00	0.00	0.00	0.00	0.00	0.00	0.01	0.00	0.01	0.01
Al	0.05	0.05	0.05	0.05	0.05	0.06	0.06	0.06	0.04	0.06	0.05	0.04	0.04
Cr	0.01	0.01	0.02	0.01	0.01	0.02	0.01	0.01	0.01	0.02	0.01	0.01	0.01
Fe	0.41	0.36	0.37	0.40	0.39	0.40	0.39	0.40	0.39	0.33	0.40	0.40	0.37
Mn	0.01	0.01	0.01	0.01	0.01	0.01	0.01	0.01	0.01	0.01	0.01	0.01	0.01
Ni	0.00	0.00	0.00	0.00	0.00	0.00	0.00	0.00	0.00	0.00	0.00	0.00	0.00
Mg	1.51	1.45	1.43	1.52	1.47	1.51	1.49	1.51	1.54	1.37	1.51	1.52	1.47
Ca	0.03	0.13	0.16	0.03	0.09	0.02	0.06	0.03	0.03	0.21	0.03	0.03	0.13
Na	0.00	0.01	0.00	0.00	0.00	0.00	0.00	0.00	0.00	0.01	0.00	0.00	0.00
total	4.00	3.99	4.01	4.00	4.00	4.00	4.00	4.00	4.00	3.99	3.99	3.99	4.00
Mg#	78	80	80	79	79	79	79	79	80	81	79	79	80
Wo	2	7	8	2	4	1	3	2	1	11	2	2	6
En	77	75	73	77	75	78	76	77	78	71	78	78	75
Fs	22	19	19	21	20	21	20	21	20	17	21	21	19

Table A3 Continued, Orthopyroxene compositions from the Reef pyroxenite, Merensky Reef, Winnaarshoek.

Depth (m)	194.9	194.9	194.9	194.9	194.9	194.9	194.9
Sample	R7_1-opx_14	R7_1-opx_15	R7_1-opx_16	R7_1-opx_17	R7_1-opx_18	R7_1-opx_19	R7_1-opx_20
SiO2	55.78	56.31	55.86	56.04	56.51	56.23	53.37
TiO2	0.29	0.25	0.24	0.17	0.10	0.15	0.12
Al2O3	0.86	0.87	1.00	1.07	0.82	1.01	0.85
Cr2O3	0.22	0.24	0.26	0.35	0.23	0.33	0.19
Fe2O3	0.64	0.00	0.00	0.00	0.00	0.00	0.00
FeO	13.08	13.30	12.86	12.01	12.58	13.05	10.34
MnO	0.33	0.29	0.30	0.21	0.23	0.25	0.24
NiO	0.11	0.17	0.18	0.17	0.10	0.13	0.07
MgO	29.48	29.44	28.74	28.64	30.07	29.77	27.93
CaO	0.68	0.69	0.72	1.50	0.40	0.61	0.81
Na2O	0.01	0.01	0.01	0.04	0.03	0.02	0.02
Total	101.48	101.55	100.16	100.20	101.06	101.55	93.93
Si	1.97	1.98	1.98	1.99	1.98	1.97	2.00
Ti	0.01	0.01	0.01	0.00	0.00	0.00	0.00
Al	0.04	0.04	0.04	0.04	0.03	0.04	0.04
Cr	0.01	0.01	0.01	0.01	0.01	0.01	0.01
Fe	0.40	0.39	0.38	0.36	0.37	0.38	0.32
Mn	0.01	0.01	0.01	0.01	0.01	0.01	0.01
Ni	0.00	0.00	0.01	0.00	0.00	0.00	0.00
Mg	1.55	1.54	1.52	1.51	1.57	1.56	1.56
Ca	0.03	0.03	0.03	0.06	0.02	0.02	0.03
Na	0.00	0.00	0.00	0.00	0.00	0.00	0.00
total	4.01	4.00	3.99	3.98	3.99	4.00	3.97
Mg#	79	80	80	81	81	80	83
Wo	1	1	1	3	1	1	2
En	78	78	78	78	80	79	81
Fs	21	20	20	19	19	20	17

Table A3 Continued, Orthopyroxene compositions from the Reef pyroxenite, Merensky Reef, Winnaarshoek.

194.9	194.9	194.9	194.9	194.9	194.9
R7_1-opx_21	R7_1-opx_22	R7_1-opx_23	R7_1-opx_24	R7_1-opx_25	R7_1-opx_26
55.37	56.03	56.00	55.34	55.23	55.64
0.23	0.11	0.20	0.19	0.08	0.16
1.08	0.92	1.26	1.16	1.84	1.13
0.38	0.17	0.39	0.42	0.49	0.43
0.00	0.00	0.48	0.00	0.00	0.82
12.78	11.82	12.84	11.40	13.50	12.37
0.27	0.22	0.22	0.24	0.23	0.24
0.06	0.10	0.14	0.09	0.11	0.14
29.11	29.66	29.77	27.87	28.51	29.39
0.83	0.59	0.68	3.31	0.83	1.13
0.00	0.03	0.00	0.07	0.01	0.03
100.11	99.66	101.98	100.09	100.83	101.46
1.97	1.99	1.96	1.97	1.96	1.96
0.01	0.00	0.01	0.00	0.00	0.00
0.05	0.04	0.05	0.05	0.08	0.05
0.01	0.00	0.01	0.01	0.01	0.01
0.38	0.35	0.39	0.34	0.40	0.39
0.01	0.01	0.01	0.01	0.01	0.01
0.00	0.00	0.00	0.00	0.00	0.00
1.54	1.57	1.55	1.48	1.51	1.54
0.03	0.02	0.03	0.13	0.03	0.04
0.00	0.00	0.00	0.00	0.00	0.00
4.00	3.99	4.00	4.00	4.00	4.01
80	82	80	81	79	80
2	1	1	6	2	2
79	81	79	76	77	78
20	18	20	18	21	20

Table A3 Continued, Orthopyroxene compositions from the Reef pyroxenite, Merensky Reef, Winnaarshoek.

Depth (m)	194.6	194.6	194.6	194.6	194.6	194.6	194.6	194.6	194.6
Sample	R8_opx1_33	R8_opx1_34	R8_opx1_35	R8_opx1_36	R8_opx1_37	R8_opx1_38	R8_opx1_39	R8_opx1_40	R8_opx1_41
SiO2	54.21	55.27	54.89	55.08	54.81	54.53	55.13	55.54	55.84
TiO2	0.21	0.13	0.16	0.24	0.17	0.21	0.20	0.19	0.21
Al2O3	1.39	1.23	1.19	1.26	1.32	1.45	0.98	1.08	1.03
Cr2O3	0.43	0.38	0.35	0.41	0.42	0.41	0.34	0.33	0.32
Fe2O3	1.15	0.70	0.12	0.00	1.07	0.00	0.63	0.44	0.00
FeO	12.09	12.71	12.60	12.99	12.72	12.79	11.71	12.04	12.74
MnO	0.27	0.23	0.31	0.29	0.30	0.34	0.21	0.26	0.27
NiO	0.12	0.12	0.09	0.08	0.12	0.12	0.12	0.10	0.12
MgO	28.92	28.97	28.75	28.67	28.92	27.58	29.75	29.08	29.64
CaO	0.75	1.16	1.00	0.73	0.79	0.84	0.80	1.78	0.71
Na2O	0.00	0.01	0.06	0.00	0.00	0.02	0.00	0.01	0.00
Total	0.00	0.00	0.00	0.00	0.00	0.00	0.00	0.00	0.00
	99.54	100.92	99.51	99.74	100.61	98.29	99.86	100.86	100.89
Si	1.95	1.96	1.97	1.97	1.95	1.98	1.96	1.96	1.97
Ti	0.01	0.00	0.00	0.01	0.00	0.01	0.01	0.01	0.01
Al	0.06	0.05	0.05	0.05	0.06	0.06	0.04	0.04	0.04
Cr	0.01	0.01	0.01	0.01	0.01	0.01	0.01	0.01	0.01
Fe	0.39	0.40	0.38	0.39	0.41	0.39	0.37	0.37	0.38
Mn	0.01	0.01	0.01	0.01	0.01	0.01	0.01	0.01	0.01
Ni	0.00	0.00	0.00	0.00	0.00	0.00	0.00	0.00	0.00
Mg	1.55	1.53	1.54	1.53	1.54	1.49	1.58	1.53	1.56
Ca	0.03	0.04	0.04	0.03	0.03	0.03	0.03	0.07	0.03
Na	0.00	0.00	0.00	0.00	0.00	0.00	0.00	0.00	0.00
total	4.01	4.01	4.00	3.99	4.01	3.98	4.01	4.00	4.00
Mg#	80	79	80	80	79	79	81	81	81
Wo	1	2	2	1	2	2	2	3	1
En	78	77	78	78	77	78	80	78	79
Fs	20	20	20	20	21	21	19	19	19

Table A3 Continued, Orthopyroxene compositions from the Reef pyroxenite, Merensky Reef, Winnaarshoek.

194.6	194.6	194.6	194.6	194.6	194.6	194.6	194.6	194.6	194.6
R8_opx1_42	R8_opx1_43	R8_opx1_44	R8_opx1_45	R8_opx1_46	R8_opx1_47	R8_opx1_48	R8_opx1_49	R8_opx1_50	R8_opx1_51
55.82	55.60	55.41	55.79	55.71	55.87	56.06	56.24	56.17	56.35
0.18	0.16	0.20	0.14	0.22	0.13	0.18	0.14	0.06	0.14
1.06	0.91	1.10	0.97	1.23	1.09	1.08	1.10	1.06	1.17
0.26	0.37	0.31	0.37	0.42	0.39	0.36	0.37	0.34	0.41
0.00	0.03	0.99	0.42	0.74	0.00	0.00	0.00	0.00	0.00
12.07	12.79	12.23	12.12	10.15	11.77	11.70	12.84	12.04	11.15
0.26	0.23	0.26	0.26	0.25	0.25	0.23	0.32	0.28	0.25
0.06	0.13	0.08	0.09	0.08	0.17	0.13	0.07	0.09	0.11
28.27	29.63	29.23	28.93	27.81	29.58	29.45	29.65	29.70	27.84
2.21	0.52	1.17	1.99	4.92	0.80	1.31	0.90	0.61	3.14
0.03	0.00	0.06	0.06	0.10	0.03	0.06	0.03	0.02	0.07
0.00	0.00	0.00	0.00	0.00	0.00	0.00	0.00	0.00	0.00
100.22	100.36	101.05	101.12	101.64	100.07	100.56	101.65	100.35	100.62
1.98	1.97	1.96	1.97	1.96	1.98	1.98	1.97	1.98	1.99
0.00	0.00	0.01	0.00	0.01	0.00	0.00	0.00	0.00	0.00
0.04	0.04	0.05	0.04	0.05	0.05	0.04	0.05	0.04	0.05
0.01	0.01	0.01	0.01	0.01	0.01	0.01	0.01	0.01	0.01
0.36	0.38	0.39	0.37	0.32	0.35	0.35	0.38	0.36	0.33
0.01	0.01	0.01	0.01	0.01	0.01	0.01	0.01	0.01	0.01
0.00	0.00	0.00	0.00	0.00	0.00	0.00	0.00	0.00	0.00
1.50	1.57	1.54	1.52	1.46	1.56	1.55	1.55	1.56	1.46
0.08	0.02	0.04	0.08	0.19	0.03	0.05	0.03	0.02	0.12
0.00	0.00	0.00	0.00	0.01	0.00	0.00	0.00	0.00	0.00
3.99	4.00	4.01	4.00	4.01	3.99	3.99	4.00	3.99	3.98
81	80	80	80	82	82	82	80	81	82
4	1	2	4	9	2	3	2	1	6
77	79	78	77	74	80	79	79	80	76
19	20	20	19	17	18	18	20	19	18

Table A4 Orthopyroxene compositions from the footwall leuconorite, Merensky Reef, Winnaarshoek.

Depth (m)	198.5	198.5	198.5	198.5	198.5	198.5	198.5	198.5	198.5
Sample	WH31_7_118	WH31_7_119	WH31_7_120	WH31_7_121	WH31_7_122	WH31_7_123	WH31_7_124	WH31_7_125	WH31_7_126
SiO2	55.15	54.75	55.41	55.34	54.76	55.24	55.11	54.95	54.85
TiO2	0.08	0.11	0.12	0.13	0.14	0.12	0.13	0.10	0.16
Al2O3	1.35	1.28	1.17	1.26	1.22	1.14	1.34	1.31	1.30
Cr2O3	0.06	0.40	0.41	0.08	0.41	0.39	0.06	0.37	0.43
Fe2O3	0.00	0.00	0.00	0.00	0.00	0.00	0.00	0.00	0.00
FeO	10.70	11.63	11.24	11.92	10.56	11.66	11.66	12.25	10.72
MnO	0.29	0.27	0.26	0.32	0.26	0.27	0.25	0.29	0.25
NiO	0.00	0.00	0.00	0.00	0.00	0.00	0.00	0.00	0.00
MgO	28.41	28.70	29.42	29.22	27.16	29.16	28.59	29.46	28.22
CaO	3.01	1.71	0.58	0.80	4.34	0.69	1.88	0.48	2.60
Na2O	0.02	0.00	0.00	0.05	0.02	0.00	0.00	0.00	0.00
Total	99.08	98.86	98.61	99.11	98.86	98.66	99.02	99.22	98.53
Si	1.97	1.97	1.98	1.98	1.97	1.98	1.97	1.97	1.97
Ti	0.00	0.00	0.00	0.00	0.00	0.00	0.00	0.00	0.00
Al	0.06	0.05	0.05	0.05	0.05	0.05	0.06	0.06	0.06
Cr	0.00	0.01	0.01	0.00	0.01	0.01	0.00	0.01	0.01
Fe	0.32	0.35	0.34	0.36	0.32	0.35	0.35	0.37	0.32
Mn	0.01	0.01	0.01	0.01	0.01	0.01	0.01	0.01	0.01
Ni	0.00	0.00	0.00	0.00	0.00	0.00	0.00	0.00	0.00
Mg	1.52	1.54	1.57	1.56	1.46	1.56	1.53	1.57	1.51
Ca	0.12	0.07	0.02	0.03	0.17	0.03	0.07	0.02	0.10
Na	0.00	0.00	0.00	0.00	0.00	0.00	0.00	0.00	0.00
total	4.00	4.00	3.98	3.99	3.99	3.99	3.99	4.00	3.99
Mg#	83	81	82	81	82	82	81	81	82
Wo	6	3	1	2	9	1	4	1	5
En	77	78	81	80	75	80	78	80	78
Fs	17	18	18	19	17	18	18	19	17

Table A4 Continued, orthopyroxene compositions from the footwall leuconorite, Merensky Reef, Winnaarshoek.

198.5	198.5	198.5	200	200	200	200	200	200
WH31_7_136	WH31_7_137	WH31_7_138	WH31_8_16a	WH31_8_17a	WH31_7_18a	WH31_7_19a	WH31_7_20a	WH31_7_21a
54.90	54.60	54.85	56.18	56.23	55.90	56.08	56.05	56.10
0.11	0.13	0.16	0.13	0.16	0.15	0.09	0.11	0.10
1.40	1.61	1.32	1.05	0.99	1.05	1.09	1.10	1.01
0.39	0.37	0.04	0.35	0.05	0.37	0.07	0.06	0.37
0.00	0.00	0.00	0.00	0.03	0.00	0.00	0.00	0.00
12.03	12.15	11.90	11.52	11.56	11.34	11.28	11.75	11.33
0.32	0.27	0.28	0.31	0.26	0.30	0.25	0.29	0.24
0.00	0.00	0.00	0.00	0.00	0.00	0.00	0.00	0.00
28.88	28.42	28.92	30.07	29.91	29.51	30.16	30.02	29.41
0.76	1.53	0.71	0.90	1.61	1.76	0.64	0.74	1.88
0.00	0.00	0.02	0.00	0.04	0.00	0.00	0.00	0.00
98.78	99.08	98.20	100.51	100.84	100.38	99.65	100.11	100.44
1.97	1.96	1.98	1.98	1.98	1.97	1.98	1.98	1.98
0.00	0.00	0.00	0.00	0.00	0.00	0.00	0.00	0.00
0.06	0.07	0.06	0.04	0.04	0.04	0.05	0.05	0.04
0.01	0.01	0.00	0.01	0.00	0.01	0.00	0.00	0.01
0.36	0.37	0.36	0.34	0.34	0.33	0.33	0.35	0.33
0.01	0.01	0.01	0.01	0.01	0.01	0.01	0.01	0.01
0.00	0.00	0.00	0.00	0.00	0.00	0.00	0.00	0.00
1.55	1.52	1.55	1.58	1.57	1.55	1.59	1.58	1.55
0.03	0.06	0.03	0.03	0.06	0.07	0.02	0.03	0.07
0.00	0.00	0.00	0.00	0.00	0.00	0.00	0.00	0.00
3.99	4.00	3.99	3.99	4.00	4.00	3.99	3.99	3.99
81	81	81	82	82	82	83	82	82
2	3	1	2	3	3	1	1	4
79	78	80	80	79	79	81	80	79
19	19	19	18	18	18	17	18	17

Table A4 Continued, orthopyroxene compositions from the footwall leuconorite, Merensky Reef, Winnaarshoek.

200	200	200	200	200	200	200	200	200
WH31_7_22a	WH31_7_23a	WH31_7_24a	WH31_7_26a	WH31_7_32a	WH31_7_33a	WH31_7_36a	WH31_7_37a	WH31_7_38a
56.19	55.87	56.18	55.00	56.07	55.80	56.03	56.13	55.68
0.15	0.16	0.16	0.22	0.14	0.17	0.13	0.11	0.15
1.01	1.01	1.02	1.47	1.12	0.92	1.22	1.17	1.15
0.33	0.35	0.37	0.46	0.35	0.28	0.38	0.06	0.08
0.00	0.00	0.00	0.00	0.00	0.00	0.00	0.00	0.00
11.74	11.44	11.46	9.65	11.72	11.54	10.72	12.12	10.69
0.30	0.31	0.29	0.26	0.29	0.29	0.28	0.29	0.26
0.00	0.00	0.00	0.00	0.00	0.00	0.00	0.00	0.00
29.94	29.85	29.45	23.40	29.44	29.20	28.84	29.53	28.52
0.97	0.90	1.10	10.74	1.17	0.80	2.55	1.41	2.83
0.00	0.00	0.00	0.00	0.00	0.00	0.01	0.00	0.00
100.63	99.88	100.03	101.21	100.28	99.00	100.16	100.82	99.37
1.98	1.98	1.99	1.96	1.98	1.99	1.98	1.98	1.98
0.00	0.00	0.00	0.01	0.00	0.00	0.00	0.00	0.00
0.04	0.04	0.04	0.06	0.05	0.04	0.05	0.05	0.05
0.01	0.01	0.01	0.01	0.01	0.01	0.01	0.00	0.00
0.35	0.34	0.34	0.29	0.35	0.34	0.32	0.36	0.32
0.01	0.01	0.01	0.01	0.01	0.01	0.01	0.01	0.01
0.00	0.00	0.00	0.00	0.00	0.00	0.00	0.00	0.00
1.57	1.58	1.55	1.24	1.55	1.55	1.52	1.55	1.51
0.04	0.03	0.04	0.41	0.04	0.03	0.10	0.05	0.11
0.00	0.00	0.00	0.00	0.00	0.00	0.00	0.00	0.00
3.99	3.99	3.98	3.99	3.99	3.98	3.99	4.00	3.99
82	82	82	81	82	82	83	81	83
2	2	2	21	2	2	5	3	6
80	80	80	64	80	80	78	79	78
18	18	18	15	18	18	17	19	17

Table A5 Orthopyroxene compositions from the footwall anorthosite, Merensky Reef, Winnaarshoek.

Depth (m)	202	202	202	202	202.1	202.1	202.1	202.1	202.1
Sample	WH31_09_1	WH31_09_2	WH31_09_3	WH31_09_4	WH31_10_66	WH31_10_67	WH31_10_68	WH31_10_69	WH31_10_70
SiO2	55.20	55.19	55.42	55.62	55.47	55.73	55.20	55.20	55.18
TiO2	0.14	0.16	0.17	0.11	0.02	0.08	0.09	0.07	0.11
Al2O3	1.02	1.19	1.09	1.24	1.79	1.49	1.80	1.95	1.76
Cr2O3	0.31	0.32	0.31	0.05	0.19	0.14	0.30	0.27	0.36
Fe2O3	0.00	0.00	0.00	0.00	0.00	0.00	0.06	0.48	0.00
FeO	12.05	12.08	12.29	12.49	10.43	10.50	10.80	10.50	9.87
MnO	0.27	0.28	0.27	0.30	0.28	0.28	0.25	0.27	0.26
NiO	0.00	0.00	0.00	0.00	0.00	0.00	0.00	0.00	0.00
MgO	28.85	29.14	29.22	29.43	30.43	30.51	30.24	30.50	28.44
CaO	1.21	0.83	0.89	0.64	0.63	0.63	0.88	0.73	2.82
Na2O	0.00	0.00	0.00	0.04	0.00	0.04	0.00	0.00	0.01
Total	99.04	99.17	99.66	99.92	99.24	99.41	99.61	99.97	98.80
Si	1.98	1.97	1.97	1.98	1.97	1.97	1.96	1.95	1.97
Ti	0.00	0.00	0.00	0.00	0.00	0.00	0.00	0.00	0.00
Al	0.04	0.05	0.05	0.05	0.07	0.06	0.08	0.08	0.07
Cr	0.01	0.01	0.01	0.00	0.01	0.00	0.01	0.01	0.01
Fe	0.36	0.36	0.37	0.37	0.31	0.31	0.32	0.32	0.29
Mn	0.01	0.01	0.01	0.01	0.01	0.01	0.01	0.01	0.01
Ni	0.00	0.00	0.00	0.00	0.00	0.00	0.00	0.00	0.00
Mg	1.54	1.55	1.55	1.56	1.61	1.61	1.60	1.61	1.51
Ca	0.05	0.03	0.03	0.02	0.02	0.02	0.03	0.03	0.11
Na	0.00	0.00	0.00	0.00	0.00	0.00	0.00	0.00	0.00
total	3.99	3.99	3.99	4.00	3.99	3.99	4.00	4.00	3.98
Mg#	81	81	81	81	84	84	83	83	84
Wo	2	2	2	1	1	1	2	1	6
En	79	79	79	79	82	82	82	82	79
Fs	19	19	19	19	16	16	17	17	16

Table A5 Continued, orthopyroxene compositions from the footwall anorthosite, Merensky Reef, Winnaarshoek.

202.1	202.1	202.1	202.1	202.1	202.1	202.1	202.1	202.1
WH31_10_71	WH31_10_72	WH31_10_73	WH31_10_74	WH31_10_75	WH31_10_76	WH31_10_77	WH31_10_78	WH31_10_79
54.90	56.88	55.70	54.99	54.75	55.13	55.55	55.54	55.11
0.09	0.00	0.12	0.14	0.15	0.14	0.09	0.10	0.18
1.84	0.19	1.20	1.41	1.56	1.26	1.08	1.09	0.96
0.44	0.00	0.32	0.38	0.39	0.33	0.25	0.36	0.24
0.24	0.00	0.00	0.00	0.00	0.00	0.00	0.00	0.00
9.59	10.55	11.66	10.50	10.57	11.65	10.95	11.89	12.27
0.20	0.31	0.23	0.23	0.30	0.27	0.28	0.26	0.31
0.00	0.00	0.00	0.00	0.00	0.00	0.00	0.00	0.00
27.49	31.30	29.58	27.39	27.40	29.20	29.43	29.75	29.19
5.41	0.50	1.21	3.72	3.69	0.77	0.96	0.50	0.61
0.00	0.00	0.00	0.02	0.00	0.02	0.00	0.00	0.01
100.19	99.72	100.02	98.80	98.82	98.78	98.60	99.48	98.90
1.95	2.00	1.97	1.98	1.97	1.98	1.99	1.98	1.98
0.00	0.00	0.00	0.00	0.00	0.00	0.00	0.00	0.00
0.08	0.01	0.05	0.06	0.07	0.05	0.05	0.05	0.04
0.01	0.00	0.01	0.01	0.01	0.01	0.01	0.01	0.01
0.29	0.31	0.35	0.32	0.32	0.35	0.33	0.35	0.37
0.01	0.01	0.01	0.01	0.01	0.01	0.01	0.01	0.01
0.00	0.00	0.00	0.00	0.00	0.00	0.00	0.00	0.00
1.46	1.64	1.56	1.47	1.47	1.56	1.57	1.58	1.56
0.21	0.02	0.05	0.14	0.14	0.03	0.04	0.02	0.02
0.00	0.00	0.00	0.00	0.00	0.00	0.00	0.00	0.00
4.00	3.99	3.99	3.99	3.99	3.99	3.98	3.99	3.99
83	84	82	82	82	82	83	82	81
11	1	2	7	7	2	2	1	1
74	83	80	76	76	80	81	81	80
15	16	18	17	17	18	17	18	19

Table A5 Continued, orthopyroxene compositions from the footwall anorthosite, Merensky Reef, Winnaarshoek.

202.1	202.1	202.1	202.1	202.1	202.1	202.1	202.1	202.2
WH31_10_80	WH31_10_81	WH31_10_82	WH31_10_83	WH31_10_84	WH31_10_85	WH31_11_2a	WH31_11_5a	WH31_11_11a
54.99	55.15	55.28	54.63	55.53	54.94	56.00	55.84	55.81
0.19	0.12	0.13	0.20	0.12	0.12	0.16	0.13	0.13
0.98	1.36	1.51	0.93	1.40	1.43	1.12	0.92	1.21
0.30	0.31	0.31	0.29	0.28	0.34	0.33	0.28	0.29
0.00	0.00	0.00	0.00	0.00	0.00	0.25	0.61	0.00
11.60	12.00	11.61	14.09	11.55	11.08	12.59	12.12	13.11
0.33	0.32	0.26	0.37	0.25	0.30	0.33	0.34	0.27
0.00	0.00	0.00	0.00	0.00	0.00	0.00	0.00	0.00
28.88	29.31	29.07	27.86	30.01	29.61	29.69	29.91	29.43
0.64	0.63	0.80	0.78	0.71	1.18	0.88	0.88	0.72
0.01	0.00	0.04	0.02	0.00	0.00	0.03	0.00	0.01
97.93	99.19	99.00	99.18	99.84	98.99	101.37	101.03	100.96
1.99	1.97	1.98	1.97	1.97	1.96	1.97	1.97	1.97
0.01	0.00	0.00	0.01	0.00	0.00	0.00	0.00	0.00
0.04	0.06	0.06	0.04	0.06	0.06	0.05	0.04	0.05
0.01	0.01	0.01	0.01	0.01	0.01	0.01	0.01	0.01
0.35	0.36	0.35	0.43	0.34	0.33	0.38	0.37	0.39
0.01	0.01	0.01	0.01	0.01	0.01	0.01	0.01	0.01
0.00	0.00	0.00	0.00	0.00	0.00	0.00	0.00	0.00
1.56	1.56	1.55	1.50	1.58	1.58	1.55	1.57	1.55
0.02	0.02	0.03	0.03	0.03	0.05	0.03	0.03	0.03
0.00	0.00	0.00	0.00	0.00	0.00	0.00	0.00	0.00
3.98	3.99	3.99	4.00	4.00	4.00	4.00	4.01	4.00
82	81	82	78	82	83	80	81	80
1	1	2	2	1	2	2	2	1
80	80	80	76	81	80	79	79	79
19	19	18	22	18	17	20	19	20

Appendix B- Clinopyroxene compositions (EPMA) from the Merensky Reef at Winnaarshoek

Table B1 Clinopyroxene composistions from the hanging wall anorthosite, Merensky Reef, Winnaarshoek.

Depth (m)	182	182	182	182	182	182	182	188.8	188.8
Sample	WH31_5	WH31_6	WH31_7	WH31_8	WH31_9	WH31_10	WH31_11	WH31_18	WH31_19
SiO2	52.48	52.18	52.18	51.97	52.27	52.00	52.66	52.76	53.05
TiO2	0.46	0.30	0.32	0.33	0.38	0.39	0.37	0.39	0.47
Al2O3	1.79	2.45	2.50	1.59	1.69	1.58	1.88	1.69	1.79
Cr2O3	0.10	0.87	0.86	0.37	0.09	0.39	0.56	0.44	0.47
Fe2O3	1.03	0.00	0.33	1.21	0.61	0.91	0.00	0.00	0.00
FeO	7.24	3.69	3.62	5.85	7.82	5.79	5.87	7.24	6.45
MnO	0.22	0.08	0.12	0.25	0.25	0.22	0.13	0.19	0.13
NiO	0.00	0.00	0.00	0.00	0.00	0.00	0.00	0.00	0.00
MgO	16.70	16.01	16.00	15.22	15.75	15.03	16.00	16.64	16.47
CaO	20.10	23.22	23.56	22.69	20.85	23.14	21.72	19.53	20.31
Na2O	0.04	0.09	0.05	0.03	0.00	0.02	0.02	0.00	0.00
Total	100.15	98.89	99.53	99.52	99.70	99.47	99.20	98.89	99.14
Si	1.94	1.93	1.92	1.94	1.95	1.94	1.95	1.96	1.96
Ti	0.01	0.01	0.01	0.01	0.01	0.01	0.01	0.01	0.01
Al	0.08	0.11	0.11	0.07	0.07	0.07	0.08	0.07	0.08
Cr	0.00	0.03	0.03	0.01	0.00	0.01	0.02	0.01	0.01
Fe	0.25	0.11	0.12	0.22	0.26	0.21	0.18	0.22	0.20
Mn	0.01	0.00	0.00	0.01	0.01	0.01	0.00	0.01	0.00
Ni	0.00	0.00	0.00	0.00	0.00	0.00	0.00	0.00	0.00
Mg	0.92	0.88	0.88	0.85	0.87	0.84	0.88	0.92	0.91
Ca	0.80	0.92	0.93	0.91	0.83	0.93	0.86	0.78	0.80
Na	0.00	0.01	0.00	0.00	0.00	0.00	0.00	0.00	0.00
total	4.01	4.00	4.00	4.01	4.01	4.01	3.99	3.99	3.98
Mg#	78	89	88	80	77	80	83	80	82
Wo	40	48	48	46	42	47	45	40	42
En	47	46	45	43	44	42	46	48	47
Fs	13	6	6	11	14	11	10	12	11

Table B2 Clinopyroxene composistions from the hanging wall leuconorite, Merensky Reef, Winnaarshoek.

Depth (m)	190.8	190.8	190.8	190.8	190.8	190.8	191.5	191.5	191.5	191.5	191.5
Sample	WH31_21	WH31_22	WH31_23	WH31_33	WH31_34	WH31_104	WH31_108	WH31_109	WH31_110	WH31_111	WH31_114
SiO2	52.29	52.06	52.12	51.89	52.33	54.29	52.72	52.69	52.46	51.74	54.13
TiO2	0.31	0.28	0.25	0.29	0.27	0.15	0.37	0.35	0.33	0.39	0.27
Al2O3	2.35	2.31	3.23	2.29	2.40	1.55	1.90	1.91	2.17	3.06	4.42
Cr2O3	0.96	0.93	0.94	0.84	0.89	0.50	0.84	0.13	0.95	0.97	0.60
Fe2O3	0.00	0.00	0.00	0.00	0.00	0.00	0.00	0.00	0.00	0.00	0.00
FeO	5.58	5.28	7.25	5.72	5.79	12.03	4.66	4.27	4.89	4.62	4.61
MnO	0.20	0.20	0.19	0.20	0.18	0.23	0.11	0.09	0.19	0.12	0.14
NiO	0.00	0.00	0.00	0.00	0.00	0.00	0.00	0.00	0.00	0.00	0.00
MgO	14.99	14.92	17.85	15.26	15.33	26.13	15.41	15.74	15.32	14.97	16.15
CaO	23.31	23.10	16.68	22.38	22.21	3.86	23.19	23.68	23.17	23.32	23.50
Na2O	0.04	0.06	0.01	0.03	0.01	0.00	0.00	0.02	0.00	0.09	0.06
Total	100.02	99.13	98.51	98.89	99.41	98.73	99.19	98.88	99.49	99.28	103.88
Si	1.93	1.94	1.93	1.93	1.94	1.97	1.95	1.95	1.94	1.92	1.91
Ti	0.01	0.01	0.01	0.01	0.01	0.00	0.01	0.01	0.01	0.01	0.01
Al	0.10	0.10	0.14	0.10	0.10	0.07	0.08	0.08	0.09	0.13	0.18
Cr	0.03	0.03	0.03	0.02	0.03	0.01	0.02	0.00	0.03	0.03	0.02
Fe	0.17	0.16	0.22	0.18	0.18	0.36	0.14	0.13	0.15	0.14	0.14
Mn	0.01	0.01	0.01	0.01	0.01	0.01	0.00	0.00	0.01	0.00	0.00
Ni	0.00	0.00	0.00	0.00	0.00	0.00	0.00	0.00	0.00	0.00	0.00
Mg	0.82	0.83	0.98	0.85	0.85	1.41	0.85	0.87	0.84	0.83	0.85
Ca	0.92	0.92	0.66	0.89	0.88	0.15	0.92	0.94	0.92	0.93	0.89
Na	0.00	0.00	0.00	0.00	0.00	0.00	0.00	0.00	0.00	0.01	0.00
total	4.00	3.99	3.98	4.00	3.99	3.99	3.99	4.00	3.99	3.99	3.99
Mg#	83	83	81	83	83	79	85	87	85	85	86
Wo	48	48	35	46	46	8	48	48	48	49	47
En	43	43	52	44	44	73	44	45	44	44	45
Fs	9	9	12	10	10	19	8	7	8	8	7

Table B3 Clinopyroxene composistions from the Reef pyroxenites, Merensky Reef, Winnaarshoek.

Depth (m)	192.1	192.1	192.1	192.1	192.1	192.1	192.1	192.1	192.1	192.1	192.1
Sample	R1-cpx-32	R1-cpx-33	R1-cpx-34	R1-cpx-35	R1-cpx-36	R1-cpx-37	R1-cpx-38	R1-cpx-39	R1-cpx-40	R1-cpx-41	R1-cpx-42
SiO2	52.74	53.60	53.45	54.16	53.05	53.44	54.22	54.22	53.52	53.83	54.47
TiO2	0.25	0.32	0.32	0.30	0.29	0.30	0.16	0.31	0.27	0.39	0.36
Al2O3	2.17	1.89	2.13	1.45	2.37	2.21	1.51	2.61	2.22	1.59	1.59
Cr2O3	0.77	0.91	0.89	0.85	1.04	0.88	0.81	0.92	0.89	0.89	0.95
Fe2O3	1.75	0.00	0.36	0.00	0.48	0.47	0.00	0.00	0.14	0.74	0.00
FeO	5.82	5.22	4.91	4.38	4.53	4.47	4.86	8.29	4.87	3.72	4.55
MnO	0.17	0.15	0.16	0.14	0.17	0.11	0.12	0.18	0.16	0.12	0.16
NiO	0.10	0.11	0.07	0.05	0.07	0.04	0.03	0.12	0.04	0.12	0.04
MgO	17.44	15.90	15.50	16.27	15.43	15.85	16.49	19.15	16.01	15.98	16.16
CaO	19.44	22.27	23.28	23.26	22.99	22.97	22.43	15.56	22.39	23.60	23.10
Na2O	0.27	0.37	0.35	0.32	0.43	0.40	0.32	0.38	0.42	0.44	0.32
Total	100.89	100.75	101.43	101.18	100.84	101.14	100.95	101.73	100.94	101.42	101.69
Si	1.93	1.95	1.94	1.96	1.94	1.94	1.97	1.94	1.95	1.95	1.96
Ti	0.01	0.01	0.01	0.01	0.01	0.01	0.00	0.01	0.01	0.01	0.01
Al	0.09	0.08	0.09	0.06	0.10	0.09	0.06	0.11	0.10	0.07	0.07
Cr	0.02	0.03	0.03	0.02	0.03	0.03	0.02	0.03	0.03	0.03	0.03
Fe	0.23	0.16	0.16	0.13	0.15	0.15	0.15	0.25	0.15	0.13	0.14
Mn	0.01	0.00	0.01	0.00	0.01	0.00	0.00	0.01	0.00	0.00	0.00
Ni	0.00	0.00	0.00	0.00	0.00	0.00	0.00	0.00	0.00	0.00	0.00
Mg	0.95	0.86	0.84	0.88	0.84	0.86	0.89	1.02	0.87	0.86	0.87
Ca	0.76	0.87	0.91	0.90	0.90	0.89	0.87	0.60	0.87	0.92	0.89
Na	0.02	0.03	0.02	0.02	0.03	0.03	0.02	0.03	0.03	0.03	0.02
total	4.02	4.00	4.00	4.00	4.00	4.00	4.00	3.99	4.00	4.01	3.99
Mg#	81	84	84	87	85	85	86	80	85	87	86
Wo	39	46	47	47	47	47	46	32	46	48	47
En	49	46	44	46	44	45	47	55	46	45	46
Fs	12	9	9	7	8	8	8	14	8	7	7

Table B3 Continued, clinopyroxene composistions from the Reef pyroxenites, Merensky Reef, Winnaarshoek.

Depth (m)	194.9	194.9	194.9	194.9	194.9	194.9	194.9	194.9	194.9
Sample	R7_cpx_23	R7_cpx_24	R7_cpx_25	R7_cpx_26	R7_cpx_27	R7_cpx_28	R7_cpx_29	R7_cpx_30	R7_cpx_31
SiO2	53.63	53.08	52.84	53.53	53.33	53.28	53.17	53.58	53.04
TiO2	0.38	0.36	0.54	0.45	0.22	0.18	0.29	0.30	0.35
Al2O3	1.62	2.09	1.98	1.90	1.96	2.29	1.97	1.97	2.05
Cr2O3	0.72	0.87	0.58	0.86	0.87	0.81	0.84	0.76	0.80
Fe2O3	0.48	0.06	0.08	0.00	0.96	0.66	0.16	0.28	0.44
FeO	3.87	4.70	6.29	4.46	3.84	4.16	4.18	4.30	3.78
MnO	0.13	0.13	0.17	0.12	0.10	0.14	0.15	0.17	0.13
NiO	0.09	0.07	0.04	0.05	0.03	0.05	0.03	0.07	0.10
MgO	16.29	15.80	17.58	15.71	16.04	15.83	16.03	16.07	15.91
CaO	23.40	22.70	19.20	23.06	22.91	23.03	22.85	23.19	23.26
Na2O	0.30	0.36	0.27	0.38	0.44	0.39	0.36	0.31	0.34
Total	100.92	100.22	99.57	100.50	100.70	100.82	100.02	101.01	100.21
Si	1.95	1.94	1.94	1.95	1.95	1.94	1.95	1.95	1.94
Ti	0.01	0.01	0.01	0.01	0.01	0.00	0.01	0.01	0.01
Al	0.07	0.09	0.09	0.08	0.08	0.10	0.09	0.08	0.09
Cr	0.02	0.03	0.02	0.02	0.03	0.02	0.02	0.02	0.02
Fe	0.13	0.15	0.20	0.14	0.14	0.15	0.13	0.14	0.13
Mn	0.00	0.00	0.01	0.00	0.00	0.00	0.00	0.01	0.00
Ni	0.00	0.00	0.00	0.00	0.00	0.00	0.00	0.00	0.00
Mg	0.88	0.86	0.96	0.85	0.87	0.86	0.88	0.87	0.87
Ca	0.91	0.89	0.76	0.90	0.90	0.90	0.90	0.90	0.91
Na	0.02	0.03	0.02	0.03	0.03	0.03	0.03	0.02	0.02
total	4.00	4.00	4.00	4.00	4.01	4.01	4.00	4.00	4.00
Mg#	87	86	83	86	86	86	87	86	87
Wo	47	47	39	48	47	47	47	47	48
En	46	45	50	45	46	45	46	45	45
Fs	7	8	10	7	8	8	7	7	7

Table B3 Continued, clinopyroxene composistions from the Reef pyroxenites, Merensky Reef, Winnaarshoek.

Depth (m)	194.6	194.6	194.6	194.6	194.6	194.6	194.6	194.6	194.6	194.6	194.6
Sample	R8_cpx_1	R8_cpx_2	R8_cpx_3	R8_cpx_4	R8_cpx_5	R8_cpx_6	R8_cpx_7	R8_cpx_8	R8_cpx_9	R8_cpx_10	R8_cpx_11
SiO2	52.90	52.59	52.73	53.95	53.40	53.23	53.69	53.81	53.75	53.82	54.70
TiO2	0.42	0.45	0.45	0.36	0.47	0.37	0.44	0.37	0.38	0.28	0.27
Al2O3	2.08	2.17	2.06	1.92	2.07	2.13	1.67	1.53	1.58	1.35	1.31
Cr2O3	0.79	0.94	0.82	0.75	0.83	0.79	0.68	0.70	0.67	0.67	0.72
Fe2O3	0.04	1.14	0.96	0.00	0.47	0.25	0.26	0.52	0.02	1.23	0.00
FeO	6.38	3.73	3.64	4.69	4.41	4.45	4.17	3.44	4.66	3.28	3.53
MnO	0.18	0.12	0.16	0.10	0.15	0.13	0.13	0.13	0.14	0.14	0.10
NiO	0.01	0.05	0.04	0.09	0.08	0.06	0.12	0.06	0.03	0.08	0.05
MgO	17.46	15.72	15.98	15.87	15.84	15.73	16.10	16.40	16.20	16.42	16.43
CaO	18.97	22.93	22.63	22.92	22.92	22.98	23.24	23.54	22.86	23.35	23.88
Na2O	0.36	0.43	0.46	0.41	0.44	0.41	0.37	0.36	0.35	0.42	0.35
Total	99.58	100.26	99.92	101.05	101.08	100.52	100.88	100.84	100.64	101.03	101.33
Si	1.94	1.93	1.94	1.96	1.94	1.94	1.95	1.96	1.96	1.96	1.97
Ti	0.01	0.01	0.01	0.01	0.01	0.01	0.01	0.01	0.01	0.01	0.01
Al	0.09	0.09	0.09	0.08	0.09	0.09	0.07	0.07	0.07	0.06	0.06
Cr	0.02	0.03	0.02	0.02	0.02	0.02	0.02	0.02	0.02	0.02	0.02
Fe	0.20	0.15	0.14	0.14	0.15	0.14	0.13	0.12	0.14	0.13	0.11
Mn	0.01	0.00	0.01	0.00	0.00	0.00	0.00	0.00	0.00	0.00	0.00
Ni	0.00	0.00	0.00	0.00	0.00	0.00	0.00	0.00	0.00	0.00	0.00
Mg	0.96	0.86	0.88	0.86	0.86	0.86	0.87	0.89	0.88	0.89	0.88
Ca	0.75	0.90	0.89	0.89	0.89	0.90	0.91	0.92	0.89	0.91	0.92
Na	0.03	0.03	0.03	0.03	0.03	0.03	0.03	0.03	0.02	0.03	0.02
total	4.00	4.01	4.01	4.00	4.00	4.00	4.00	4.00	4.00	4.01	4.00
Mg#	83	86	86	86	85	86	87	88	86	87	89
Wo	39	47	47	47	47	47	47	48	46	47	48
En	50	45	46	45	45	45	46	46	46	46	46
Fs	11	8	8	8	8	8	7	6	8	7	6

Table B3 Continued, clinopyroxene composistions from the Reef pyroxenites, Merensky Reef, Winnaarshoek.

194.6	194.6	194.6	194.6	194.6	194.6	194.6	194.6	194.6	194.6	194.6
R8_cpx_12	R8_cpx_13	R8_cpx_14	R8_cpx_15	R8_cpx_16	R8_cpx_17	R8_cpx_18	R8_cpx_19	R8_cpx_20	R8_cpx_21	R8_cpx_22
54.50	53.75	53.48	54.02	54.17	53.94	54.13	53.43	53.37	54.69	53.51
0.27	0.28	0.29	0.26	0.28	0.23	0.26	0.48	0.50	0.34	0.53
1.40	1.75	1.48	1.50	1.39	1.55	1.62	2.08	1.97	1.64	1.96
0.74	0.72	0.82	0.70	0.66	0.75	0.76	0.78	0.77	0.74	0.76
0.67	0.00	0.00	0.06	0.00	0.38	0.00	0.69	0.00	0.00	0.17
3.76	4.43	4.27	4.30	4.60	3.67	4.27	4.25	5.09	8.11	4.14
0.14	0.16	0.14	0.13	0.15	0.12	0.10	0.14	0.12	0.17	0.16
0.07	0.04	0.05	0.05	0.06	0.06	0.11	0.10	0.04	0.08	0.04
16.55	16.27	16.29	16.22	16.43	16.49	16.33	16.03	15.81	20.45	16.04
23.71	22.81	22.60	23.36	22.98	23.18	23.06	22.72	22.52	14.64	23.15
0.34	0.33	0.37	0.32	0.29	0.38	0.36	0.46	0.41	0.28	0.41
102.15	100.52	99.79	100.93	101.01	100.74	100.98	101.16	100.58	101.14	100.86
1.96	1.96	1.96	1.96	1.96	1.96	1.96	1.94	1.95	1.96	1.95
0.01	0.01	0.01	0.01	0.01	0.01	0.01	0.01	0.01	0.01	0.01
0.06	0.08	0.06	0.06	0.06	0.07	0.07	0.09	0.08	0.07	0.08
0.02	0.02	0.02	0.02	0.02	0.02	0.02	0.02	0.02	0.02	0.02
0.13	0.13	0.13	0.13	0.14	0.12	0.13	0.15	0.16	0.24	0.13
0.00	0.00	0.00	0.00	0.00	0.00	0.00	0.00	0.00	0.01	0.00
0.00	0.00	0.00	0.00	0.00	0.00	0.00	0.00	0.00	0.00	0.00
0.89	0.88	0.89	0.88	0.89	0.89	0.88	0.87	0.86	1.09	0.87
0.91	0.89	0.89	0.91	0.89	0.90	0.90	0.88	0.88	0.56	0.90
0.02	0.02	0.03	0.02	0.02	0.03	0.03	0.03	0.03	0.02	0.03
4.01	4.00	4.00	4.00	4.00	4.00	4.00	4.01	4.00	3.99	4.00
87	87	87	87	86	88	87	85	85	82	87
47	47	46	47	46	47	47	46	46	30	47
46	46	47	46	46	46	46	46	45	57	46
7	7	7	7	7	7	7	8	8	13	7

Table B4 Clinopyroxene composistions from the footwall leuconorites, Merensky Reef, Winnaarshoek.

Depth (m)	198.5	198.5	198.5	198.5	198.5	198.5	198.5	198.5	198.5
Sample	Wh31_7_127	Wh31_7_128	Wh31_7_129	Wh31_7_130	Wh31_7_131	Wh31_7_132	Wh31_7_133	Wh31_7_134	Wh31_7_135
SiO2	52.69	52.50	52.53	52.98	52.57	52.16	52.63	53.02	52.51
TiO2	0.20	0.27	0.23	0.28	0.30	0.26	0.24	0.28	0.25
Al2O3	1.99	2.18	1.84	2.00	1.77	2.02	1.95	1.74	1.67
Cr2O3	0.77	0.82	0.13	0.79	0.77	0.10	0.12	0.72	0.12
Fe2O3	0.43	0.00	0.00	0.00	0.03	0.39	0.00	0.09	0.00
FeO	3.82	4.50	4.09	4.21	4.20	4.16	4.51	3.99	3.96
MnO	0.15	0.13	0.20	0.13	0.15	0.18	0.17	0.18	0.12
NiO	0.00	0.00	0.00	0.00	0.00	0.00	0.00	0.00	0.00
MgO	15.90	15.67	15.68	15.78	16.02	16.20	15.77	16.09	15.95
CaO	23.87	23.49	23.55	23.67	23.39	22.89	23.44	23.86	23.03
Na2O	0.06	0.06	0.02	0.06	0.06	0.01	0.05	0.05	0.06
Total	99.88	99.62	98.26	99.89	99.25	98.39	98.86	100.02	97.68
Si	1.94	1.94	1.96	1.95	1.94	1.94	1.95	1.95	1.96
Ti	0.01	0.01	0.01	0.01	0.01	0.01	0.01	0.01	0.01
Al	0.09	0.09	0.08	0.09	0.08	0.09	0.09	0.08	0.07
Cr	0.02	0.02	0.00	0.02	0.02	0.00	0.00	0.02	0.00
Fe	0.13	0.14	0.13	0.13	0.13	0.14	0.14	0.13	0.12
Mn	0.00	0.00	0.01	0.00	0.00	0.01	0.01	0.01	0.00
Ni	0.00	0.00	0.00	0.00	0.00	0.00	0.00	0.00	0.00
Mg	0.87	0.86	0.87	0.86	0.88	0.90	0.87	0.88	0.89
Ca	0.94	0.93	0.94	0.93	0.93	0.91	0.93	0.94	0.92
Na	0.00	0.00	0.00	0.00	0.00	0.00	0.00	0.00	0.00
total	4.00	4.00	3.99	3.99	4.00	4.00	4.00	4.00	3.99
Mg#	87	86	87	87	87	86	86	88	88
Wo	48	48	48	48	48	47	48	48	48
En	45	45	45	45	45	46	45	45	46
Fs	7	7	7	7	7	7	7	7	7

Table B4 Continued, clinopyroxene composistions from the footwall leuconorites, Merensky Reef, Winnaarshoek.

198.5	198.5	198.5	198.5	198.5	198.5	200	200	200
Wh31_7_139	Wh31_7_140	Wh31_7_141	Wh31_7_142	Wh31_7_143	Wh31_7_144	Wh31_8_25a	Wh31_7_27a	Wh31_7_28a
53.16	52.91	52.46	52.49	53.06	53.37	53.56	53.46	53.95
0.33	0.21	0.43	0.35	0.30	0.32	0.29	0.26	0.25
1.99	1.82	1.93	1.62	1.58	1.76	1.59	1.60	1.32
0.64	0.09	0.67	0.07	0.12	0.59	0.63	0.63	0.52
0.00	0.00	0.00	0.00	0.00	0.00	0.00	0.00	0.00
6.15	4.02	4.22	4.16	3.97	4.35	3.62	3.93	3.90
0.18	0.13	0.15	0.13	0.16	0.13	0.16	0.18	0.14
0.00	0.00	0.00	0.00	0.00	0.00	0.00	0.00	0.00
17.64	16.08	15.63	15.89	16.05	16.25	16.60	16.50	16.46
19.50	23.53	23.36	23.45	23.27	23.85	23.41	23.52	22.90
0.03	0.00	0.00	0.06	0.00	0.01	0.09	0.00	0.04
99.61	98.78	98.86	98.21	98.50	100.62	99.95	100.07	99.48
1.95	1.96	1.95	1.96	1.97	1.95	1.96	1.95	1.98
0.01	0.01	0.01	0.01	0.01	0.01	0.01	0.01	0.01
0.09	0.08	0.08	0.07	0.07	0.08	0.07	0.07	0.06
0.02	0.00	0.02	0.00	0.00	0.02	0.02	0.02	0.01
0.19	0.12	0.13	0.13	0.12	0.13	0.11	0.12	0.12
0.01	0.00	0.00	0.00	0.00	0.00	0.01	0.01	0.00
0.00	0.00	0.00	0.00	0.00	0.00	0.00	0.00	0.00
0.96	0.89	0.86	0.88	0.89	0.88	0.90	0.90	0.90
0.77	0.93	0.93	0.94	0.92	0.93	0.92	0.92	0.90
0.00	0.00	0.00	0.00	0.00	0.00	0.01	0.00	0.00
3.99	3.99	3.99	4.00	3.99	4.00	3.99	3.99	3.98
84	88	87	87	88	87	89	88	88
40	48	48	48	48	48	47	47	47
50	46	45	45	46	45	47	46	47
10	7	7	7	7	7	6	6	6

Table B5 Continued, clinopyroxene composistions from the footwall leuconorites, Merensky Reef, Winnaarshoek.

200	200	200	200	200	200	200	200	200
Wh31_7_29a	Wh31_7_30a	Wh31_7_31a	Wh31_7_34a	Wh31_7_35a	Wh31_7_39a	Wh31_7_40a	Wh31_7_41a	Wh31_7_42a
54.12	54.29	53.89	54.08	53.86	53.69	53.77	54.11	53.56
0.17	0.25	0.25	0.28	0.24	0.31	0.22	0.28	0.30
1.33	1.19	1.38	1.44	1.25	1.41	1.65	1.43	1.47
0.68	0.55	0.67	0.10	0.51	0.65	0.74	0.11	0.60
0.00	0.00	0.00	0.00	0.00	0.00	0.00	0.00	0.00
3.81	3.59	3.92	3.72	3.58	3.73	3.82	3.73	4.47
0.11	0.11	0.17	0.09	0.09	0.20	0.10	0.19	0.20
0.00	0.00	0.00	0.00	0.00	0.00	0.00	0.00	0.00
16.66	17.05	16.47	16.55	16.57	16.54	16.41	16.33	16.76
23.72	23.60	23.74	23.71	24.05	23.52	23.14	23.38	22.31
0.02	0.04	0.00	0.00	0.06	0.02	0.06	0.00	0.02
100.61	100.67	100.49	99.96	100.20	100.06	99.91	99.55	99.69
1.97	1.97	1.96	1.97	1.96	1.96	1.96	1.98	1.96
0.00	0.01	0.01	0.01	0.01	0.01	0.01	0.01	0.01
0.06	0.05	0.06	0.06	0.05	0.06	0.07	0.06	0.06
0.02	0.02	0.02	0.00	0.01	0.02	0.02	0.00	0.02
0.12	0.11	0.12	0.11	0.11	0.11	0.12	0.11	0.14
0.00	0.00	0.01	0.00	0.00	0.01	0.00	0.01	0.01
0.00	0.00	0.00	0.00	0.00	0.00	0.00	0.00	0.00
0.90	0.92	0.89	0.90	0.90	0.90	0.89	0.89	0.92
0.92	0.92	0.93	0.93	0.94	0.92	0.91	0.92	0.88
0.00	0.00	0.00	0.00	0.00	0.00	0.00	0.00	0.00
3.99	3.99	3.99	3.99	4.00	3.99	3.99	3.98	3.99
89	89	88	89	89	89	88	89	87
47	47	48	48	48	47	47	48	45
46	47	46	46	46	46	47	46	47
6	6	6	6	6	6	6	6	7

Table B5 Clinopyroxene composistions from the footwall anorthosites, Merensky Reef, Winnaarshoek.

Depth (m)	202	202	202	202	202	202	202	202	202.1
Sample	WH31_9_09	WH31_9_10	WH31_9_11	WH31_9_12	WH31_9_13	WH31_9_14	WH31_9_15	WH31_9_16	WH31_10_17
SiO2	53.07	53.99	53.68	54.16	53.97	53.73	53.14	53.06	52.99
TiO2	0.27	0.27	0.30	0.29	0.26	0.34	0.22	0.21	0.25
Al2O3	1.81	1.57	1.48	1.69	1.71	1.70	1.89	1.57	1.58
Cr2O3	0.66	0.58	0.52	0.53	0.58	0.61	0.74	0.64	0.11
Fe2O3	0.00	0.00	0.00	0.00	0.00	0.00	0.00	1.01	0.13
FeO	3.74	4.61	4.19	4.07	6.19	4.23	4.17	3.16	3.68
MnO	0.14	0.17	0.11	0.14	0.19	0.11	0.17	0.15	0.09
NiO	0.00	0.00	0.00	0.00	0.00	0.00	0.00	0.00	0.00
MgO	17.12	15.97	15.85	15.54	20.72	16.02	17.10	17.54	16.21
CaO	22.20	23.14	23.87	24.25	16.36	23.96	22.15	22.51	23.96
Na2O	0.00	0.05	0.04	0.03	0.00	0.05	0.05	0.05	0.05
Total	99.01	100.35	100.03	100.70	99.98	100.75	99.63	99.89	99.04
Si	1.95	1.97	1.97	1.97	1.95	1.95	1.95	1.94	1.96
Ti	0.01	0.01	0.01	0.01	0.01	0.01	0.01	0.01	0.01
Al	0.08	0.07	0.06	0.07	0.07	0.07	0.08	0.07	0.07
Cr	0.02	0.02	0.01	0.02	0.02	0.02	0.02	0.02	0.00
Fe	0.11	0.14	0.13	0.12	0.19	0.13	0.13	0.12	0.12
Mn	0.00	0.01	0.00	0.00	0.01	0.00	0.01	0.00	0.00
Ni	0.00	0.00	0.00	0.00	0.00	0.00	0.00	0.00	0.00
Mg	0.94	0.87	0.87	0.84	1.12	0.87	0.93	0.96	0.89
Ca	0.88	0.90	0.94	0.94	0.63	0.93	0.87	0.88	0.95
Na	0.00	0.00	0.00	0.00	0.00	0.00	0.00	0.00	0.00
total	3.99	3.98	3.99	3.98	4.00	3.99	4.00	4.01	4.00
Mg#	89	86	87	87	86	87	88	88	88
Wo	45	47	48	49	33	48	45	45	48
En	49	45	45	44	57	45	48	49	46
Fs	6	8	7	7	10	7	7	7	6

Table B5 Continued, clinopyroxene composistions from the footwall anorthosites, Merensky Reef, Winnaarshoek.

202.1	202.1	202.1	202.1	202.2	202.2	202.2	202.2	202.2	202.2
WH31_10_18	WH31_10_19	WH31_10_20	WH31_10_21	WH31_11_22	WH31_11_23	WH31_11_24	WH31_11_25	WH31_11_26	WH31_11_27
52.83	53.63	52.86	53.24	53.63	53.93	53.36	53.79	53.72	53.07
0.21	0.25	0.25	0.26	0.31	0.27	0.28	0.24	0.25	0.22
1.74	1.48	1.47	1.61	1.32	1.16	1.45	1.25	1.41	1.87
0.10	0.48	0.39	0.08	0.52	0.51	0.62	0.52	0.49	0.50
0.68	0.00	0.44	0.00	0.00	0.00	0.00	0.00	0.00	0.00
3.36	3.83	2.61	3.53	3.97	4.05	4.02	4.37	4.14	4.48
0.14	0.11	0.15	0.09	0.16	0.14	0.17	0.17	0.13	0.19
0.00	0.00	0.00	0.00	0.00	0.00	0.00	0.00	0.00	0.00
16.19	16.33	16.17	16.20	16.46	16.65	16.37	16.99	16.56	15.96
24.20	23.97	24.83	24.07	23.50	23.42	23.24	22.66	23.46	23.03
0.00	0.08	0.01	0.07	0.00	0.03	0.03	0.02	0.00	0.00
99.45	100.16	99.18	99.14	99.86	100.15	99.55	100.02	100.16	99.32
1.95	1.96	1.95	1.96	1.96	1.97	1.96	1.97	1.96	1.96
0.01	0.01	0.01	0.01	0.01	0.01	0.01	0.01	0.01	0.01
0.08	0.06	0.06	0.07	0.06	0.05	0.06	0.05	0.06	0.08
0.00	0.01	0.01	0.00	0.02	0.01	0.02	0.01	0.01	0.01
0.12	0.12	0.09	0.11	0.12	0.12	0.12	0.13	0.13	0.14
0.00	0.00	0.00	0.00	0.00	0.00	0.01	0.01	0.00	0.01
0.00	0.00	0.00	0.00	0.00	0.00	0.00	0.00	0.00	0.00
0.89	0.89	0.89	0.89	0.90	0.91	0.90	0.93	0.90	0.88
0.96	0.94	0.98	0.95	0.92	0.92	0.92	0.89	0.92	0.91
0.00	0.01	0.00	0.00	0.00	0.00	0.00	0.00	0.00	0.00
4.01	4.00	4.00	4.00	3.99	3.99	3.99	3.99	3.99	3.99
88	88	91	89	88	88	88	87	88	86
48	48	50	49	47	47	47	45	47	47
45	46	45	46	46	46	46	47	46	45
6	6	5	6	6	7	7	7	7	7

Appendix C- Plagioclase compositions (EPMA) from the Merensky Reef at Winnaarshoek

Table C1 Plagioclase compositions from the hanging wall anorthosites, Merensky Reef, Winnaarshoek.

Depth (m)	182	182	182	182	182	182	182	188.8	188.8	182	182	182	182	182
Sample	1a-core	3a-core	4a-core	6a-core	9a-core	11a-core	13a-core	14a-core	16a-core	2a-rim	5a-rim	7a-rim	10a-rim	12a-rim
SiO2	50.40	49.56	49.55	49.47	49.18	47.95	48.74	49.01	48.99	48.01	49.30	48.70	48.20	48.90
Al2O3	31.83	32.83	32.20	32.22	31.75	32.29	32.00	31.59	31.65	34.11	32.48	32.63	32.03	31.96
FeO	0.07	0.10	0.13	0.06	0.12	0.08	0.08	0.10	0.09	0.06	0.19	0.05	0.07	0.16
CaO	14.80	15.27	15.10	15.27	14.88	15.48	15.14	15.05	14.70	16.78	15.78	16.02	15.35	15.09
Na2O	3.11	2.44	2.77	2.71	2.74	2.28	2.51	2.60	2.69	2.00	2.56	2.42	2.36	2.51
K2O	0.13	0.20	0.18	0.17	0.17	0.13	0.16	0.19	0.18	0.06	0.17	0.15	0.13	0.17
BaO	0.00	0.00	0.00	0.00	0.00	0.02	0.00	0.00	0.00	0.00	0.00	0.00	0.00	0.01
Total	100.34	100.40	99.93	99.90	98.84	98.23	98.64	98.54	98.29	101.01	100.48	99.97	98.15	98.80
Si	2.29	2.25	2.26	2.26	2.27	2.23	2.26	2.27	2.27	2.18	2.24	2.23	2.24	2.26
Al	1.70	1.76	1.73	1.74	1.73	1.77	1.75	1.72	1.73	1.82	1.74	1.76	1.76	1.74
Fe	0.00	0.00	0.01	0.00	0.00	0.00	0.00	0.00	0.00	0.00	0.01	0.00	0.00	0.01
Ca	0.72	0.74	0.74	0.75	0.74	0.77	0.75	0.75	0.73	0.82	0.77	0.79	0.77	0.75
Na	0.27	0.22	0.25	0.24	0.25	0.21	0.23	0.23	0.24	0.18	0.23	0.21	0.21	0.22
K	0.01	0.01	0.01	0.01	0.01	0.01	0.01	0.01	0.01	0.00	0.01	0.01	0.01	0.01
Ba	0.00	0.00	0.00	0.00	0.00	0.00	0.00	0.00	0.00	0.00	0.00	0.00	0.00	0.00
Total	5.00	4.98	5.00	5.00	4.99	4.99	4.99	4.99	4.99	5.00	5.00	5.00	4.99	4.99
Ab	27	22	25	24	25	21	23	24	25	18	22	21	22	23
An	72	77	74	75	74	78	76	75	74	82	77	78	78	76
Or	1	1	1	1	1	1	1	1	1	0	1	1	1	1

Table C2 Plagioclase compositions from the footwall leuconorites, Merensky Reef, Winnaarshoek.

Depth (m)	190.8	190.8	190.8	190.8	190.8	190.8	191.5	191.5	191.5
Sample	04_20a-core	04_21a-core	04_23a-core	04_24a-core	04_26a-core	04_28a-core	05_70-core	05_71-core	05_74-core
SiO2	50.79	52.57	49.53	49.50	49.30	49.97	52.03	52.19	50.60
Al2O3	31.72	30.83	32.30	32.63	32.54	32.26	31.29	30.49	32.01
FeO	0.07	0.07	0.05	0.10	0.10	0.07	0.01	0.09	0.05
CaO	14.65	13.07	15.44	16.01	15.44	15.19	13.85	13.28	14.58
Na2O	3.11	3.71	2.52	2.45	2.65	2.65	3.68	3.97	3.17
K2O	0.20	0.17	0.16	0.15	0.17	0.17	0.28	0.28	0.21
BaO	0.00	0.02	0.02	0.00	0.00	0.00	0.00	0.00	0.00
Total	100.54	100.44	100.01	100.84	100.21	100.30	101.13	100.29	100.63
Si	2.30	2.37	2.26	2.25	2.25	2.27	2.34	2.36	2.29
Al	1.69	1.64	1.74	1.74	1.75	1.73	1.66	1.63	1.71
Fe	0.00	0.00	0.00	0.00	0.00	0.00	0.00	0.00	0.00
Ca	0.71	0.63	0.75	0.78	0.75	0.74	0.67	0.64	0.71
Na	0.27	0.32	0.22	0.22	0.23	0.23	0.32	0.35	0.28
K	0.01	0.01	0.01	0.01	0.01	0.01	0.02	0.02	0.01
Ba	0.00	0.00	0.00	0.00	0.00	0.00	0.00	0.00	0.00
Total	4.99	4.98	4.99	4.99	5.00	4.99	5.00	5.00	5.00
Ab	27	34	23	21	23	24	32	35	28
An	71	65	76	78	76	75	66	64	71
Or	1	1	1	1	1	1	2	2	1

Table C2 Continued, plagioclase composistions from the footwall leuconorites, Merensky Reef, Winnaarshoek.

191.5	191.5	191.5	191.5	190.8	190.8	190.8	190.8	190.8
05_75-core	05_76-core	05_77-core	05_78-core	04_22a-rim	04_24a-rim	04_25a-rim	04_27a-rim	04_29a-rim
51.12	50.61	52.87	50.86	49.30	49.50	49.49	48.09	49.90
31.38	31.83	30.98	32.09	32.25	32.63	32.77	33.04	32.15
0.01	0.08	0.07	0.05	0.10	0.10	0.05	0.12	0.09
14.37	14.36	13.16	14.53	15.46	16.01	16.09	16.56	15.06
3.39	3.14	3.46	3.39	2.53	2.45	2.31	2.09	2.65
0.26	0.20	0.28	0.22	0.15	0.15	0.15	0.11	0.16
0.03	0.00	0.02	0.00	0.00	0.00	0.00	0.00	0.00
100.56	100.23	100.83	101.14	99.79	100.84	100.85	100.01	100.00
2.32	2.30	2.37	2.29	2.26	2.25	2.24	2.20	2.27
1.68	1.70	1.64	1.70	1.74	1.74	1.75	1.79	1.73
0.00	0.00	0.00	0.00	0.00	0.00	0.00	0.00	0.00
0.70	0.70	0.63	0.70	0.76	0.78	0.78	0.81	0.74
0.30	0.28	0.30	0.30	0.22	0.22	0.20	0.19	0.23
0.02	0.01	0.02	0.01	0.01	0.01	0.01	0.01	0.01
0.00	0.00	0.00	0.00	0.00	0.00	0.00	0.00	0.00
5.00	4.99	4.97	5.01	4.99	4.99	4.99	5.00	4.98
29	28	32	29	23	21	20	19	24
69	71	67	69	76	78	79	81	75
2	1	2	1	1	1	1	1	1

Table C3 Plagioclase compositions from the Reef pyroxenites, Merensky Reef, Winnaarshoek.

Depth (m)	192.1	192.1	192.1	192.1	192.1	192.1	192.1	192.1	192.1	192.1
Sample	R1-plag1-incl	R1-plag1-incl	R1-plag1-incl	R1-plag1-incl	R1-plag2	R1-plag2	R1-plag2	R1-plag3- co1	R1-plag3- rim1	R1-plag- incl1
SiO2	52.67	51.31	50.90	50.86	50.68	51.04	51.11	51.66	51.73	51.76
Al2O3	30.31	31.01	31.16	31.00	31.00	31.02	30.78	30.73	30.54	30.51
FeO	0.24	0.17	0.35	0.24	0.19	0.23	0.30	0.41	0.31	0.47
CaO	12.09	13.25	12.95	13.18	13.07	13.27	13.14	12.79	12.49	12.62
Na2O	4.05	3.54	3.56	3.56	3.58	3.50	3.76	3.84	3.98	3.82
K2O	0.42	0.36	0.38	0.34	0.38	0.37	0.37	0.39	0.37	0.28
BaO	0.02	0.01	0.01	0.02	0.01	0.03	0.01	0.04	0.03	0.02
Total	99.79	99.66	99.32	99.19	98.90	99.47	99.45	99.85	99.45	99.48
Si	2.29	2.39	2.34	2.33	2.33	2.33	2.33	2.34	2.35	2.36
Al	1.71	1.62	1.67	1.68	1.67	1.68	1.67	1.66	1.65	1.64
Fe	0.02	0.01	0.01	0.01	0.01	0.01	0.01	0.01	0.02	0.01
Ca	0.69	0.59	0.65	0.64	0.65	0.64	0.65	0.64	0.62	0.61
Na	0.27	0.36	0.31	0.32	0.32	0.32	0.31	0.33	0.34	0.35
K	0.01	0.02	0.02	0.02	0.02	0.02	0.02	0.02	0.02	0.02
Ba	0.00	0.00	0.00	0.00	0.00	0.00	0.00	0.00	0.00	0.00
Total	4.99	4.99	4.99	5.00	5.00	5.00	5.00	5.01	5.00	5.00
Ab	37	32	32	32	32	32	33	34	36	35
An	61	66	65	66	65	66	64	63	62	64
Or	2	2	2	2	2	2	2	2	2	2

Table C3 Continued, Plagioclase compositions from the Reef pyroxenites, Merensky Reef, Winnaarshoek.

192.1	192.1	192.1	192.1	192.1	192.1	192.1	192.1
R1-plag- incl2	R1-plag2	R1-plag2	R1-plag2	R1-plag2	R1-plag1	R1-plag2	R1-plag3
52.18	50.92	51.44	51.18	51.29	51.15	50.07	50.96
30.27	30.98	30.98	30.79	31.16	30.94	31.61	31.06
0.14	0.29	0.26	0.15	0.36	0.14	0.22	0.19
12.27	13.10	13.02	12.84	13.24	12.87	13.55	13.02
4.06	3.73	3.57	3.69	3.60	3.84	3.37	3.79
0.31	0.32	0.35	0.32	0.33	0.25	0.23	0.27
0.00	0.02	0.06	0.04	0.01	0.01	0.00	0.00
99.23	99.36	99.67	99.01	99.99	99.20	99.05	99.29
2.36	2.38	2.33	2.34	2.35	2.33	2.34	2.30
1.64	1.63	1.67	1.66	1.66	1.67	1.67	1.71
0.02	0.01	0.01	0.01	0.01	0.01	0.01	0.01
0.62	0.60	0.64	0.64	0.63	0.65	0.63	0.67
0.34	0.36	0.33	0.32	0.33	0.32	0.34	0.30
0.02	0.02	0.02	0.02	0.02	0.02	0.01	0.01
0.00	0.00	0.00	0.00	0.00	0.00	0.00	0.00
4.99	4.99	5.01	4.99	4.99	5.00	5.00	5.00
37	33	32	34	32	35	31	34
61	65	65	64	66	64	68	64
2	2	2	2	2	1	1	2

Table C3 Continued, Plagioclase compositions from the Reef pyroxenites, Merensky Reef, Winnaarshoek.

Depth (m)	194.9	194.9	194.9	194.9	194.9	194.9	194.9	194.9	194.9	194.9
Sample	R7-1- plag1	R7-1- plag1	R7-1- plag1	R7-1- plag1	R7-1- plag1	R7-1- plag2	R7-1- plag2	R7-1- plag2	R7-1- plag2	R7-2- plag1
SiO2	53.07	53.11	53.41	53.63	53.28	53.01	52.39	52.72	52.90	52.34
Al2O3	29.50	29.64	29.08	29.84	29.58	30.25	30.12	29.81	29.83	29.79
FeO	0.25	0.22	0.24	0.08	0.20	0.00	0.29	0.34	0.37	0.43
CaO	11.79	11.82	11.52	11.74	11.55	11.98	12.30	11.82	12.01	11.85
Na2O	4.28	4.28	4.47	4.46	4.50	4.12	3.97	4.15	4.18	4.11
K2O	0.40	0.40	0.43	0.37	0.42	0.35	0.36	0.39	0.38	0.33
BaO	0.02	0.02	0.03	0.03	0.02	0.04	0.03	0.04	0.03	0.01
Total	99.31	99.49	99.18	100.14	99.56	99.76	99.45	99.26	99.70	98.85
Si	2.41	2.42	2.42	2.44	2.42	2.42	2.40	2.39	2.40	2.40
Al	1.59	1.58	1.59	1.56	1.59	1.58	1.62	1.62	1.60	1.60
Fe	0.00	0.01	0.01	0.01	0.00	0.01	0.00	0.01	0.01	0.01
Ca	0.58	0.58	0.58	0.56	0.57	0.56	0.58	0.60	0.58	0.58
Na	0.38	0.38	0.38	0.39	0.39	0.40	0.36	0.35	0.37	0.37
K	0.02	0.02	0.02	0.02	0.02	0.02	0.02	0.02	0.02	0.02
Ba	0.00	0.00	0.00	0.00	0.00	0.00	0.00	0.00	0.00	0.00
Total	4.99	4.99	4.99	4.99	4.99	5.00	4.98	4.99	4.99	4.99
Ab	39	39	40	40	40	38	36	38	38	38
An	59	59	57	58	57	60	62	60	60	60
Or	2	2	3	2	2	2	2	2	2	2

Table C3 Continued, Plagioclase composistions from the Reef pyroxenites, Merensky Reef, Winnaarshoek.

194.9	194.9	194.9	194.9	194.9	194.9	194.9	194.9	194.9	194.9	194.9
R7-2- plag1	R7-2- plag1	R7-2- plag1	R7-3- plag1	R7-3- plag1	R7-3- plag1	R7-3- plag1	R7-3- plag2	R7-3- plag2	R7-3- plag2	R7-3- plag2
53.36	52.98	52.90	50.48	50.27	50.07	50.30	50.91	51.93	51.30	50.75
29.80	29.62	29.92	31.66	31.52	31.98	31.68	30.58	30.86	31.23	31.42
0.18	0.22	0.18	0.43	0.30	0.28	0.41	0.28	0.24	0.27	0.31
11.63	11.62	11.65	13.63	13.86	14.09	13.82	13.57	13.21	13.43	13.60
4.38	4.35	4.41	3.04	3.14	3.14	3.25	3.51	3.57	3.54	3.42
0.32	0.30	0.30	0.29	0.28	0.27	0.25	0.38	0.33	0.33	0.32
0.03	0.04	0.01	0.03	0.02	0.01	0.00	0.01	0.01	0.03	0.04
99.69	99.14	99.36	99.55	99.38	99.83	99.71	99.24	100.15	100.12	99.85
2.40	2.42	2.42	2.41	2.31	2.30	2.29	2.30	2.34	2.35	2.33
1.61	1.59	1.59	1.60	1.71	1.70	1.72	1.71	1.65	1.65	1.67
0.02	0.01	0.01	0.01	0.02	0.01	0.01	0.02	0.01	0.01	0.01
0.58	0.56	0.57	0.57	0.67	0.68	0.69	0.68	0.67	0.64	0.65
0.37	0.38	0.38	0.39	0.27	0.28	0.28	0.29	0.31	0.31	0.31
0.02	0.02	0.02	0.02	0.02	0.02	0.02	0.01	0.02	0.02	0.02
0.00	0.00	0.00	0.00	0.00	0.00	0.00	0.00	0.00	0.00	0.00
4.99	4.99	4.99	4.99	4.98	4.99	5.00	5.00	5.00	4.99	5.00
40	40	40	28	29	28	29	31	32	32	31
58	59	58	70	70	70	69	67	66	66	67
2	2	2	2	2	2	2	2	2	2	2

Table C3 Continued, Plagioclase composistions from the Reef pyroxenites, Merensky Reef, Winnaarshoek.

Depth (m)	194.6	194.6	194.6	194.6	194.6	194.6	194.6	194.6	194.6	194.6	194.6
Sample	R8-2-plag1	R8-2-plag1	R8-2-plag1	R8-2-plag1	R8-2_co1	R8-2-plag3	R8-2-plag3	R8-2-plag3	R8-2-plag3	R8-31_co1	R8-3_co2
SiO2	52.57	53.23	52.53	53.00	53.20	53.59	53.05	52.40	53.08	51.93	51.85
Al2O3	30.23	30.03	30.67	30.14	29.82	29.43	29.85	29.95	29.87	31.04	30.77
FeO	0.18	0.23	0.45	0.07	0.40	0.18	0.20	0.12	0.07	0.04	0.10
CaO	12.05	11.66	12.56	11.86	12.02	11.26	11.83	11.56	11.81	13.02	12.98
Na2O	4.24	4.44	4.10	4.25	4.33	4.60	4.37	4.33	4.28	3.64	3.78
K2O	0.31	0.32	0.28	0.28	0.34	0.40	0.39	0.29	0.32	0.30	0.30
BaO	0.04	0.04	0.03	0.02	0.01	0.00	0.01	0.01	0.02	0.00	0.02
Total	99.63	99.95	100.62	99.62	100.11	99.46	99.71	98.66	99.45	99.96	99.78
Si	2.39	2.41	2.37	2.40	2.41	2.43	2.43	2.41	2.40	2.41	2.35
Al	1.62	1.60	1.63	1.61	1.59	1.58	1.58	1.60	1.62	1.60	1.66
Fe	0.01	0.01	0.02	0.00	0.02	0.01	0.01	0.01	0.00	0.00	0.00
Ca	0.59	0.57	0.61	0.58	0.58	0.55	0.55	0.58	0.57	0.57	0.63
Na	0.37	0.39	0.36	0.37	0.38	0.40	0.40	0.38	0.38	0.38	0.32
K	0.02	0.02	0.02	0.02	0.02	0.02	0.02	0.02	0.02	0.02	0.02
Ba	0.00	0.00	0.00	0.00	0.00	0.00	0.00	0.00	0.00	0.00	0.00
Total	5.00	4.99	5.00	4.99	5.00	4.99	4.99	5.00	4.99	4.99	4.98
Ab	38	40	36	39	39	41	39	40	39	33	34
An	60	58	62	60	59	56	59	59	59	65	64
Or	2	2	2	2	2	2	2	2	2	2	2

Table C4 Plagioclase compositions from the footwall leuconorites, Merensky Reef, Winnaarshoek.

Depth (m)	198.5	198.5	198.5	198.5	198.5	198.5	198.5	200	200	200
Sample	07_79-core	07_80-core	07_89-core	07_90-core	07_91-core	07_93-core	07_94-core	08_31-core	08_34-core	08_35-core
SiO2	49.97	52.86	49.90	50.25	53.26	52.31	52.85	49.78	49.37	49.12
Al2O3	31.99	30.22	32.12	32.28	30.05	30.64	30.08	32.53	32.67	32.98
FeO	0.02	0.05	0.04	0.06	0.04	0.03	0.03	0.09	0.11	0.07
CaO	14.87	12.34	14.52	14.90	12.44	13.17	12.48	15.31	15.31	15.76
Na2O	3.11	3.20	3.00	3.16	3.49	4.17	4.42	2.99	2.76	2.51
K2O	0.20	0.21	0.22	0.22	1.07	0.35	0.40	0.17	0.13	0.11
BaO	0.01	0.01	0.00	0.02	0.03	0.00	0.00	0.00	0.00	0.00
Total	100.17	98.89	99.79	100.89	100.38	100.67	100.26	100.87	100.35	100.55
Si	2.28	2.41	2.28	2.27	2.41	2.36	2.39	2.26	2.25	2.23
Al	1.72	1.62	1.73	1.72	1.60	1.63	1.60	1.74	1.75	1.77
Fe	0.00	0.00	0.00	0.00	0.00	0.00	0.00	0.00	0.00	0.00
Ca	0.73	0.60	0.71	0.72	0.60	0.64	0.60	0.74	0.75	0.77
Na	0.27	0.28	0.27	0.28	0.31	0.37	0.39	0.26	0.24	0.22
K	0.01	0.01	0.01	0.01	0.06	0.02	0.02	0.01	0.01	0.01
Ba	0.00	0.00	0.00	0.00	0.00	0.00	0.00	0.00	0.00	0.00
Total	5.01	4.93	5.00	5.01	4.98	5.02	5.01	5.01	5.00	5.00
Ab	27	31	27	27	32	36	38	26	24	22
An	72	67	72	71	62	62	60	73	75	77
Or	1	1	1	1	6	2	2	1	1	1

Table C4 Continued, Plagioclase composistions from the footwall leuconorites, Merensky Reef, Winnaarshoek.

200	200	200	200	200	200	200	198.5	198.5	198.5	198.5
08_36-core	08_37-core	08_39-core	08_40-core	08_43-core	08_44-core	08_46-core	07_81-rim	07_82-rim	07_87-rim	07_88-rim
50.09	49.77	49.95	49.98	50.51	49.89	50.38	50.65	51.17	51.77	50.73
32.30	32.42	32.54	32.63	32.69	32.82	32.10	31.48	30.92	31.36	31.61
0.08	0.11	0.11	0.04	0.06	0.08	0.05	0.05	0.05	0.08	0.11
15.32	15.18	15.17	15.36	15.00	15.46	14.74	14.24	13.76	13.58	14.18
2.92	2.72	2.82	2.79	2.97	3.01	3.00	3.34	3.28	3.83	3.37
0.16	0.14	0.15	0.14	0.26	0.17	0.16	0.27	0.37	0.25	0.26
0.00	0.00	0.01	0.00	0.00	0.00	0.00	0.00	0.01	0.02	0.01
100.87	100.34	100.74	100.95	101.48	101.42	100.44	100.03	99.57	100.90	100.26
2.27	2.26	2.26	2.26	2.27	2.25	2.29	2.31	2.34	2.33	2.31
1.72	1.74	1.74	1.74	1.73	1.74	1.72	1.69	1.66	1.67	1.69
0.00	0.00	0.00	0.00	0.00	0.00	0.00	0.00	0.00	0.00	0.00
0.74	0.74	0.74	0.74	0.72	0.75	0.72	0.69	0.67	0.66	0.69
0.26	0.24	0.25	0.24	0.26	0.26	0.26	0.29	0.29	0.33	0.30
0.01	0.01	0.01	0.01	0.01	0.01	0.01	0.02	0.02	0.01	0.02
0.00	0.00	0.00	0.00	0.00	0.00	0.00	0.00	0.00	0.00	0.00
5.00	4.99	5.00	5.00	5.00	5.02	4.99	5.00	4.99	5.01	5.00
25	24	25	25	26	26	27	29	29	33	30
74	75	74	75	73	73	72	69	68	65	69
1	1	1	1	2	1	1	2	2	1	2

Table C5 Plagioclase composistions from the footwall anorthosites, Merensky Reef, Winnaarshoek.

Depth (m)	202.1	202.1	202.1	202.1	202.1	202.2	202.2	202.2	202.2	202.2	202.2	202.2
Sample	09_1_core	09_3_core	09_4_core	09_6_core	09_8_core	10_47_core	10_48_core	10_49_core	10_53_core	10_54_core	10_55_core	10_58_core
SiO2	52.67	50.71	51.09	51.04	49.59	49.47	49.59	49.05	50.56	49.12	49.69	49.96
Al2O3	30.54	31.73	31.53	31.41	32.37	32.49	32.57	32.73	31.39	31.97	32.50	32.06
FeO	0.10	0.05	0.08	0.07	0.03	0.08	0.04	0.14	0.03	0.05	0.07	0.05
CaO	12.80	14.40	14.04	14.19	15.28	15.52	15.47	15.68	14.16	15.00	15.08	14.90
Na2O	4.53	3.32	3.42	3.57	2.78	2.76	2.71	2.60	3.03	2.84	2.84	3.06
K2O	0.27	0.23	0.27	0.23	0.18	0.19	0.18	0.14	0.28	0.22	0.20	0.26
BaO	0.03	0.00	0.00	0.01	0.03	0.00	0.03	0.00	0.00	0.00	0.01	0.00
Total	100.94	100.45	100.42	100.52	100.25	100.51	100.59	100.33	99.45	99.20	100.40	100.29
Si	2.37	2.30	2.32	2.31	2.26	2.25	2.25	2.24	2.31	2.26	2.26	2.27
Al	1.62	1.70	1.68	1.68	1.74	1.74	1.74	1.76	1.69	1.73	1.74	1.72
Fe	0.00	0.00	0.00	0.00	0.00	0.00	0.00	0.01	0.00	0.00	0.00	0.00
Ca	0.62	0.70	0.68	0.69	0.75	0.76	0.75	0.77	0.69	0.74	0.73	0.73
Na	0.40	0.29	0.30	0.31	0.25	0.24	0.24	0.23	0.27	0.25	0.25	0.27
K	0.02	0.01	0.02	0.01	0.01	0.01	0.01	0.01	0.02	0.01	0.01	0.02
Ba	0.00	0.00	0.00	0.00	0.00	0.00	0.00	0.00	0.00	0.00	0.00	0.00
Total	5.02	5.00	5.00	5.01	5.00	5.01	5.00	5.00	4.98	5.00	5.00	5.01
Ab	38	29	30	31	24	24	24	23	27	25	25	27
An	60	70	68	68	74	75	75	76	71	74	74	72
Or	1	1	2	1	1	1	1	1	2	1	1	2

Table C5 Plagioclase composistions from the footwall anorthosites, Merensky Reef, Winnaarshoek.

202.2	202.2	202.2	202.2	202.2	202.1	202.1	202.1	202.1	202.1	202.1	202.1	202.1
10_59_core	10_60_core	10_62_core	10_63_core	10_67_core	09_12_rim	09_14_rim	09_16_rim	09_17_rim	09_20_rim	09_21_rim	09_2_rim	09_7_rim
50.91	46.78	54.63	51.98	48.83	51.66	51.28	50.11	50.43	50.25	49.64	52.95	50.50
31.25	29.42	29.49	31.02	32.30	31.51	32.12	32.82	32.10	32.26	32.56	30.27	31.59
0.05	0.03	0.04	0.08	0.12	0.09	0.05	0.04	0.07	0.15	0.08	0.05	0.07
13.81	13.44	11.31	13.44	15.57	14.21	14.54	15.39	14.94	14.98	15.30	12.59	13.98
3.43	2.76	5.28	3.79	2.58	3.25	3.41	2.89	3.09	2.99	2.64	4.27	3.41
0.28	0.27	0.22	0.14	0.19	0.19	0.24	0.16	0.23	0.17	0.18	0.20	0.24
0.01	0.01	0.00	0.00	0.00	0.01	0.00	0.00	0.00	0.00	0.02	0.00	0.00
99.73	92.71	100.97	100.45	99.59	100.93	101.64	101.41	100.86	100.79	100.41	100.33	99.78
2.32	2.30	2.44	2.35	2.24	2.33	2.30	2.26	2.28	2.28	2.26	2.39	2.30
1.68	1.70	1.56	1.65	1.75	1.67	1.70	1.74	1.71	1.72	1.74	1.61	1.70
0.00	0.00	0.00	0.00	0.00	0.00	0.00	0.00	0.00	0.01	0.00	0.00	0.00
0.67	0.71	0.54	0.65	0.77	0.69	0.70	0.74	0.72	0.73	0.75	0.61	0.68
0.30	0.26	0.46	0.33	0.23	0.28	0.30	0.25	0.27	0.26	0.23	0.37	0.30
0.02	0.02	0.01	0.01	0.01	0.01	0.01	0.01	0.01	0.01	0.01	0.01	0.01
0.00	0.00	0.00	0.00	0.00	0.00	0.00	0.00	0.00	0.00	0.00	0.00	0.00
5.00	4.99	5.01	5.00	5.00	4.98	5.01	5.00	5.00	5.00	4.99	5.00	5.00
31	27	45	34	23	29	29	25	27	26	24	38	30
68	72	54	66	76	70	69	74	72	73	75	61	68
2	2	1	1	1	1	1	1	1	1	1	1	1

Appendix D- Simple mass balance contamination models

Table D Simple mass balance contamination models

End Member Average Initial Values		
	ppm Nd	End
DM	2	3.3
B2 Like magma (Komatiite)	6	-1
Basal Rooiberg	64	-8.6
Archaean TTG	45	-14

Contamination (%)	**5**	**10**	**15**	**20**	**25**	**30**
Depleted Mantle (DM)	1.9	1.8	1.7	1.6	1.5	1.4
Basal Rooiberg (BR)	3.2	6.4	9.6	12.8	16	19.2
DM%	37.3	22.0	15.0	11.1	8.6	6.8
UC%	62.7	78.0	85.0	88.9	91.4	93.2
Epsilon Nd	-4.2	-6.0	-6.8	-7.3	-7.6	-7.8
Sum Nd (ppm)	5.10	8.20	11.30	14.40	17.50	20.60
Depleted Mantle (DM)	1.9	1.8	1.7	1.6	1.5	1.4
Archaean TTGs	2.25	4.5	6.75	9	11.25	13.5
DM%	45.8	28.6	20.1	15.1	11.8	9.4
TTGs%	54.2	71.4	79.9	84.9	88.2	90.6
Epsilon Nd	-6.1	-9.1	-10.5	-11.4	-12.0	-12.4
Sum Nd (ppm)	4.15	6.30	8.45	10.60	12.75	14.90
B2 Like magma (Komatiite)	5.7	5.4	5.1	4.8	4.5	4.2
Basal Rooiberg (BR)	3.2	6.4	9.6	12.8	16	19.2
B2	64.0	45.8	34.7	27.3	22.0	17.9
BR%	36.0	54.2	65.3	72.7	78.0	82.1
Epsilon Nd	-3.7	-5.1	-6.0	-6.5	-6.9	-7.2
Sum Nd (ppm)	8.90	11.80	14.70	17.60	20.50	23.40
B2 Like magma (Komatiite)	5.7	5.4	5.1	4.8	4.5	4.2
Archaean TTGs	2.25	4.5	6.75	9	11.25	13.5
B2	71.7	54.5	43.0	34.8	28.6	23.7
TTGs%	28.3	45.5	57.0	65.2	71.4	76.3
Epsilon Nd	-4.7	-6.9	-8.4	-9.5	-10.3	-10.9
Sum Nd (ppm)	7.95	9.90	11.85	13.80	15.75	17.70